DEVELOPING MULTIFUNCTIONAL

IRON OXIDE NANOPARTICLES FOR

NOVEL CANCER THERAPEUTIC STRATEGIES

A Dissertation
Presented to
The Academic Faculty

by

Christopher A. Quinto

In Partial Fulfillment
of the Requirements for the Degree
Doctor of Philosophy in the
Wallace H. Coulter Department of Biomedical Engineering

Georgia Institute of Technology
December 2015

DEVELOPING MULTIFUNCTIONAL

IRON OXIDE NANOPARTICLES FOR

NOVEL CANCER THERAPEUTIC STRATEGIES

Approved by:

Dr. Gang Bao, Advisor
Department of Biomedical Engineering
Georgia Institute of Technology
Department of Bioengineering
Rice University

Dr. John McDonald
Department of Biology
Georgia Institute of Technology

Dr. Hui Mao
Department of Radiology
Emory University

Dr. Krishnendu Roy
Department of Biomedical Engineering
Georgia Institute of Technology

Dr. Younan Xia
Department of Biomedical Engineering
Georgia Institute of Technology

Date Approved: 08/04/2015

To my loving girlfriend, Jenna
Who has supported and stood by me throughout the whole Ph.D.

ACKNOWLEDGEMENTS

I wish to thank Dr. Bao for giving me the opportunity to work in his lab and pursue my research in the nanoparticle field. I would like to thank the members of my thesis committee for the invaluable support and feedback over the past years—Dr. Gang Bao, Dr. Hui Mao, Dr. Krishnendu Roy, Dr. John McDonald, and Dr. Younan Xia. Much of the success and potential impact of my thesis project would have been impossible without their individually unique, and invaluable perspectives and areas of expertise.

The support staff in charge of the BME program, IBB, and core facilities are all amazing people that were always so helpful with any questions I might have. Specifically Sally Gerrish and Shannon Sullivan were critical in making sure I was on top of every form and task throughout the BME PhD and putting me in contact with the proper people for each of those steps.

Two of the undergraduate students I mentored, Hirishikesh Kale and Priya Mohindra, both worked in the lab for several years and their capable hands provided a huge boost to the pace of my research. They were both bright students full of potential, and I only hope the skills I taught them will prove useful wherever their lives take them.

My fellow lab members provided tremendous support both in technical training and in making the lab an enjoyable and entertaining place to work. In particular, Dr. Sheng Tong was instrumental in teaching me how to synthesize iron oxide nanoparticles and work with animal models. He was always available to bounce ideas off of or get a second opinion on a particular research direction. I wish him success in his future endeavors at Rice University. Yanni was always ready to inject some cute animals into our daily workflow through the institution of “cat time”. Only Brian’s “witty” puns could rival my own, and his assignment of our unofficial lab roles helped maintain structure and order for tasks which others may find inconsequential. Travis is just an all-around good guy, and I’ll miss

our frequent game nights. I doubt I'll ever meet another American who is as genuinely interested and immersed in the Chinese culture as Krueger. The Bao lab Olympics were always a great way to blow off some steam and put our lab skills to the test against each other. Sadly I never won due to my poor stability during the dizzy bat events.

Eli Fine and I joined the lab at the same time and ended up sitting next to each other throughout our five years at Georgia Tech. While there were a number of "unique" personality traits and quirks to become accustom to, we grew close during our time together. We were even roommates living in the infamous "Pirate House" through two of those years. Weekends were never boring with Eli always ready and willing to have a good time. I feel our adventures driving tanks, skydiving, and water jet packing were the highlight of any journal club where we shared our escapades through the ridiculous photos. While the Door Guardians never won the Bao lab Olympics, we were always strong contenders for top placement.

I was fortunate to enter the BME program with an amazing cohort that have become my closest friends in Atlanta. We've bonded through the many weeks of trivia, BBUGS/Emory social events, Georgia Tech football games/tailgates, brewery happy hours, bar nights, and general hangouts. We've supported each other through the graduate classes, qualifying exams, proposals, and now finally defenses. We were always there for each other to cheer us on for each step of the way. I am impressed with how far we've all come together throughout the whole PhD process, and I am sure we were all go on to do great things with our lives post Tech.

I want to thank my parents who have given me every opportunity in the world to succeed, and I am forever grateful. They are two of the smartest, most hardworking people that I know and have been tremendous role models for me to aspire to be like. My brother and sister are amazing people who have been there to support me my whole life. Even though we no longer live together under the same roof, I still feel as close to them as I did when we were little.

I especially want to thank Jenna Wilson for sticking with me throughout graduate school even when we were across the country from one another. She was always willing to look over my work to give me honest feedback, and I feel that has helped improve my ability to communicate ideas clearly and effectively. Her love and support have helped me get through the rough times when it felt like science was conspiring against me. Just knowing that I wasn't alone going through this process, and that I always had someone I could count on has pushed me to never give up throughout it all.

Of course, none of this work would be possible with the generous funding from the National Heart Lung and Blood Institute of the NIH.

TABLE OF CONTENTS

LIST OF TABLES

LIST OF FIGURES

LIST OF SYMBOLS AND ABBREVIATIONS

AMF	Alternating Magnetic Field
CPT	Camptothecin
DLS	Dynamic Light Scattering
DOX	Doxorubicin
DSPE	1,2-distearoyl-sn-glycero-3-phosphoethanolamine
FC	Field Cooling
IONP	Iron Oxide Nanoparticle
MFH	Magnetic Fluid Hyperthermia
MRI	Magnetic Resonance Imaging
PEG	Polyethylene Glycol
PTX	Paclitaxel
RES	Reticuloendothelial System
SPIO	Superparamagnetic Iron Oxide Nanoparticle
SQUID	Superconducting Quantum Interference Device
TEM	Transmission Electron Microscope
ZFC	Zero Field Cooling

SUMMARY

Magnetic nanoparticles hold tremendous potential to change the way that we study the body at the smallest level and can revolutionize how we diagnose and treat diseases. By reducing iron oxide down to the nanoscale, unique material properties are unlocked that drastically change how the particles interact with each other and respond to external magnetic fields. These unique properties of iron oxide nanoparticles (IONPs) enable a number of biomedical applications which covers nearly every possible area in biomedicine and continues to grow. Magnetic attraction can be utilized for bioseparation of tagged proteins or cells, directing stem cells to an injury site within the body, trigger protein signaling through forced interactions of cell surface receptors, or focus a drug carrier specifically to a tumor. The ability to influence the proton relaxation times of surrounding water molecules enables magnetic resonance contrast which can be utilized for cancer diagnostics or tracking stem cell fate following transplantation into the body. When exposed to an alternating magnetic field (AMF), the particles generate heat which can be used to either kill cancer cells directly or mediate the release of a chemotherapeutic. Each of these functions can be easily integrated with one another to create a truly multifunctional platform, but development of a nanoparticle for multiple simultaneous applications requires careful optimization of the common parameters for each function. For any biomedical application, the surface chemistry of the nanoparticle plays a critical role governing how the particle interacts with the physiological environment, prompting the design and evaluation of numerous iron oxide nanoparticle formulations over the years. Our lab has concentrated on phospholipid-PEG coated iron oxide nanoparticles that have been shown to be tunable in terms of composition, amenable to various bioconjugation strategies, stable in physiological buffers, and exhibit strong *in vivo* performance following systemic delivery. The overall goal with this project was to optimize the coating

composition and magnetic core size of phospholipid-PEG iron oxide nanoparticles for drug delivery, magnetic fluid hyperthermia, and magnetic resonance contrast applications and utilize these functions in combination for cancer therapy.

To evaluate the potential of the IONPs for a combination hyperthermia-chemotherapy cancer treatment, monodisperse, superparamagnetic iron oxide nanoparticles (SPIOs) 14 nm in diameter were synthesized via thermal decomposition and coated with either DSPE-PEG 2000 or DSPE-PEG 5000 (1,2-distearoyl-sn-glycero-3-phosphoethanolamine-N-[methoxy(polyethylene glycol)-2000/5000]) using a dual solvent exchange technique. The particles were initially characterized in terms of their core size, hydrodynamic diameter, and magnetic properties. The drug Doxorubicin (DOX) was loaded onto the particles through hydrophilic/hydrophobic and electrostatic interactions with the phospholipid-PEG coating at a high capacity and allowed for sustained release. The heat generation of the particles was determined by measuring the temperature of the ferrofluids when exposed to an alternating magnetic field generated by an inductor coil. By comparing the two PEG lengths, it was found that DOX loading and release were inhibited by longer PEG, but heat generation was unaffected.

Due to the variances between different cancer cell lines, three types of cancer (HeLa, U87, MCF7) were initially evaluated for their heat sensitivity. The HeLa cell line was chosen to examine the interaction of hyperthermia with DOX and two other drugs, Paclitaxel and Camptothecin. The SPIO-based delivery of DOX was capable of delivering the drug to the cell nuclei, and the SPIOs themselves were also internalized into the cells. The vesicles containing the nanoparticles could then be disrupted by MFH allowing for cytosolic release. Exposure of the cells to the DOX-SPIOs in a dose dependent manner confirmed that the DOX activity was not altered through loading and release from the SPIO carrier. The combination of MFH with SPIO-based DOX delivery enhanced the efficacy over that of either treatment alone, but a truly synergistic response could not be confirmed. When injected systemically, the SPIOs exhibited a long circulation half-life (~100 min)

and localized to the tumor and organs associated with the reticuloendothelial system (liver, kidneys, and spleen) while minimal uptake was found in the heart, lungs, and muscle.

It was hypothesized that by incorporating phospholipids with a phase transition above body temperature, a controlled drug release mechanism could be utilized to further control drug biodistribution. To this end, 1,2-dipalmitoyl-sn-glycero-3-phosphocholine (DPPC) was integrated into the coating at varying molar ratios (0-75%) with the DSPE-PEG. While the composition of the coating layer could be controlled by the initial molar ratios used in the coating process, increasing the amount of DPPC caused an increase in particles size and polydispersity. On the other hand, neither dye loading nor heat generation showed significant differences between the different coating compositions. Unfortunately, a distinct temperature-dependent release was not observed with any of the coating compositions.

Lastly, the effect of magnetic core size on heat generation and magnetic resonance contrast was evaluated. An initial numerical simulation was conducted using the linear response theory to identify the optimal core size for magnetic fluid hyperthermia using superparamagnetic particles and analyzed how polydispersity, magnetic anisotropy, and the alternating magnetic field parameters affected the size dependency. A systematic array of monodisperse iron oxide cores between 6 to 40 nm were synthesized through iterative regrowth thermal decomposition and coated with DSPE-PEG using the dual solvent exchange method. The saturation magnetization increased from 6-10 nm in size, but larger sizes did not show much change. All of the cores displayed magnetization curves indicative of superparamagnetism at room temperature despite the presumed superparamagnetic limit of ~20 nm. Furthermore, the coercivity remained relatively unchanged for the range of sizes tested. Both heat generation and MR contrast displayed a linear dependence with core size indicating a single mechanism governing each function throughout the size range. With equivalent iron concentrations, the cellular response to MFH using different sized cores reflected the large increases in specific absorption rate as the core size increased from

6 to 19 to 40 nm. Each of those core sizes was able to generate significant contrast *in vivo* to discern the ferrofluid distribution in a mouse tumor following intratumoral injection. Only the 40 nm nanoparticles were able to achieve temperatures relevant for apoptosis within the tumor during AMF exposure. The combination of MFH and nanoparticle DOX delivery inhibited tumor growth relative to a saline control, but differences with the individual treatments could not be distinguished within the measurement timespan of one week.

In summary, this work has examined the phospholipid-PEG coated iron oxide nanoparticle platform in the context of drug delivery, magnetic fluid hyperthermia, and magnetic resonance imaging for cancer therapy applications. The coating layer can be tuned in terms of the PEG length and lipid composition in a controlled manner through the dual solvent exchange method, and it was found that the drug delivery kinetics could be altered with PEG length. By increasing the core size up to 40 nm, exceptional heat generation and T_2 contrast were achieved that were relevant in an *in vivo* tumor model to visualize IONP distribution within the tumor using MRI and trigger apoptosis through MFH. These studies lay the foundation for the development of next generation multifunctional magnetic nanoparticles as a unique tool to improve the future of cancer treatment.

CHAPTER 1

INTRODUCTION

Iron oxide nanoparticles (IONPs) are unique compared to other types of nanoparticles because of their superparamagnetic property at nanoscale sizes which allows for magnetic resonance (MR) contrast, localization through magnetic force, and generation of heat through a process called magnetic fluid hyperthermia (MFH) when subjected to an alternating magnetic field (AMF). Various strategies have also been employed to develop IONPs as drug carriers. These functions of IONPs are attractive to cancer therapy where they can be used in both a diagnostic and therapeutic capacity. The inherent multifunctionality of the IONP platform poses a challenge when optimizing the nanoparticle design to excel at each application. The IONP system comprises two parts: the metallic core composed of magnetite (Fe_3O_4)/ maghemite (Fe_2O_3) and a coating layer of polysaccharide, polymer, or monomer. Previous studies have examined how IONPs can contribute to hyperthermia or drug delivery as individual cancer treatments, but combinatorial therapy remains limited. The IONP coating governs drug loading and can influence magnetic fluid hyperthermia which has spurred development of many different IONP coating formulations to achieve peak efficiencies. The magnetic core size determines whether the iron oxide nanoparticles fall within the superparamagnetic, single domain, or multidomain regimes which alter the underlying processes for MR contrast and MFH. Our lab has developed phospholipid-PEG coated IONPs that can achieve fine tuning of the core size from 6-40 nm and tailoring of the coating layer. The phospholipid-PEG enables hydrophobic drugs to be loaded passively due to hydrophobic/hydrophilic interactions with the coating for high drug loading without affecting the chemical structure of the drug. Thus, the **objective** of this work was to engineer the phospholipid-PEG-coated SPIO platform for optimal chemotherapeutic drug delivery, hyperthermia, and magnetic resonance

contrast. The **central hypothesis** is that the phospholipid-PEG coating layer and iron oxide core size can be tailored to enhance thermo-chemotherapy and MR contrast for cancer therapy. This hypothesis was investigated through the following aims:

Specific Aim 1: Develop a SPIO-based platform to enable MFH and drug delivery for enhanced cancer therapy.

The working hypothesis was that by coating SPIOs with phospholipids/phospholipid-PEG conjugates, the nanoparticles would be amenable to high drug loading and generating sufficient heat to raise the local temperature to apoptotic levels, enhancing cancer cell death through combination therapy. A dual-solvent exchange method was used to coat the SPIOs with either DSPE-PEG 2000, DSPE-PEG 5000. The chemotherapeutic Doxorubicin (DOX) was used as the model drug, as its hydrophobicity enabled loading into the lipid layer of the SPIO coating, and its fluorescent properties could quantify loading and release. The drug loading and release and heat generation during exposure to an AMF were compared between the two PEG lengths. Three different cancer cell lines (HeLa, U87, and MCF7) were evaluated for their sensitivity to hyperthermia over a range of temperatures and durations. DOX along with two additional drugs (Camptothecin and Paclitaxel) were assessed for their interaction with hyperthermia to enhance cell death. The DOX localization within the cells following DOX-SPIO incubation was examined through fluorescent microscopy, and SPIO internalization was measured via ferrozine assay for iron content. The viability of HeLa cells treated with DOX-SPIOs and MFH was analyzed for a combinatorial effect between MFH and DOX delivery. The DOX-SPIOs were translated to an *in vivo* xenograft mouse tumor model to determine circulation half-life and biodistribution via ferrozine assay on blood samples and *ex vivo* fluorescent imaging of the organs, respectively.

Specific Aim 2: Determine the effect of IONP core size on magnetic resonance contrast and heat generation.

The working hypothesis was that core size is a strong determinant for MR contrast and heat generation of IONPs, and a systematic comparison of cores sizes that cover the multiple magnetic regimes of IONPs could yield an optimal core size for both of these functionalities. Monodisperse iron oxide cores of 6, 8, 10, 15, 19, 25, 32, and 40 nm were synthesized via thermal decomposition and coated with phospholipid-PEG. The particles were characterized by measuring their size through TEM and dynamic light scattering and magnetic properties using a SQUID magnetometer. The specific absorption rates of the IONPs were evaluated by measuring the temperature increase when the IONPs were exposed to an AMF at two magnetic field strengths. The core size effect on T_2 relaxivity was determined by measuring the relaxation times of each core size over a range of concentrations. The signal enhancements of the different cores were compared via magnetic resonance imaging. The effect of magnetic fluid hyperthermia on U87 cell viability was assessed with an MTT assay. The SPIOs were intratumorally injected into U87 tumor-bearing mice, and the SPIO distribution was analyzed with MRI. To compare the heating efficiencies in a physiological environment, the intratumoral temperatures of the mice were measured during AMF exposure and the subsequent cell death was analyzed via histology.

This work is **innovative** because it is the first time phospholipid-PEG coated SPIOs have been used for a combined magnetic fluid hyperthermia and drug delivery application. The comparison of the efficacy of these two treatments alone and in combination can help elucidate potential synergistic effects with the two forms of therapy. Further, the recent advances in core synthesis have enabled this systematic study of core sizes that span multiple magnetic size regimes, and how those regimes relate to MFH and MR contrast efficiencies. The impact of this work is **significant** because it will optimize the SPIO platform for multimodal applications and raises questions as to the exact size cutoffs for

IONP magnetic properties. This work will lay the foundation for future clinical studies involving phospholipid-PEG-coated SPIOs for cancer therapy.

CHAPTER 2

BACKGROUND

Magnetism

A material's magnetic property stems from unpaired electron spins giving rise to a net atomic dipole moment, and the collective moments and alignments of each magnetic dipole with its neighbors in the crystal lattice determines the bulk material magnetism. There are several classes of magnetism including: paramagnetism, ferromagnetism, anti ferromagnetism, and superparamagnetism. With paramagnetic materials, thermal energy causes the magnetic dipoles to be randomly oriented such that there is no net magnetization when there is no external magnetic field. Exposure to a magnetic field causes the dipoles to align with the field causing the magnetization to be proportional to the strength of the applied field. The crystal lattice of ferromagnetic materials creates a state where it is energetically favorable for the magnetic dipoles to align in parallel with one another without the need of an external field. Bulk ferromagnetic materials have uniformly oriented dipoles regions organized into multiple magnetic Weiss domains where the overall magnetization of the material is the summation of each of the domains.[1] Antiferromagnetism is similar to ferromagnetism, but is the result of a favored anti-parallel orientation of the neighboring dipoles where the equal but opposite magnitudes cancel each other; therefore there is no net magnetization. Ferrimagnetism is related to antiferromagnetism, but the magnitudes of the neighboring dipoles are unequal creating an overall magnetization.

When an external magnetic field is applied to a multidomain material, the individual domains will attempt to align themselves with the external field until all of the domains are aligned, resulting in an increase in the total magnetization up to the saturation magnetization. The tendency for the domains to be aligned in this orientation after removal

of the external field is called the remanent magnetization, and to restore the original magnetic state, a specific magnetic field strength is required called coercivity. The mismatch between the applied field and the magnetization of the material leads to hysteresis loops in the magnetization curve.

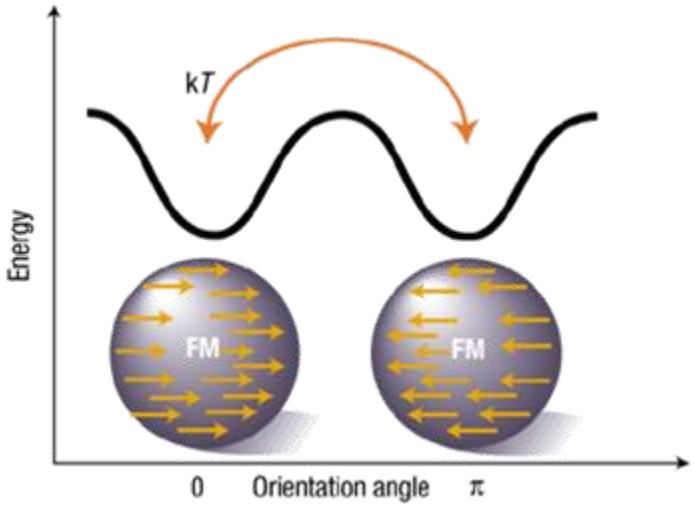

Fig. 2-1 Magnetic orientation flipping of superparamagnetic particles due to thermal fluctuations.

The superparamagnetic property represents a special case of ferromagnetic or ferrimagnetic materials when the size of the material is reduced to the nanoscale. The magnetostatic energy increases proportionally with volume, but the energy associated with the walls between magnetic domains increases with surface area. The high surface area to volume ratio of nanomaterials makes the existence of multiple magnetic domains unfavorable, so a single domain system dominates. The magnetization of single domain particles is subject to thermal fluctuations, and the mechanism of magnetic dipole rotation was first theorized by Stoner and Wohlfarth.[2] When the magnetic anisotropy energy barrier, energy necessary to rotate between the easy axes (stable directions of magnetization), of a particle is comparable to its thermal energy (kT), the magnetization direction can randomly flip between the parallel and antiparallel directions along the easy

axis (**Fig 2-1)**.[3] The relaxation time for magnetic reversal is given by the Néel-Brown expression [4, 5]:

$$\tau = \tau_0 \exp\left(\frac{KV}{k_B T}\right),$$

where $\tau_0 \sim 10^{-10}$s is the inverse attempt frequency, K is the anisotropy energy density, V is the magnetic core volume, k_B is the Boltzman constant, and T is the temperature. The magnetic anisotropy is based on both the crystal structure and shape of the particle. The blocking temperature, T_b, is reached upon cooling to the point where τ becomes longer than the experimental measuring time (τ_m):

$$T_B = \frac{KV}{k_B \ln(\frac{\tau_m}{\tau_0})},$$

Below the blocking temperature, the particle does not exhibit the superparamagnetic property of random magnetic reversals. Hence, the term superparamagnetism is specifically attributed to particles whose blocking temperature is below room temperature.

A solution of superparamagnetic particles has similar magnetic properties as a bulk paramagnetic material. When there is no applied magnetic field, the random flipping of the magnetic dipoles concurrent with Brownian motion results in zero net magnetic moment, but when a field is applied, the particles align their dipoles with the field direction, creating a strong net magnetization. Whereas the magnetization of paramagnetic materials is proportional to the magnitude of the applied field, superparamagnetic particles have a much larger magnetic susceptibility, so the magnetization plateaus to higher magnetic saturations even at relatively low external field strengths. The magnetic field response curves for superparamagnetism display a sigmoidal shape with very low coercivity and magnetic remanence compared to the open hysteresis loops of ferromagnetic/ferrimagnetic materials (**Fig. 2-2)**.[6] The lack of magnetic remanence is important for biomedical applications so that the particles will not be magnetically attracted to one another in solution to cause aggregation.

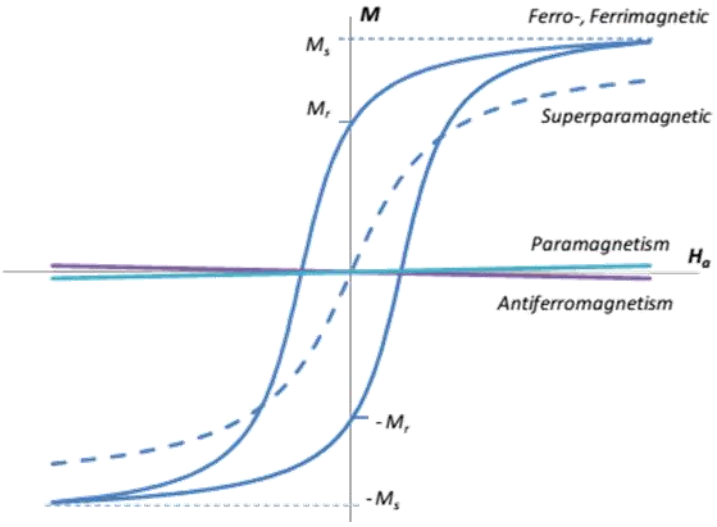

Fig. 2-2 Magnetic field response curves for ferromagnetic, ferromagnetic, paramagnetic, antiferromagnetic, and superparamagnetic materials. M_s is saturation magnetization and M_r is remanent magnetization.

The saturation magnetization for superparamagnetic particles is determined by the chemical composition and crystal structure of the nanoparticle. Iron oxide is the most well-studied type of superparamagnetic particle and while doping with elements such as nickel, cobalt, and manganese is characterized by higher saturation magnetization, these materials raise biocompatibility risks for *in vivo* use. In order to maximize the magnetization of iron oxide nanocrystals, a high purity magnetite (Fe_3O_4) structure is required though it is not very stable, and the particle surface is subject to oxidative transformation to the less magnetic maghemite (γFe_2O_3) when in contact with oxygen. Thus, the lower surface area to volume ratio of larger nanoparticles enables higher magnetic saturation through the increased magnetite crystal purity.

Superparamagnetic iron oxide nanoparticles for biomedical applications.

Superparamagnetic iron oxide nanoparticles are single magnetic domain particles composed of magnetite (Fe_3O_4) and/or maghemite (Fe_2O_3). The superparamagnetic property enables iron oxide nanoparticles to only exhibit magnetism when under the

influence of an external magnetic field, so they are stable in solution and will not spontaneously aggregate. This property also enables unique features, as they can influence the magnetic relaxation of the protons around them, experience force through magnetic field gradients, and generate heat when exposed to an alternating magnetic field. Biomedical applications have been developed which utilize these features, such as MRI contrast, bioseparation processes, magnetic targeting, and heat mediators in hyperthermia treatment.[7-13] Since other features, such as magnetic guidance and MR contrast, are intrinsic to the SPIO-based core, these functionalities can be applied without much additional modification of the nanoparticle. Specifically, the MR contrast allows for theranostic capabilities in which pharmacokinetics and dosimetry can be more accurately monitored by following drug-loaded SPIOs.[14-16] This is important for oncologists to determine whether the failure of the treatment to reach its expected therapeutic outcome is due to resistance to the treatment or because an inadequate dose reached the tumor.[17] The magnetic guidance can further enhance accumulation within the tumor by placing magnets proximal to the tumor during circulation which may enhance extravasation of SPIOs from the tumor vasculature into the interstitium.[18-20] These multifunctional features are exclusive to magnetic nanoparticles and make the SPIO a valuable nanoparticle platform for biomedical applications.

Toxicity and biocompatibility are of particular importance for *in vivo* applications of metallic nanoparticles. Of all the metal-based nanoparticles, iron oxide appears to be the safest, as there are well-known degradation and clearance mechanisms in the body for iron such as its incorporation into chelating proteins like hemoglobin, ferritin, and transferrin. Studies have found that these metabolic mechanisms apply to SPIOs, as systemic delivery of SPIOs led the particles to be broken down in the liver without observable toxic effects.[12, 21-23] SPIO formulations have been FDA approved as MRI contrast agents for years and more recently as the iron supplement Ferumoxytol.[24] While more studies

regarding the toxicity and safety of SPIOs are warranted, the clinical translation and FDA approval of these nanoparticles for other applications appears favorable.

Synthesis methods of iron oxide nanoparticles.

The classical method for synthesizing iron oxide nanoparticles is coprecipitation which involves aging stoichiometric mixtures of ferrous and ferric salts in an alkaline aqueous solution.[25, 26] The chemical equation for this reaction is given by:

$$Fe^{2+} + 2Fe^{3+} + 8OH^{-} \rightarrow Fe_3O_4 + 4H_2O,$$

To stabilize the particles in solution, polymers such as dextran are added to coat the particle surface.[27, 28] Coprecipitation is a facile synthesis method which can produce large quantities of nanoparticles in a single reaction, but there is poor size control of size and crystallinity, resulting in polydisperse samples with weak magnetic properties.

Microemulsion builds off of the coprecipitation principle, but aims for better size and shape control during the synthesis.[29] This method uses a water-in-oil system that creates micro or nanodroplets of aqueous iron salts stabilized by amphiphilic surfactants (reverse micelles).[30-32] The synthesis reaction is carried out within the droplets to control nucleation and growth of the nanocrystals. While this approach offers better size control, crystallinity is still low, and the yield is reduced.

Numerous other methods have also been developed to synthesize magnetic nanoparticles such as hydrothermal techniques,[33] ultrasound irradiation,[34] spray pyrolysis,[35] laser pyrolysis,[36] sol-gel,[37] and the use of magnetic bacteria.[38, 39] These methods often require stringent control of experimental conditions or expensive equipment while still not attaining the desired size, shape, and crystallinity for the produced nanoparticles.

The recently developed thermal decomposition method has become the gold standard for iron oxide nanoparticle synthesis. This technique, originally developed for semiconductor quantum dots, involves heating iron salts or organometallic precursors with

surfactants in a high-boiling point organic solvent up to 300^{o}C to trigger spontaneous nanoparticle nucleation and growth.[40-42] The process can be described as first, heating causes the precursors to reduce to their molecular species, increasing the monomer concentration. When the monomer concentration reaches a critical supersaturation point, spontaneous nucleation of the nanocrystals occurs. Nucleation causes a reduction in the monomer concentration which prevents further nucleation and proceeds to the growth stage. Remaining monomers in solution then interact with the nanocrystal seeds to increase their size. The transient changes in monomer concentration corresponding with the key steps in the nanoparticle synthesis were first described by Lamer and Dinegar and are represented in **Fig. 2-3**.[43] The surfactant molecules coordinate the addition of monomers to the growing crystal through dynamic solvation at high temperatures and determine the final equilibrium size of the nanoparticle population. The synthesized particles are capped by a hydrophobic surfactant layer which prevents further growth and aggregation. The size and shape of the nanocrystals can be controlled by the initial precursor and surfactant concentrations as well as the duration, ramp rate, and temperature of the reaction. In this manner, large quantities of monodisperse iron oxide nanoparticles with high crystallinity with tunable size and shape can be produced.[43-48] One unique benefit to this technique is that it allows for doping of other magnetic species such as manganese and cobalt which can alter the magnetic properties of the particles.[49-51]

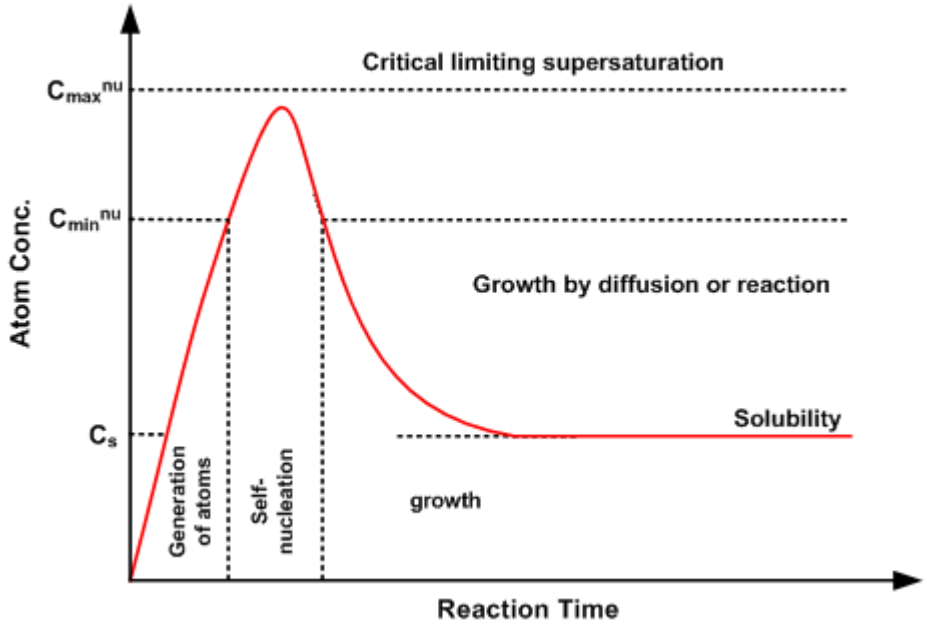

Fig. 2-3 LaMer model of colloidal synthesis.

Coating IONPs with phospholipid-PEG molecules.

The majority of IONP synthesis methods produce a colloid suspension that is stabilized in an organic solvent by hydrophobic surfactant molecules. The hydrophobic surface of the iron oxide cores requires a stable coating that will confer water solubility and prevent uptake by macrophages for *in vivo* applications. Many different coating molecules have been investigated, but most show poor long-term stability in physiological buffers, exhibit heterogeneity in terms of size/composition, are cytotoxic, or do not adequately protect the IONP during circulation.[8, 52] The most common coatings are made up of starch or dextran which can then be cross-linked to further stabilize the coating layer.[53, 54] While these coated IONPs have shown success in various biomedical applications, there remain questions as to how well the coating prevents recognition by macrophages, as they display relatively short circulation half-lives.[55] One strategy for coating IONP with hydrophobic surfactants is to adsorb amphiphilic molecules such that the hydrophobic region of the molecule interacts with the surfactants and the hydrophilic region is exposed to the aqueous

environment.[56, 57] Phospholipid-PEG conjugates are one such amphiphilic polymer with a low critical micelle concentration that were originally developed as surface modifiers for liposomes to improve circulation half-life and were later used to form micelle nanoparticle drug carriers.[58, 59] Polyethylene glycol (PEG), a commonly used coating agent for other nanoparticles, is conjugated to the lipid phosphate group to increase amphiphilicity and confer water solubility as well as prevent protein binding due to steric hindrance. Our lab has applied phospholipid-PEG to coating IONPs through the development of a dual solvent exchange method which is a modification of the film hydration method used to coat nanocrystals or form micelles and liposomes.[59-65] The final IONPs are coated with the 16 carbon chain lipid (1,2-Distearoyl-sn-glycero-3-phosphoethanolamine) PEG conjugate (DSPE-PEG). The 16 carbon length of the lipid matches the 16 carbon oleic acid surfactant on the SPIOs to promote interdigitation for a more stable coating.

Limitations of conventional chemotherapy.

While chemotherapy is one of the most common forms of treatment for various types of cancer, there are still high rates of recurrence and resistance to the treatment, indicating that substantial improvements are required. The available chemotherapeutic compounds require continual dosing to be effective and are often characterized by severe dose-limiting side effects that can be as harmful as the cancer itself. These adverse effects are attributed to nonspecific mechanisms of action and drug distribution to healthy tissue. In addition, many highly active drugs suffer from poor solubility, which decreases their bioavailability and thus inhibits their clinical effectiveness. It has been estimated that approximately 40% of potential drug candidates identified through high-throughput screening programs are discontinued due to their poor water solubility.[66, 67] Current trends in the drug lead identification process are beginning to relax the initial filter parameters in order to increase the possible chemical space, leading to more candidates with high lipophilicity and poor

aqueous solubility.[66, 67] Those compounds that do pass clinical trials often require excipients to ensure the drug has viable pharmacokinetics, but these can pose issues for dose escalation. Finding new ways to modify the pharmacokinetics and pharmacodynamics of these drugs is of key importance to make chemotherapy safer and more effective for the patient.[68]

Benefits of nanoparticle-based drug delivery.

The use of nanoparticles for drug delivery offers exciting possibilities to address many of the issues that hinder conventional chemotherapy. Loading the drug onto nanoparticles can protect the drug from degradation and oxidation while in circulation, as the drug will be sequestered away from the proteins and enzymes responsible for those functions. The size range for nanoparticles (10-100 nm) is one of the main determining factors for improving circulation half-life. The nanoparticles can be designed to be large enough not to be removed via kidney filtration, but small enough to avoid uptake and clearance by macrophages of the reticuloendothelial system.[69] Specifically for tumor delivery, nanoparticles can passively accumulate in the tumor interstitium via the enhanced permeability and retention (EPR) effect.[70] The heterogeneous angiogenesis of the developing tumor vasculature leads to gaps within the endothelial layer which are large enough (~100 nm) for nanoparticles to extravasate through. Once the nanoparticles enter the tumor, there is reduced drainage due to the poorly developed lymphatic system, leading to retention of the nanoparticles in the tumor interstitium. Through these mechanisms, nanoparticle-based drug delivery enables a higher localization within the tumor and reduces the potential of drug-specific side effects that result from accumulation in healthy tissue. Nanoparticle-based drug delivery can also enable a slow sustained release of drug molecules that can be more clinically effective and potentially require less frequent dosing. At the cellular level, nanoparticle-based drug delivery provides an alternative form of entry into the cell through receptor-mediated endocytosis, rather than by diffusion through the

cell membrane. Since the drug does not diffuse through the cell membrane, the drug efflux pumps, which would otherwise attempt to remove the drug from the cell, are not activated. The activation of these efflux pumps is inherent to multidrug resistance (MDR), which is observed in many types of cancer where chemotherapy has been ineffective.[71] Specifically, it has been observed that conjugating DOX to the surface of SPIOs is able to circumvent the ATP-binding cassette transporters associated with MDR.[72] For these reasons, delivering a drug using a nanoparticle can reduce systemic toxicity, lower the dosage needed and make that dosage more effective, and help mitigate the effects of multidrug resistance.

Methods of SPIO drug loading.

The most well-studied nanoparticles for drug delivery are liposomes, which carry drugs within an aqueous core enclosed by a lipid membrane. The inner volume of the particle is large and allows for water soluble drugs to be encapsulated with fairly high efficiency.[60, 73-78] Liposomal drug formulations have been successful and have resulted in FDA approval of DOXIL, which is a form of liposome-encapsulated Doxorubicin. In contrast to liposomes, IONPs have an inner core composed of iron oxide which limits interior cargo space. To compensate, IONP-based drug delivery is most often achieved through the conjugation of the drug molecule to the surface of the nanoparticles, exploiting the high surface area to volume ratio characteristic of particles at this size.[10, 16, 79] The downsides of this conjugation approach are that loading capacity is limited and complicated by the fact that each drug would need to be attached on a case-by-case basis to develop the proper conjugation scheme and even then, the activity of the drug could be compromised if the active site is unavailable for proper binding. Having the drug on the outer surface of the nanoparticle does not confer the same protective effects as loading within the particle and can also alter the charge and stability of the particle itself, further complicating the process by changing the pharmacokinetics.[80, 81] Moreover, the release

profile from these SPIOs is often very rapid, while a more sustained release is desirable in order to retain a clinically relevant local drug concentration.

An alternative loading approach would be to partition the drug within the coating layer on the SPIO. This type of loading is generally accomplished by using hydrophobic drug molecules that associate with the hydrophobic coating layer due to hydrophobic/hydrophilic interaction with the surrounding aqueous solvent. The loading of poorly soluble drugs is important from the pharmaceutical standpoint because many of the top chemotherapeutic compounds have issues with solubility which causes unfavorable pharmacokinetics. In the initial drug screening process, 40% of potential candidates are screened out early on due to hydrophobicity, and with the millions of candidates that are screened, a suitable nanoparticle carrier could help bring many of these drug candidates to market.[82] Previous studies have coated SPIOs with Pluronic, oleic acid-conjugated PEG, or glycerol monooleate and subsequently loaded DOX into an oleic acid surfactant layer. Each resulted in large particles (~200 nm) that still had limited drug loading and relatively short circulation half-life which can be attributed to the coating.[83-87] The large size makes extravasation difficult and increases likelihood of uptake by the RES system, both of which limit *in vivo* efficacy. The previous studies show that loading into the hydrophobic layer of the coating is possible, but a better coating method could be developed that would allow for a smaller particle size with a high drug loading capacity and long circulation half-life *in vivo*.

Hyperthermia as a cancer treatment.

Hyperthermia is a unique form of therapy which involves raising the temperature of a region of the body in order to treat a disease. The temperature necessary to elicit a heat response varies for different cell types *in vitro* and *in vivo*, but generally increasing the temperature of the tumor to 41-46^{o}C for approximately one hour triggers apoptosis, with thermal ablation occurring above 46^{o}C.[88-91] At ~43^{o}C, the heat can denature

intracellular proteins which then accumulate and set off signaling cascades for apoptosis in the cell. Conversely, higher temperatures induce necrosis. Additional targets influenced by heat are membranes, the cytoskeleton, and the proteins involved with DNA repair, all of which further destabilize the cell and offset homeostasis, making the cells more vulnerable to other forms of treatment.[92, 93] Tumors are especially susceptible to hyperthermia when compared to normal tissues because of their rapid cell division, increased hypoxia, low pH, and limited temperature regulation due to poor fluid transfer. While increasing blood flow in response to increasing temperatures is one of the body's main methods for thermal regulation, the tumor vasculature actually causes a decrease in blood flow with temperatures exceed 42^{o}C, causing tumors to be less capable of countering hyperthermia.[94-96] Overall, these characteristics make hyperthermia more selective for cancerous tissue over healthy tissue.[97]

Traditionally the application of hyperthermia has been performed through either water bath, high intensity focused ultrasound, radio-frequency interstitial tumor ablation, or laser induced thermal therapy, but all of these methods suffer from some combination of poor localization, short penetration depths, or high invasiveness.[98] These shortcomings limit the temperatures that can be applied, pose risks of damaging the surrounding tissue, and make sustaining a sufficiently high temperature throughout the whole tumor difficult for extended periods of time. Additionally, hyperthermia treatment alone has not been shown to be effective enough to fully remove the cancer. For these reasons, widespread clinical use of hyperthermia has been limited, but new methods of applying hyperthermia could make the treatment more localized and effective.

Hyperthermia is most often administered as an adjuvant to another form of therapy such as radiotherapy or chemotherapy.[97, 99] The increased heat aids both forms of therapy by causing vasodilation below 42^{o}C, which raises blood flow to the area and thus increases the amount of drug (in the case of chemotherapy) or oxygen (in the case of radiation) reaching the area. There are several different modes of interaction between heat

and drugs at the cellular level, including additive or superadditive interactions in which a linear increase in efficacy with increasing temperature is observed, threshold-behavior where an increased cytotoxic effect is only seen above a certain temperature, or independent effects where there is no interaction at all.[97] Specifically for Doxorubicin, the exact interaction with heat is inconclusive, as there are conflicting reports stating it is either additive, superadditive, or exhibits threshold-like behavior when used in conjunction with hyperthermia.[100-103] In order to take advantage of the interactions between hyperthermia and chemotherapy, there exists the need to develop agents that can deliver both forms of therapy concurrently in order to effectively couple the treatments at the disease site and maximize their interactions.

Magnetic fluid hyperthermia.

Magnetic fluid hyperthermia is the process by which magnetic nanoparticles generate heat when exposed to an alternating magnetic field. In this process, the thermal energy of the particle overcomes the barrier between the two easy axes of orientation, and the magnetic dipole re-aligns with the field each time the polarity is changed. For micron-sized, multi-magnetic domain particles, heat generation is mainly due to hysteretic losses which are not very efficient for the radio frequency energy delivered. For nano-sized, single magnetic domain particles, the re-alignment may occur through two mechanisms: Néelian paramagnetic switching where the magnetic dipole moves within the particle and is resisted by the magnetic anisotropy due to the crystal lattice and shape effects; or Brownian rotation in which the physical particle rotates to align with the external field and is resisted by shear stress from the surrounding fluid.[104, 105] The dominating mechanism is determined by the shorter relaxation time for the particle which is dependent on the magnetic core and coating properties.[106, 107]

MFH offers distinct advantages over conventional forms of hyperthermia application because it allows for the remote heating of the tumor from outside of the body

by delivering the heat source inside the tumor through a minimally invasive procedure. The envisioned therapy would only require an IV injection of the SPIOs followed by exposure to an AMF which would be akin to the fields sustained during an MRI. MFH is actuated by magnetic fields that are not attenuated by biological tissue, so there is no effective penetration limit for this form of therapy, which can be an issue for gold nanoparticle-based photothermal therapy.[108] The heat is generated from within the tumor itself so, with proper control of the external field parameters, heating of surrounding tissue should be minimal and heating of deep-seated tumors is possible. A nanoparticle heat source also offers the potential for localized heating inside the cell following endocytosis of the nanoparticle. Recent work suggests that bulk solution temperature does not need to be raised for a therapeutic effect; intracellular MFH could disrupt lysosomal membranes releasing proteolytic enzymes and increase reactive oxygen species to trigger cell death.[109] Compared to traditional hyperthermia treatments, MFH improves on the penetration depth and heat localization (including the ability for intracellular heating), which would make this form of hyperthermia more effective and safer for the patient.

MFH was first pioneered by Gilchrist et al. in 1957 using iron oxide microparticles.[110] Since then, intratumoral injection of SPIOs followed by MFH has been shown effective in pancreatic and skin cancer animal models.[111, 112] Systemic delivery of targeted dextran-coated SPIOs has been shown to slow breast cancer tumor growth *in vivo*.[55] In 2006, a phase I clinical trial was carried out in Germany using a direct injection of the SPIOs into various types of tumors and using a whole body magnetic field applicator. The study showed that this therapy is feasible and well-tolerated in human patients, but the heat distribution in the tumors were inadequate, suggesting that further optimization of the AMF and SPIO distribution in the tumor is needed.[113] While MFH addresses some of the main issues with conventional hyperthermia application and has shown feasibility in a clinical setting, it still does not have sufficient therapeutic effect to treat cancer as a singular treatment. Coupling chemotherapy or radiotherapy to MFH could

enhance the overall therapy for complete tumor regression by utilizing the synergistic interactions.

Iron oxide nanoparticle-based magnetic resonance contrast.

Magnetic resonance imaging is based on the nuclear spin magnetic relaxation processes of water molecule protons. The nuclear spins are first aligned with an external magnetic field followed by a radio frequency (RF) transverse pulse with a perpendicular alignment which temporarily perturbs the spins off of the original alignment. Upon removal of the RF pulse, the spins return to their original alignment according to two different relaxation mechanisms: longitudinal (T_1) and transverse (T_2) relaxation. T_1 relaxation concerns the realignment of the magnetic moment with the original field, and T_2 relaxation is described as the loss of signal in the perpendicular plane. When superparamagnetic nanoparticles are exposed to magnetic fields used in MR imaging, their dipole moments rotate to align with the field, creating a strong net magnetization which enhances the local magnetic flux. This phenomena has a strong effect on the MR signal from the surrounding water molecule protons as they are rapidly dephased. Specifically, the SPIOs cause a shortening of the spin-spin T_2 relaxation of the protons during MRI which is represented by negative contrast (loss of signal/darkening) on the MR image. The relaxivity of SPIOs is a measure of the inverse T_2 shortening time normalized to the molar concentration of iron expressed as s^{-1} mM^{-1}. In accordance to the outer sphere theory of relaxation, the SPIO MR contrast is dependent on strength of the local magnetic field inhomogeneities and the size of that field in relation to the number of protons influenced.[114-116] Two SPIO formulations Feridex I.V. and Resovist have been FDA approved as clinical MRI contrast agents for imaging of liver lesions. The MR contrast capability of SPIOs has been utilized for a number of applications ranging from tracking hematopoietic and neural progenitor cells *in vivo*,[117] imaging transgene expression,[118] delineating brain tumor borders,[119] atherosclerotic plaque detection in rabbits and humans,[120, 121] and tissue transplant monitoring of

pancreatic islets for diabetes therapy.[122, 123] While these studies provide a strong proof of concept for using SPIOs as MR contrast agents, sensitivity is still low compared to other imaging modalities, so there is a need to improve the relaxivity to enhance the signal contrast and reduce the delivered dose.

CHAPTER 3

OPTIMIZING SUPERPARAMAGNETIC IRON OXIDE NANOPARTICLE COATING FOR A COMBINED DRUG DELIVERY AND HYPERTHERMIA CANCER TREATMENT[1]

Abstract

Superparamagnetic iron oxide nanoparticles (SPIOs) have the potential for use as a multimodal cancer therapy agent due to their ability to carry anticancer drugs and generate localized heat when exposed to an alternating magnetic field, resulting in combined chemotherapy and hyperthermia. To explore this potential, we synthesized SPIOs with a phospholipid-polyethylene glycol (PEG) coating, and loaded Doxorubicin (DOX) with 30.8% w/w loading capacity when the PEG length is optimized. We found that DOX-loaded SPIOs exhibited a sustained DOX release over 72 hours where the release kinetics could be altered by PEG length. In contrast, the heating efficiency of the SPIOs showed minimal change with PEG length. With a core size of 14 nm, the SPIOs could generate sufficient heat to raise the local temperature to 43^{o}C, enough to trigger apoptosis in cancer cells. Further, we found that DOX-loaded SPIOs resulted in cell death comparable to free DOX, and that the combined effect of DOX and SPIO-induced hyperthermia enhanced cancer cell death in vitro. This study demonstrates the potential of using phospholipid-PEG coated SPIOs for chemotherapy-hyperthermia combinatorial cancer treatment with increased efficacy.

Introduction

Conventional cancer chemotherapy treatments are often compromised by systemic toxicity which stems from a lack of tumor specificity when anticancer drugs are delivered. The side effects limit the dose of the drug used, rendering effective cancer treatment difficult.

Nanoparticle-based drug delivery has the potential to overcome this challenge by targeted delivery to tumor and taking the advantage of tumor's natural leaky vasculature to increase the accumulation of drug-loaded nanoparticles within the tumor interstitium.[69, 70] By loading anticancer drug into nanoparticles, the more favorable pharmacokinetics and tunable biodistribution of nanoparticles can increase the efficacy of the drug.[76, 77] Drug molecules loaded into a nanoparticle may also be protected from degradation and oxidation while in circulation.[124, 125] A similar approach has been used with liposomal carriers in the form of Doxil; however, while having some reduction in cardiotoxicity, the efficacy in reducing tumor burden was not improved over free Doxorubicin.[75] Specifically, the use of liposomes as a drug carrier is hindered by their large size (>100 nm) which makes deep penetration into the tumor tissue difficult following extravasation from the blood vessel.[126, 127] Despite its shortcomings, the use of Doxil has stimulated the development of more advanced multi-functional nanoparticles.

Superparamagnetic iron oxide nanoparticles (SPIOs) have the potential to improve cancer treatment by generating local heat when exposed to an alternating magnetic field (AMF). Cancer cells are susceptible to hyperthermia, as raising the temperature to ~43^{o}C for 30-60 minutes can trigger apoptosis.[88, 90, 91] It is also possible that the cell membrane, cytoskeleton, and proteins involved in DNA damage repair could be affected by the increased temperature which further destabilizes the cell and offsets homeostasis, making cancer cells more vulnerable to chemotherapy.[92, 93, 128] It has been shown that tumors are especially susceptible to hyperthermia compared to normal tissues because of their faster cell division, increased hypoxia, low pH, and limited temperature regulation due to poor fluid transfer.[129, 130] However, hyperthermia alone may not be sufficient for cancer treatment and thus is often used as an adjuvant to other forms of therapy such as radiotherapy and chemotherapy.[97, 99] Further, the application of hyperthermia through high-intensity focused ultrasound, radio-frequency interstitial tumor ablation, or laser induced thermal therapy may pose risks of damaging the surrounding tissue, thus

preventing the widespread use of hyperthermia for cancer therapies.[98] Although previous studies have utilized SPIOs for hyperthermia[7, 131, 132] and drug delivery[84, 85, 133] separately, with different core synthesis methods and coating compositions, only very limited efforts have been made to optimize the SPIO-based approach for a combinatorial hyperthermia and chemotherapy for cancer treatment.[134]

Here we report the development and optimization of phospholipid-PEG coated SPIOs for simultaneous local heat generation and delivery of chemotherapeutic agents. The SPIO nanoparticle is composed of an iron oxide core of ~14 nm coated with a phospholipid-PEG layer which renders the SPIO water soluble and enables a high degree of drug loading through hydrophobic/hydrophilic and/or electrostatic interactions (**Fig. 3-1**). The SPIOs can generate a high amount of heat when an alternating magnetic field (AMF) is applied.[106] We quantified the effect of PEG length on drug loading and release, as well as temperature change, and identified PEG 2000 to be the optimal length. We demonstrate that the DSPE-PEG 2000 coated SPIOs can enhance cancer cell death through the concurrent delivery of local heat and chemotherapeutic drugs. Using the SPIOs as both drug carrier and heat source has the clear advantage of ensuring a close coupling between chemotherapy and hyperthermia for more effective cancer treatment.

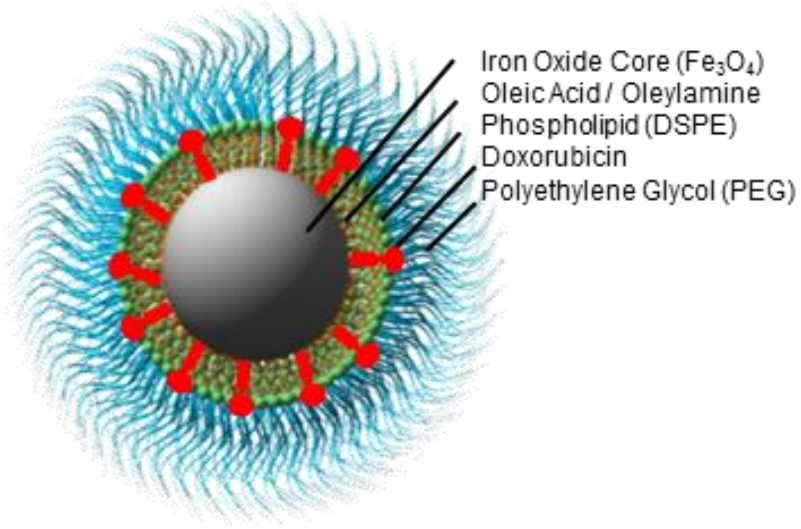

Fig. 3-1 Phospholipid PEG-coated iron oxide nanoparticle loaded with doxorubicin. The nanoparticle consists of an inner iron oxide core, covered with a surfactant layer of oleic acid and oleylamine, and an outer coating of phospholipid-PEG.

Methods

Chemicals

Iron acetylacetonate (Fe(acac)3 99%), 1,2-hexadecanediol (technical grade, 90%), oleic acid (technical grade, 90%), and oleylamine (technical grade, 70%), toluene (>99.9%), chloroform (99%), dimethyl sulfoxide (DMSO 99%) benzyl ether (98%), hydrochloric acid, hydroxylamine HCl, sodium hydroxide, ammonium acetate, ferrozine, and thioglycolic acid (>98%) were purchased from Sigma-Aldrich and used as received; 1,2-distearoyl-sn-glycero-3-phosphoethanolamine-N-[methoxy(polyethylene glycol)-2000/5000] (DSPE-PEG 2000/5000) was purchased from Avanti Polar Lipids. Doxorubicin hydrochloride (98.0-102.0% HPLC) was purchased from Sigma-Aldrich and dissolved in an aqueous solution at 1 mg/ml.

Synthesis of iron oxide nanoparticles

Iron oxide nanoparticle cores of 6 nm diameter were synthesized by an adapted published procedure.[51] Iron acetylacetonate (6 mmol), 1,2-hexadecanediol (30 mmol), oleic acid (18 mmol), and oleylamine (18 mmol) were mixed in benzyl ether (60 ml) in a 500 ml round bottom flask and magnetically stirred. A vacuum was applied for 40 minutes, then the solution was raised to 120^{o}C by a heating mantle attached to a temperature controller. After another 40 minutes, the vacuum was removed and replaced by a flow of Nitrogen. The solution was then raised to 200^{o}C and held for 2 hours before ramping to 300^{o}C and holding for 1 hour. The solution was then cooled to room temperature and ethanol (240 ml) was added to separate and precipitate the nanoparticle cores via three rounds of centrifugation. Finally, the cores were redispersed in toluene. To obtain larger core sizes, an iterative regrowth method was used that involves a modification of the seed synthesis protocol. Briefly, iron oxide nanoparticle seeds are mixed with an amount of iron acetylacetonate equivalent to mass necessary to increase the size of the cores by ~2 nm. Oleic acid and oleylamine are added at a 3:1 molar ratio to the iron acetylacetonate amount and 1,2-hexadecanediol is added at a 5:1 molar ratio to the iron acetylacetonate. Benzyl ether is then added to obtain a final iron acetylacetonate concentration of 20 mg/ml. The following heating and subsequent purification are the same as the synthesis procedure.

Dual solvent exchange coating method

To coat 1 mg Fe of SPIOs, 200 µl of the ferrofluid at 5 mg/ml Fe was mixed with DSPE-PEG (2000, 5000) in 400 µl of chloroform in a 100 ml round bottom flask. The amount of DSPE-PEG was determined based on a ratio of 8 DSPE-PEG molecules per nm^2 SPIO surface area. Then, 4 ml of DMSO was incrementally added followed by a 30-minute incubation at room temperature. The toluene and chloroform was removed via vaporization under vacuum. Afterwards, 20 ml of deionized water was then slowly added to the solution. DMSO was removed and replaced with deionized water through three rounds of

centrifugation in Vivaspin 20 centrifugal filter tubes with molecular weight cut-off 100 kDa (Sartorius, Goettingen, Germany). Finally, the solution was passed through a 0.2 μm HT Tuffryn syringe filter membrane (Pall Life Sciences, Ann Arbor, MI) and stored in deionized water at 4^{o}C.

Characterization

Transmission electron microscopy (TEM)

The average core diameter of the SPIOs was measured via transmission electron microscopy. The polymer coating layer on the SPIOs was visualized by negative staining with phosphotungstic acid on glow discharged copper grids prior to imaging. TEM images were recorded with a transmission electron microscope (Hitachi H-7500, Tokyo, Japan) connected to a CCD camera. The negative staining and TEM procedures were conducted by the Robert P. Apkarian Integrated Electron Microscopy Core at Emory University. The images were analyzed using ImageProPlus® software.

SQUID magnetization measurements

Magnetization measurements on uncoated iron oxide cores were carried out using a superconducting quantum interference device (SQUID) magnetometer (Quantum Design MPMS-5S, San Diego, CA). Field-dependent magnetization curves were measured at 300 K as a function of the external magnetic field in the range of 0-5x10^4 Gauss.

Dynamic light scattering

The hydrodynamic diameter of the coated SPIOs was measured using a dynamic light scattering device (DynaPro Nanostar, Wyatt Technology, Santa Barbara, CA). The SPIOs were dispersed in deionized water at 100 μg/ml Fe and measured at 25^{o}C. The mass weighted size distribution was reported.

Zeta potential measurements

The zeta potentials of DSPE-PEG 2000 and 5000 coated SPIOs and DOX-SPIOs were measured using a Malvern Instruments Zetasizer Nano ZS (Malvern Instruments, Worcestershire, United Kingdom). Non-loaded and DOX-loaded SPIO samples were suspended at 50 µg/ml Fe in phosphate buffered saline (13.7 mM NaCl, 1 mM Na_2HPO_4, 0.27 mM KCl) at pH 4, 7, and 10 in a disposable folded capillary cell.

Iron concentration measurement

Iron content of samples was determined using a ferrozine assay. Briefly, 50 µl of sample was mixed with 50 µl of 12 M HCl and incubated at room temperature for 30 minutes. Then, 240 µl of 2 M NaOH, 50 µl of 4 M ammonium acetate, 110 µl 5% hydroxylamine HCl, and 500 µl water were added to the solution sequentially. After 30 minutes of incubation, 50 µl of the solution were mixed with 0.02% ferrozine solution in a 384 well plate. Light absorption was read at 562 nm with 810 nm as the reference wavelength using a microplate reader (Safire2, Tecan Group Ltd., Männedorf, Switzerland). The absorption was compared to a molecular iron standard to determine the concentration. The number of SPIOs per gram of iron was estimated to be 1.35E17 based on the volume of a spherical 14 nm diameter SPIO and the density of magnetite (5.17 g/cm^3) assuming the cores were made up of Fe_3O_4.

Drug delivery

Drug loading

The chemotherapeutic drug Doxorubicin was loaded into the SPIOs by incubating the drug with nanoparticles at a 1:1 mass ratio in deionized water for 24 hours undisturbed at room temperature. The free drug was then removed via three rounds of ultracentrifugation for 1 hour at 40,000 g. The amount of Doxorubicin loaded was quantified by first incubating the SPIOs in thiogylcolic acid for 3 hours. Then the light absorption of Doxorubicin was measured using a microplate reader (Safire2, Tecan Group Ltd., Männedorf, Switzerland)

at 480 nm with 810 nm as the reference wavelength. The absorption was compared to a standard to determine the concentration. The DOX concentration was then divided by the iron concentration measured by a ferrozine assay to determine the DOX loading as % w/w DOX/Fe.

Drug release

The drug release profile was characterized by injecting 1 mg of SPIOs into a 20 kDa MWCO dialysis cassette (Slide-A-Lyzer, Pierce, Rockford, Ill). The cassette was placed in a release buffer of 80 ml PBS with 5% BSA kept at 37ºC and stirred. At the given time points, 100 µl aliquots were removed and replaced with fresh buffer to ensure sink conditions during the release period. The DOX fluorescence intensity of the aliquots was measured at 595 nm via UV-Vis spectrophotometer and the concentration of the aliquots was determined with a known standard. The amount released was compared to the initial amount loaded into the SPIOs to estimate the percent released.

Dye loading

The lipophilic dye, DiI, was loaded into SPIOs by incubating the dye with nanoparticles at a 40:1 mass ratio in deionized water for 24 hours undisturbed at room temperature. The free dye was then removed via passing through a 0.2 µm HT Tuffryn syringe filter membrane (Pall Life Sciences, Ann Arbor, MI) and stored protected from light in deionized water at 4ºC.

Magnetic fluid hyperthermia

A 1 ml volume of coated SPIOs at 0.4 mg/ml Fe was placed inside a polystyrene-insulated 7.5-turn, 2.54 cm inner diameter inductor coil (EasyHeat 2.4kW, Ameritherm, Scottsville, NY). The field strength within the coil was estimated according to the Biot-Savart law and the profile was modelled in matlab (Figure S1). An alternating magnetic field (23.77 kA/m, 355 kHz) was generated within the coil, causing the SPIOs to produce heat. The resulting

temperature rise in the ferrofluid was measured over three minutes with a fiber optic temperature probe (FLUOTEMP, Photon Control Inc., Burnaby BC, Canada) and recorded in real time. The slope of the linear region of the temperature vs. time plot was normalized to a water sample and used to calculate the SAR using the equation below:

$$SAR = \frac{1}{m_{Fe}} C_{H_2O} m_{H_2O} \left(\frac{dT}{dt}\right)$$

where m_{Fe} is the mass of the iron in the sample, C_{H_2O} is the specific heat of water, m_{H_2O} is the mass of the water, and $\frac{dT}{dt}$ is the temperature rise of the fluid. For the cellular experiments, the water circulating through the coil was adjusted to maintain a 37°C temperature in a 1 ml sample of media without SPIO during the AMF treatment. This baseline was chosen to mimic body temperature.

Modeling magnetic field profile within inductor coil

The normalized magnetic field strength profile within a 7.5-turn inductor coil (EasyHeat 2.4kW, Ameritherm, Scottsville, NY) of 3 cm length and 2.54 cm inner diameter was modeled using the Biot-Savart law in Matlab.

Cell culture

HeLa, U87, and MCF-7 cells were obtained from ATCC, USA and cultured in T75 cell culture dishes following ATCC instructions. Cells were grown in Dulbecco's Modified Eagle's Medium (DMEM) (Sigma-Aldrich) supplemented with 10% fetal bovine serum (ATCC). Cultures were replenished with fresh media every other day and passaged upon reaching 70% confluence.

Sensitivity to hyperthermia

HeLa, U87, and MCF-7 cells were seeded in 6-well plates in 3 ml of phenol red-free media and allowed to attach overnight. The media was replaced with prewarmed media at 37, 43,

44, 45, or 46ºC and left in a cell culture incubator set to the same temperature for 30 minutes or one hour. The media was then replaced with 37ºC media and left in the 37ºC incubator overnight. 24 hours post treatment, phase contrast images of the cells were taken with a fluorescent microscope (AxioVert S100, Zeiss, Jena, Germany) before being trypsinized, stained, and analyzed according to the established propidium iodide flow cytometry apoptosis protocol.[135] As an alternative method to assess cell viability, on the third day an MTT assay was performed. Briefly, the media in the wells was replaced with phenol red-free DMEM with 0.5 mg/ml MTT (3-(4,5-dimethylthiazol-2-yl)-2,5-diphenyltetrazolium bromide, Invitrogen) and incubated at 37ºC for 2 h. The formazan crystals were dissolved in 200 µl of DMSO and the absorbance was read at 570 nm with 810 nm as the reference. The cell viability was normalized to the 37 ºC control.

Drug and hyperthermia synergy

HeLa cells were seeded into a 96 well plate at 5000 cells per well. After an overnight incubation, free Doxorubicin, Camptothecin, or Paclitaxel was added to the wells at a range of concentrations. The plate was then placed in a water bath to maintain a hyperthermia temperature of 43ºC for 1 hour. Following the hyperthermia, the plate was returned to a 37ºC incubator. Cell viability was measured 48 hours post treatment using an MTT assay.

DOX dose response

HeLa cells were seeded in 96-well plates at 3000 cells per well in 100 µl of media and allowed to attach overnight. The media was replaced with either free DOX or DOX-loaded SPIOs (DOX-SPIOs) at a range of DOX concentrations from 0.1-50 µg/ml and incubated for 48 hours. An MTT assay was performed to assess cell viability. The cell viability was compared to the untreated control, and a dose response curve was generated to determine the IC50 by curve fitting.

Cell internalization

HeLa cells were seeded onto eight chamber glass slides at 5 x 10^4 cells per chamber and allowed to attach overnight. The media was replaced with either free DOX or DOX-SPIOs at 1 µg/ml DOX. At 2 and 8 hours of incubation, cells were washed with PBS, fixed with paraformaldehyde, and stained with DAPI. Cells were imaged with a DeltaVision deconvolution fluorescent microscope equipped with DAPI, TRITC, and Cy5 filters (Applied Precision, Issaquah, WA). Confocal image processing was done using the DeltaVision Softworx program (Applied Precision, Issaquah, WA). The fluorescent intensity of the images was normalized using ImageJ (NIH, Bethesda, MD). The iron internalization was measured by trypsinizing the cells, performing a cell count, and measuring the iron content of the cell population with a ferrozine assay and subtracting the endogenous iron measured from an untreated sample.

MFH-mediated intracellular release

HeLa cells were seeded onto 12 mm circular coverslips within a 24-well plate at 3 x 10^4 cells per well and allowed to attach overnight. The media was replaced with fresh media containing 200 µg/ml Alexafluor 488-conjugated dextran (10,000 MW) and 100 µg/ml Fe DiI-labelled SPIO. The cells were placed over an array of NdFeB, N42 circular magnets (K&J Magnetics, Jamison, PA) as used in the previous study by Landzuri et al. for 2 hours to internalize the SPIOs with magnetic force and dextran through endocytosis.[9] The cells were then washed twice with PBS and the media replaced with fresh media containing 10 mM of HEPES. A single coverslip is transferred to an isolated well of a 24-well plate to be placed in the 7.5-turn, 2.54 cm inner diameter insulated inductor coil and exposed to an alternating magnetic field (23.77 kA/m, 355 kHz) for two hours. The cells were then washed three times with PBS, stained with Hoescht, and mounted for fluorescent microscopy. The colocalization of the Alexafluor and DiI signals was analyzed by calculating the Pearson's correlation coefficient and Mander's colocalization coefficient

using the JACoP plugin for the ImageJ software. Background was corrected by using threshold value to remove noise and background signal for all channels.

Evaluation of combinatorial response to magnetic fluid hyperthermia and Doxorubicin delivery

HeLa cells were grown to 80% confluency in a T-75 cell culture flask. The cells were detached with 0.05% trypsin/EDTA and resuspended in cell culture media with 10 μM HEPES. The cells were counted and $5x10^4$ cells were pipetted into eight different cryovials. The vials were then filled to 1 ml of either media, media with 100 μg/ml Fe SPIO (without DOX), 100 μg/ml Fe DOX-loaded SPIO (16.6 μg/ml DOX), or an equivalent free DOX solution. Each of these groups had a +AMF/-AMF sample with the +AMF samples undergoing a 1 hour AMF treatment (23.77 kA/m, 355 kHz) and the –AMF samples kept in a cell culture incubator at 37^{o}C. An additional sample was heated in a water bath at 43^{o}C for 1 hour. Two hours after the AMF treatment, the media in each sample was then replaced with fresh media and seeded into a 96-well plate at 5000 cells per well so that the total incubation time with the SPIO/SPIO-DOX/DOX was 3 hours. After 24 hours, an MTT assay was performed to compare the cell viabilities between each of the groups. Alternatively, to assess the morphological changes after the AMF treatment, the media in each sample was instead seeded into an 8-well chamber slide (Nunc Lab-Tek II) at 25,000 cells per well. Phase contrast images of the live HeLa cells were taken 24 hours later using a Zeiss AxioVert S100 fluorescent microscope.

HeLa xenograft tumor model

All animal procedures were conducted with the approval of the Institutional Animal Care and Use Committee at the Georgia Institute of Technology. Xenograft tumors were induced in athymic nude mice by subcutaneously injecting 3M HeLa cells suspended in PBS into

the right flank. Tumors were monitored each day until they reached the appropriate size for experimentation.

Circulation half-life

The circulation half-life of the DOX-SPIOs was determined by delivering the nanoparticles to the mice via a 2 mg Fe/kg tail-vein injection and collecting blood samples at 5 minutes, 15 minutes, 30 minutes, 1 hour, 2 hours, 3 hours, and 24 hours post-injection. The iron content in each sample was measured with a ferrozine assay and normalized to the baseline blood iron content measured in control mice. The data was fitted to a logarithmic curve and the half-life of the DOX-SPIOs was determined.

Biodistribution

The lipophilic dye, DiR, was added at a 1:100 wt ratio (DiR:SPIO) during the DMSO addition of the dual solvent exchange coating process to allow for incorporation into the lipid layer. After coating, DOX was loaded onto the SPIOs as described previously. Tumor-bearing mice were anesthetized with isoflurane and injected with the DiR-DOX-SPIOs (2 mg/kg Fe) via tail vein injection and sacrificed 24 hours post-injection. Organs of interest were collected, blotted dry, and the DiR fluorescence was examined using the IVIS imaging system (IVIS Spectrum; Caliper LifeSciences, Alameda, CA). The excitation and emission detectors were set at 710 nm and 780 nm, respectively.

Statistical Analysis

For paired comparisons, Student t-tests assuming unequal variances were used to determine statistical significance ($p < 0.05$). For comparisons across multiple groups, analysis of variance (ANOVA) was used followed by a Tukey's Honest Significance Test with a 95% confidence interval to determine significant ($p<0.05$) differences between the experimental groups.

Results

Synthesis and characterization

Superparamagnetic iron oxide cores were synthesized using a thermal decomposition technique to produce monodisperse iron oxide cores of 14 nm in diameter stabilized with an oleic acid oleylamine surfactant layer (**Fig. 3-2A,B**).[51] To confer aqueous solubility to the nanoparticle cores, the SPIOs were coated with a layer of phospholipid-PEG (DSPE-PEG) using a dual solvent exchange method.[64] The coated SPIOs can be stored in an aqueous solution for months without any aggregation. The presence of the coating layer was confirmed through TEM imaging of the coated SPIOs negatively stained with phosphotungstic acid, as demonstrated by the white halos surrounding the dark iron oxide cores (**Fig. 3-2C**). Two different DSPE-PEG lengths were used for coating with molecular weights of 2000 and 5000 kDa. The coated SPIOs exhibited narrow size distributions (**Fig. 3-2D**) with peak hydrodynamic diameters were found to be 28.12 nm and 30.83 nm for the PEG 2000 and 5000 SPIOs respectively. Although the conformation of the PEG molecules has some effect, the size increase over the core diameter (14 nm) roughly correlates with the estimated size of the phospholipid-PEG molecules. It is important to note that the size shown on the negative stain TEM image in **Fig. 3-2C** does not accurately reflect the hydrodynamic diameter of the SPIOs, since the drying process results in contraction of the PEG chains.

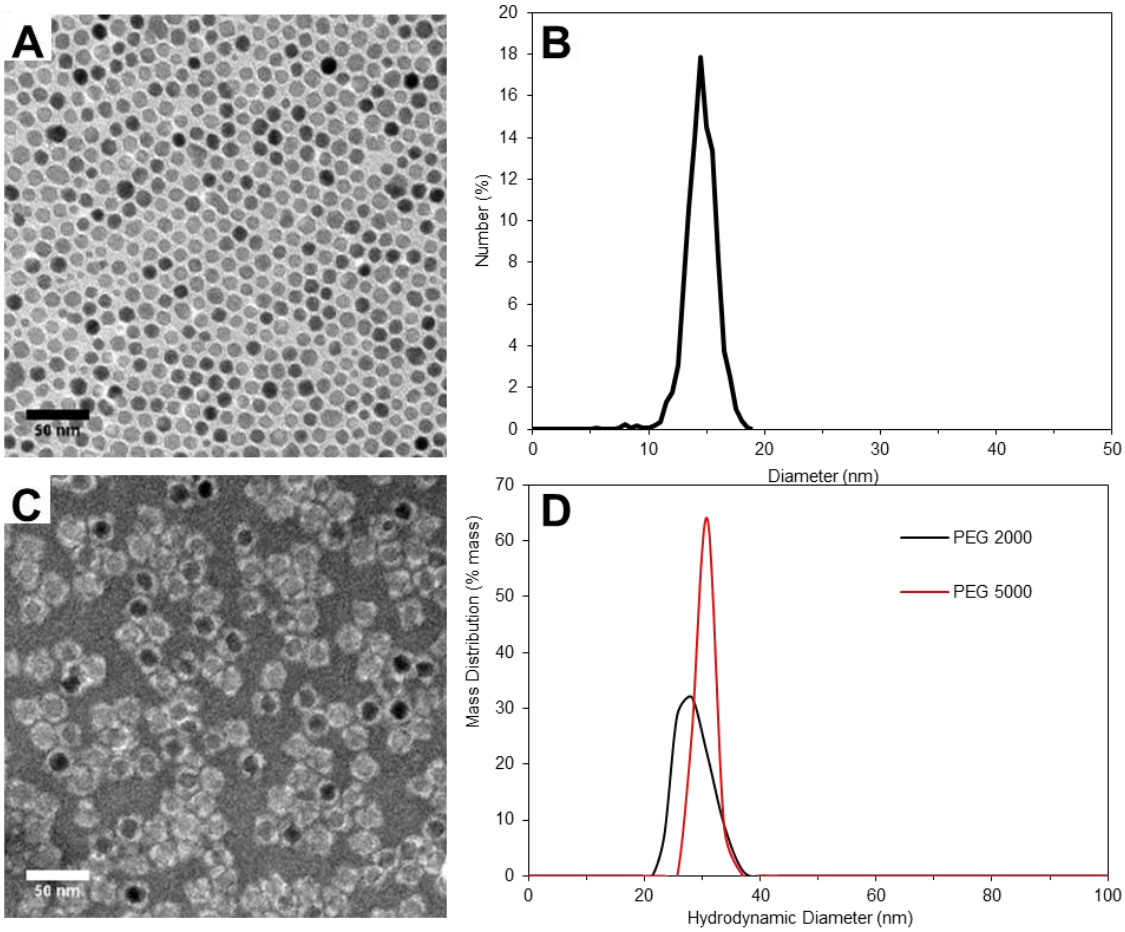

Fig. 3-2 Size measurements of iron oxide nanoparticles. (A) TEM image of SPIO cores and (B. Synthesized SPIO core size distribution. (C) PEG 2000 SPIOs negatively stained with phosphotungstic acid. (D) Hydrodynamic size distribution of SPIOs coated with DSPE-PEG 2000 and 5000 measured by dynamic light scattering. Room temperature magnetization curve of SPIO cores.

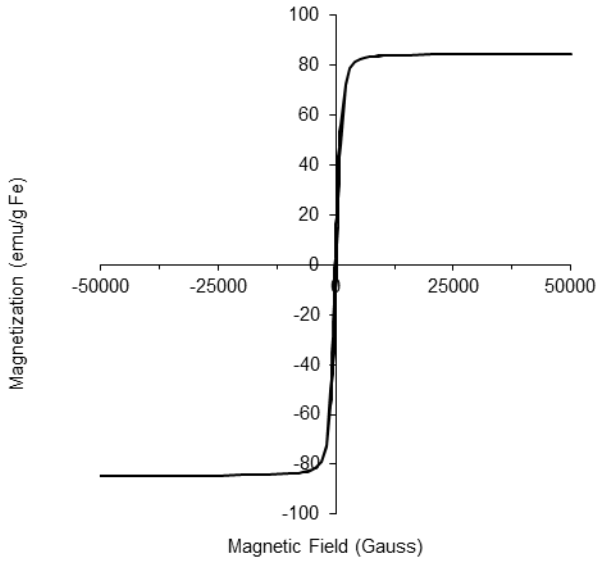

Fig. 3-3 Room temperature magnetization curve of 14 nm SPIO cores.

Heat generation by SPIOs

When SPIOs are exposed to an alternating magnetic field, they generate heat, which can be used for hyperthermia-based cancer treatment. The two main factors that influence the amount of local heat generation are: (1) the specific absorption rate (SAR), a measure of the heat generation per unit mass of SPIO and (2) the local SPIO concentration. The SAR is governed by the physical properties of the SPIOs and the applied magnetic field. Thus, the magnetization of the SPIOs was measured using a superconducting quantum interference device (SQUID) magnetometer, and the magnetic saturation was found to be 84.6 emu/g Fe, which approaches the theoretical limit of bulk magnetite (**Fig. 3-3**). The magnetization curve also displays the on/off behavior indicative of superparamagnetism, and the lack of hysteresis suggests that the primary mechanism of heat generation can be attributed to Néelian and Brownian relaxation rather than hysteretic losses.[106, 107]

The SAR of the SPIOs was calculated to evaluate the effect of PEG length on the efficiency of heat generation (see details in the Methods section). Aqueous solutions

containing coated SPIOs with 0.4 mg/ml Fe were exposed to an alternating magnetic field (23.77 kA/m, 355 kHz), and the temperature of the ferrofluid was measured as a function of time (**Fig. 3-4**). The SAR did not show significant differences between the PEG lengths and was determined to be 371 $\pm$ 15 and 425 $\pm$ 20 W/g Fe for SPIOs with PEG 2000 and 5000 respectively (**Fig. 3-4D**), as described in the Methods section. These results are consistent with the theoretical prediction that for SPIOs with a 14 nm core, Neélian relaxation is thought to be the predominant mechanism which is unaffected by the size of the coating.[106, 107]

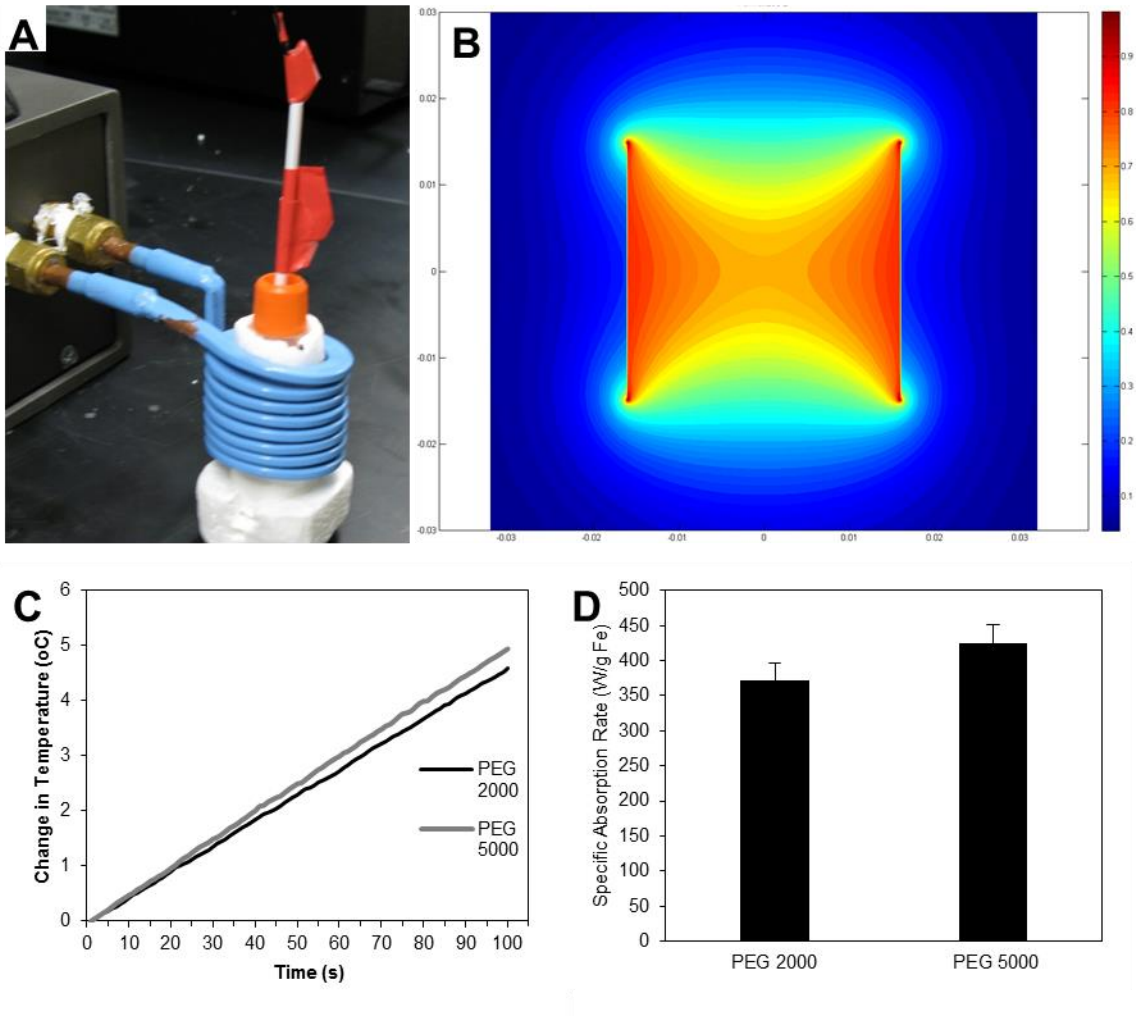

Fig. 3-4 Specific absorption rate measurement. (A) Hyperthermia test setup: 7.5-turn, 2.54 cm inner diameter inductor coil, polystyrene insulation, cryovials containing ferrofluid, fiber optic temperature probe positioned in center of sample, and (B) normalized magnetic field strength profile within inductor coil. (C) Temperature profile of a 1 ml aqueous solution containing SPIOs coated with PEG 2000 and 5000 at 0.4 mg/ml Fe during exposure to an alternating magnetic field of 23.77 kA/m and 355 kHz, (D) specific absorption rates of SPIOs coated with DSPE-PEG 2000 and 5000 calculated from the temperature profiles. Error bars represent standard error.

Doxorubicin loading into SPIOs

The amphiphilic nature of the SPIO coating layer facilitates loading of hydrophobic and amphiphilic drugs into the nanoparticles. The anthracycline antibiotic Doxorubicin (DOX) was chosen as a model drug in this study since it is a common chemotherapeutic that suffers from poor solubility in physiological buffers and exhibits significant cardiotoxicity.[75] Further, the fluorescence of DOX enables quantification of loading and release as well as analysis of cellular localization using microscopy. DOX was loaded into SPIOs by incubation with coated SPIOs at room temperature for 72 hours. To characterize the effect of PEG length on DOX loading into the SPIOs, the loading capacity of the PEG 2000 and 5000 SPIOs was compared. We found that the drug loading capacity of SPIOs with PEG 2000 was significantly higher (30.8 ± 2.2% w/w (DOX/iron)) than the PEG 5000 (14.5 ± 3.3%) (**Fig. 3-5A**). We also found that loading DOX into the coated SPIOs did not significantly alter the zeta potential of the SPIOs (**Fig. 3-5B,C**).

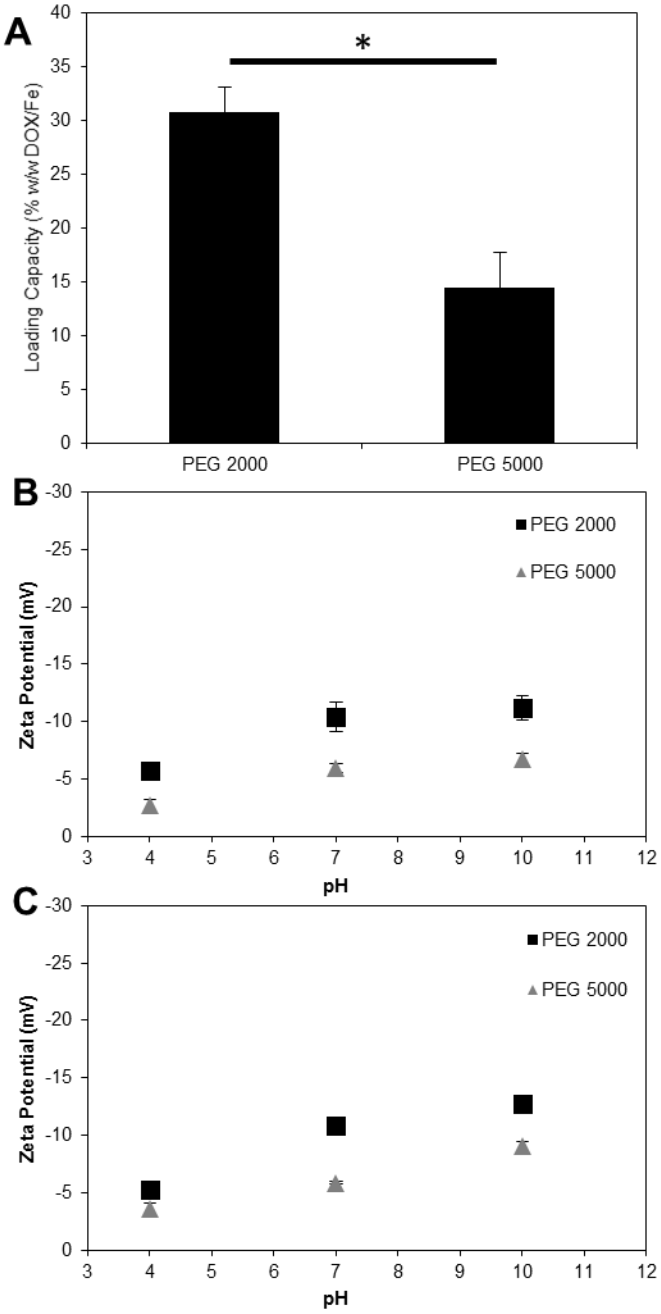

Fig. 3-5 Effect of PEG length on DOX loading into SPIOs. (A) DOX loading capacity of SPIOs coated with DSPE-PEG 2000 and 5000. Loading capacity was determined by the mass ratio (w/w) of loaded DOX compared to the mass of the SPIOs. Error bars represent standard error. * = significant difference (Tukey test $p<0.01$) Zeta potential of (B) SPIOs without and (C) with Doxorubicin loading.

Doxorubicin release

The drug release kinetics was assessed to ensure that the time scale of release is sufficient to allow for systemic circulation and subsequent sustained release in the tumor. The release profile was quantified using a dialysis cassette with a release medium consisting of PBS + 5% BSA, since serum albumin has been shown to bind anticancer drugs in circulation.[136] As shown in **Fig. 3-6**, there were moderate differences in the release profiles between the PEG lengths though each was characterized by an initial burst release within the first six hours followed by a period of slow sustained release. The SPIOs with PEG 2000 had the highest initial burst release, but SPIOs with PEG 5000 had a similar initial release rate after a two-hour lag period (**Fig. 3-6 inset**). We believe the much higher loading capacity of SPIOs coated with PEG 2000 has a clear advantage in overall effectiveness as a drug delivery agent, although in some cases a slower, more sustained release would be favorable as well.

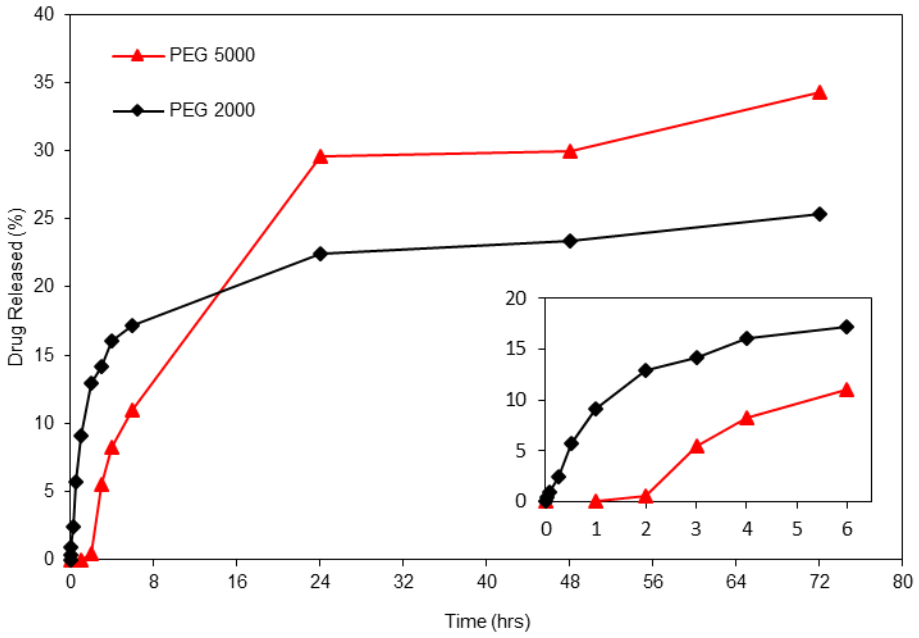

Fig. 3-6 Effect of PEG length on DOX release from SPIOs. DOX release from DOX-SPIOs as a function of time in a PBS buffer containing 5% BSA. Inset: first 6 hours of release profile.

Cell type-specific hyperthermia sensitivity

To better understand how hyperthermia affects different types of cancer and choose an appropriate cell line for further cellular studies, HeLa cervical cancer, U87 glioblastoma, and MCF-7 breast cancer cells were exposed to various heating conditions followed by an assessments of cell viability. As an initial screen, the three cell types were exposed to either 37, 43, 44, 45, or 46^{o}C for one hour and the percentage of apoptotic cells was measured via flow cytometry (**Fig. 3-7A**). The MCF-7 were the most thermotolerant, only showing apoptosis at the highest temperature tested (46^{o}C). In contrast, the HeLa and U87 cells displayed high degrees of apoptosis with the 44^{o}C treatment, 46% and 29.4% apoptotic cells, respectively, which decreased at the higher temperatures. To further characterize the thermal duration effect on the HeLa and U87 cells, the experiment was repeated for a 30 minute heating. Both cell lines had similar responses for all five temperatures used (37, 43, 44, 45, or 46^{o}C) with signs of apoptosis starting at 44^{o}C and increasing up to 30% (U87) and 25% (HeLa) apoptotic cells at 46^{o}C (**Fig. 3-7B**). The effects of hyperthermia were observed in the rounded, altered morphology of the cells and evidence of cell detachment (**Fig. 3-8**). The apoptosis results were then compared to cell viability measurements using an MTT assay which displayed a reduction in viability at a lower 42/43^{o}C (**Fig. 3-9**). The cell viability measurements may reveal effects of hyperthermia which were insufficient to trigger apoptotic programmed cell death, but did cause lasting damage to the cells which exist even 24 hours later. The MTT assay using the HeLa 43^{o}C temperature baseline was chosen for the following studies due the higher experimental throughput and more sensitive output for combined hyperthermia and chemotherapy treatments.

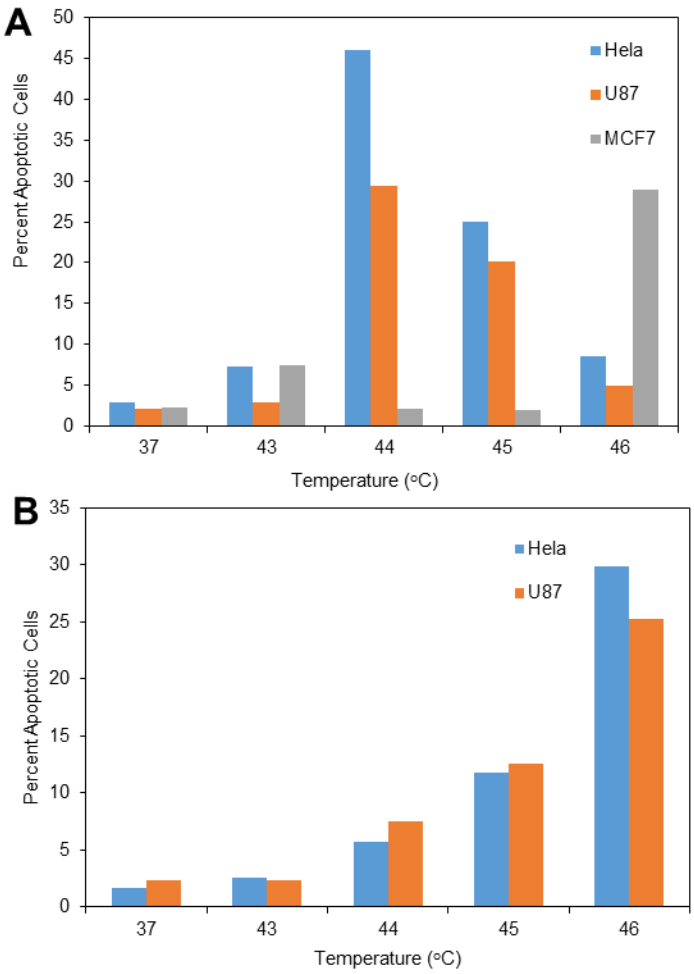

Fig. 3-7 Hyperthermia-mediated apoptosis in cancer cell lines. Apoptosis rates in cells exposed to (A) 1 hour and (B) 30 minutes of the indicated temperatures and measured 24 hours posttreatment with propidium iodide staining via flow cytometry.

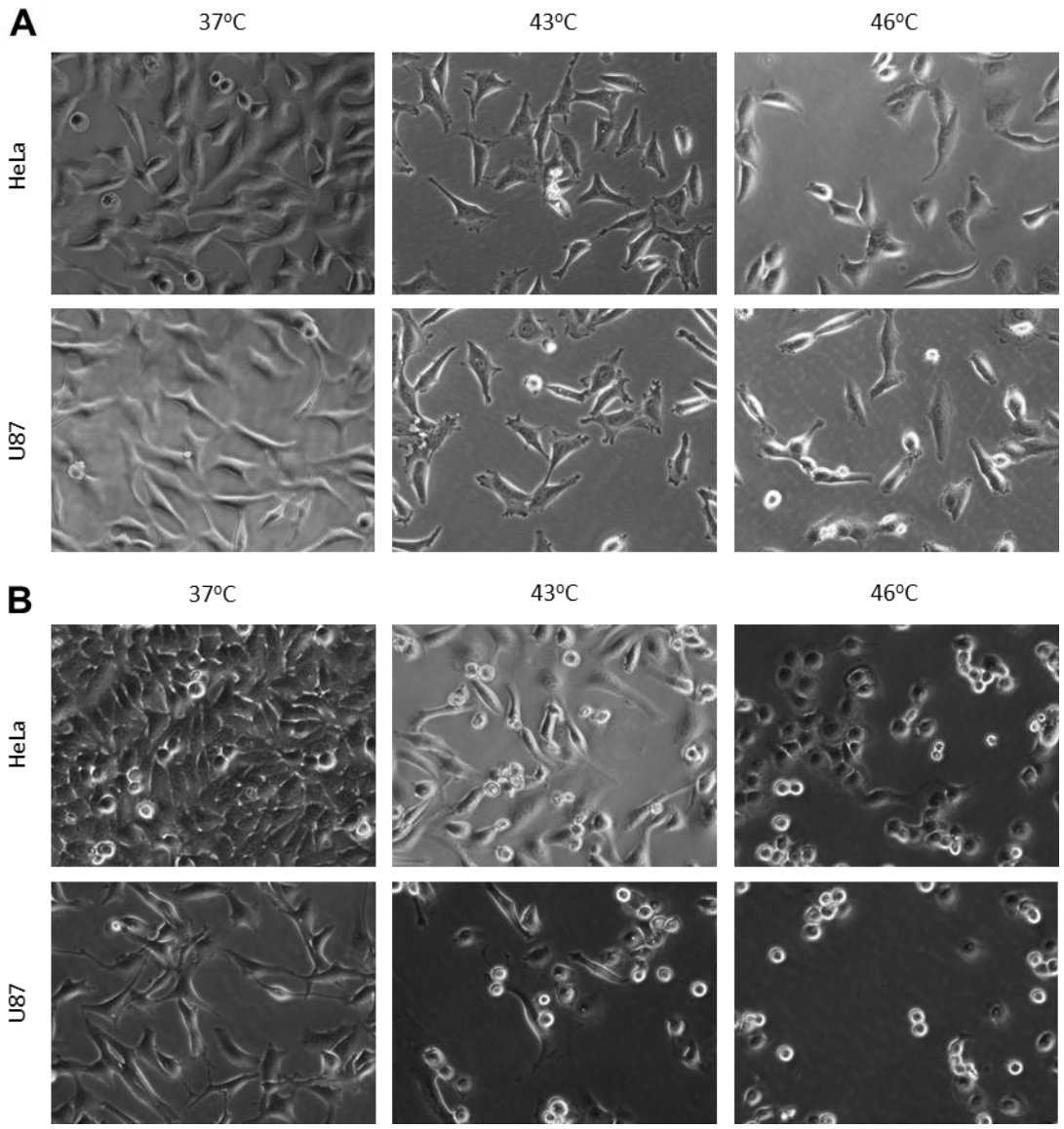

Fig. 3-8 Morphological effects of hyperthermia on cancer cells. Phase contrast images of HeLa and U87 cells exposed to the indicated temperatures in a cell culture incubator for (A) 30 minutes and (B) 1 hour. Images taken 24 hours post treatment.

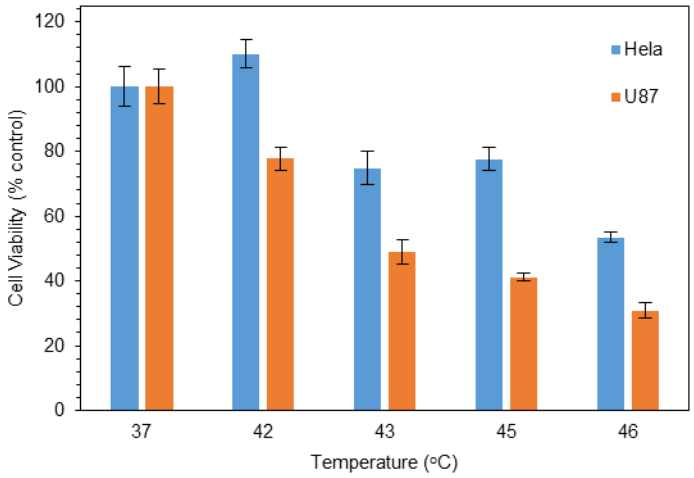

Fig. 3-9 Cell viability of HeLa and U87 cells exposed to the indicated temperatures for one hour and measured via MTT assay 24 hours posttreatment. Error bars represent standard error.

Drug-heat synergy

Three poorly soluble drugs, Doxorubicin (DOX), Camptothecin (CPT), and Paclitaxel (PTX), were examined for their potential synergy with hyperthermia using HeLa cells. These additional drugs were chosen as they have each previously been loaded into phospholipid-PEG micelles in a similar fashion as DOX, so translation to phospholipid-PEG coated SPIOs could be feasible.[59, 137-140] As shown in **Fig. 3-10**, both DOX and CPT exhibited an enhanced treatment efficacy with hyperthermia treatment which was more pronounced at higher drug concentrations suggesting synergistic behavior. By contrast, the combined effect of PTX and hyperthermia was additive except for the 50 nM concentration which was actually less effective with the addition of hyperthermia. While CPT is a potential candidate for combination therapy, its extremely low solubility in aqueous solutions (0.511 mg/ml) and lack of quantitative concentration measurement methods made SPIO-based drug loading studies difficult. For this reason, DOX was the only drug used for further SPIO studies.

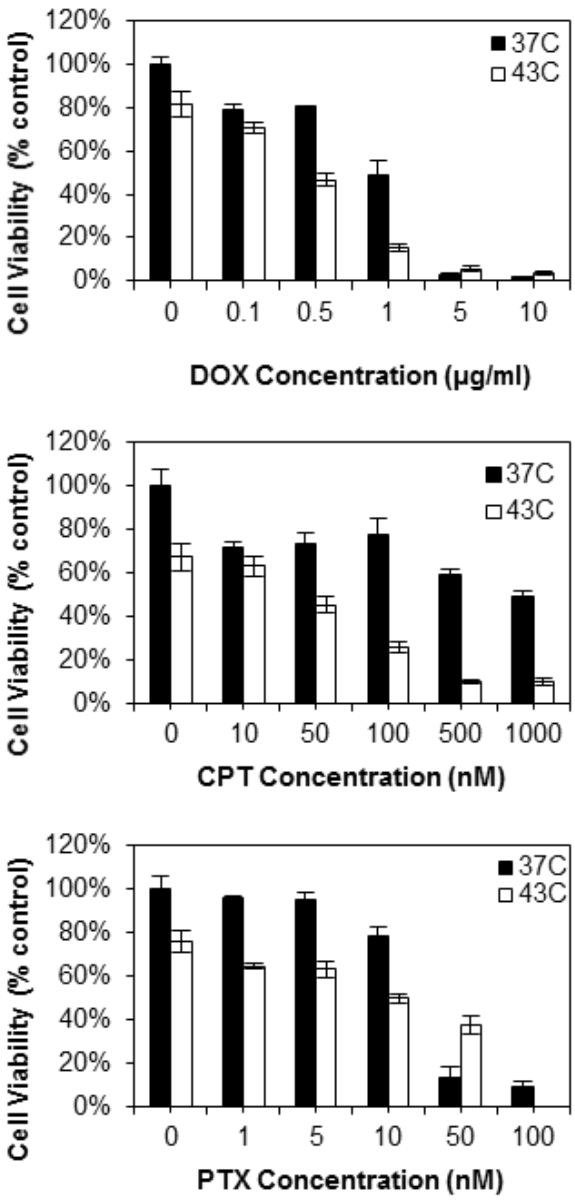

Fig. 3-10 Combination treatment of chemotherapy and hyperthermia. HeLa cell viability 24 hours posttreatment with a range of free DOX, CPT, or PTX concentrations with or without 43ºC water bath heating for 60 minutes. Error bars represent standard error.

Intracellular DOX-SPIO localization

Based on the results of magnetic fluid hyperthermia and drug loading and release, in all the subsequent cellular studies, SPIOs with PEG 2000 were used (hereafter referred to as SPIOs). To compare the cellular delivery efficiency of free DOX and SPIO-based DOX, HeLa cells were incubated with DOX-loaded SPIOs (DOX-SPIOs) or free DOX respectively and fluorescence microscopy was performed. DOX was observed in the cytoplasm and nucleus of the DOX-SPIO treated cells after 2 and 8 hours of incubation respectively. In contrast, the free DOX entered the cell nucleus after only 2 hours of incubation (**Fig. 3-11**). To assess SPIO internalization, the iron content of the cells was analysed and found to be 1.14 pg iron per cell, equivalent to ~153,000 SPIOs per cell. Estimating a cell volume of 2.5 pL, this correlates to an intracellular iron concentration of 455 µg/ml Fe, which should be sufficient for strong intracellular MFH based on the SAR measurement. These results suggest that the DOX-SPIO based approach enables efficient delivery of DOX into cells and a sufficient amount of the SPIOs are internalized to achieve both drug delivery and hyperthermia.

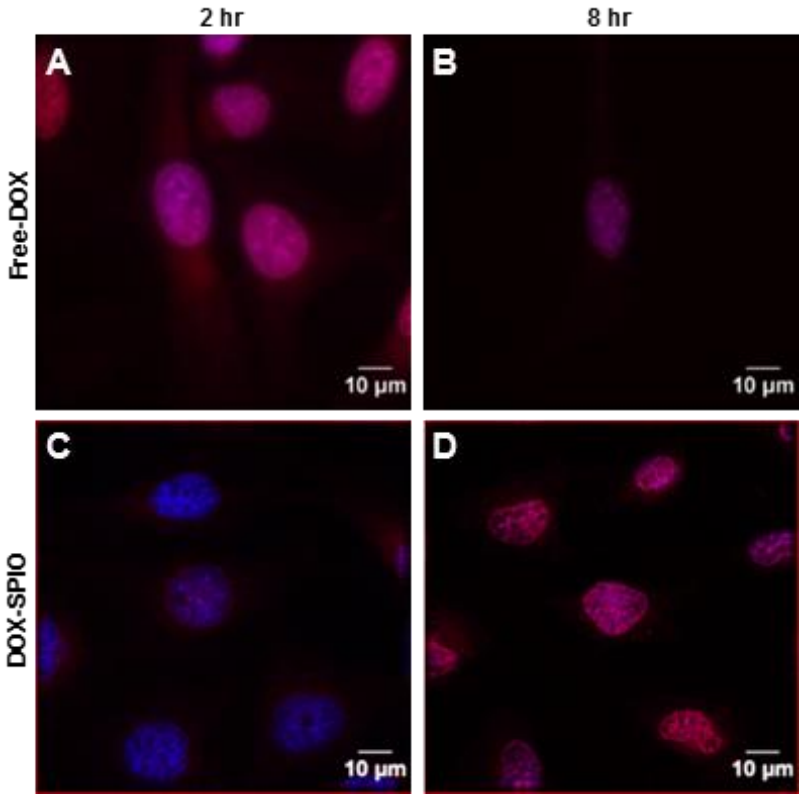

Fig. 3-11 DOX-SPIO internalization into HeLa cells. Confocal images of HeLa cells incubated with free DOX, (A) and (B), or DOX-loaded PEG 2000 SPIOs, (C) and (D), for 2 or 8 hours, respectively. The images displayed in (A-D) are overlays of two channels where cell nuclei are labelled in blue with Hoescht and DOX fluorescence is in red.

MFH-mediated intracellular release

There is growing evidence that intracellular hyperthermia can induce disruption of endocytic vesicles to release their contents within the cell.[109, 141-144] This controlled intracellular release has important implications in both drug delivery and macromolecule delivery using nanoparticles. To explore whether this phenomenon was occurring in our system, dye-labelled SPIOs were co-delivered with fluorescently labelled dextran to visualize endocytic vesicle release from magnetic fluid hyperthermia. By concurrently incubating the cells with both dextran and the SPIOs, the endocytosis process would be able to internalize multiple of each macromolecule within in the same vesicle. Disruption of the vesicle could then be identified by a reduction in colocalization of the two fluorescent signals compared to non-heated controls. We found that cells exposed to the AMF and thus subjected to intracellular MFH, had a distinct lack of the colocalized dextran/SPIO signals in contrast to untreated controls which would suggest release (**Fig. 3-12A**). Though even without MFH, the dextran and SPIO signals do not show complete colocalization which can be attributed to the spatially heterogeneous internalization of the two macromolecules. The heterogeneous SPIO distribution is exacerbated by the non-uniform magnetic field gradients driving magnetofection.

To quantitatively measure the difference in colocalization between the –MFH and +MFH cells, the Pearson correlation coefficient and the Mander's colocalization coefficients were calculated for each of the images.[145] The Pearson correlation coefficient (PCC) is a value between -1 (complete negative correlation) and 1 (complete positive correlation) which describes the relationship between the two signal intensities. The PCC was 0.777 and 0.608 for the –MFH and +MFH cells, respectively, indicating a significant drop in correlation after hyperthermia (**Fig. 3-12B**). The Mander's colocalization coefficients (MCC) range between 0 and 1 and describe the overlap of each signal with respect to the other (co-occurrence) which is independent of pixel intensities. Here M1 denotes the fraction of dextran signal compartments containing SPIO signal and

M2 denotes the fraction of SPIO signal compartments containing dextran signal. The M1 coefficient was significantly lower for the +MFH cells (0.069$\pm$0.028) than the –MFH cells (0.477$\pm$0.159) in contrast to the M2 coefficient which showed no significant difference between +MFH cells (0.429$\pm$0.135) than the –MFH cells (0.313$\pm$0.014) (**Fig. 3-12C**). These data suggest that some of the smaller dextran molecules (2.36 nm) are able to escape the vesicles with hyperthermia thus decreasing the fraction of dextran that overlaps with the SPIO signal (M1), but the SPIO may still be trapped in the vesicles with any remaining dextran so there is no change in M2.

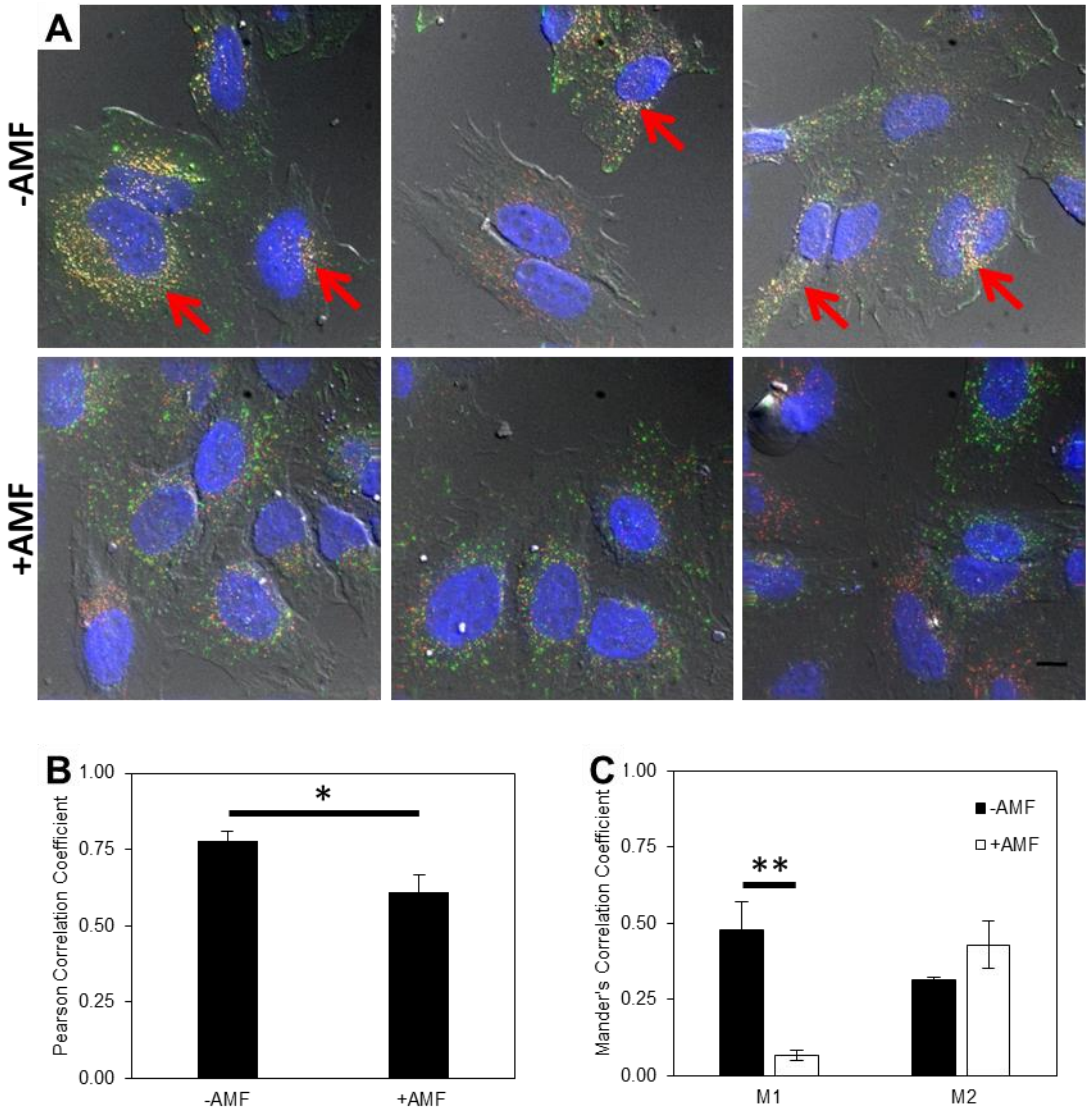

Fig. 3-12 Intracellular hyperthermia-mediated endosome disruption. (A) Representative confocal images of HeLa cells incubated with both Alexafluor 488-conjugated dextran and DiI-labelled SPIO then exposed to an AMF (23.77 kA/m, 355 kHz) or left in the incubator for 2 hours. The cell nuclei are labelled in blue with Hoescht, DiI-SPIO is in red, and Alexafluor 488-dextran is in green. Arrows indicate areas of SPIO and dextran colocalization displayed in yellow. Scale bar = 10 µm. (B) Pearson Correlation Coefficient and (C) Mander's Correlation Coefficients were determined for each set of images for quantitative colocalization analysis using the JACoP ImageJ plugin. Error bars represent standard error. *P < 0.05, **P<0.01 using the Student's t-test.

DOX-SPIO Dose response

The cytotoxic effect of the DOX-SPIOs was assessed and compared to free DOX in a dose response experiment. HeLa cells were incubated with either free DOX or DOX-SPIOs for 48 hours at a range of equivalent DOX concentrations and subsequently assessed for viability to generate a dose response curve. As shown in **Fig. 3-13**, the DOX-SPIOs had a slightly higher IC50 (2.42 µg/ml DOX, determined via curve fitting) compared to the free DOX (1.40 µg/ml DOX). The higher IC50 observed for the DOX-SPIOs may be due to the slower and incomplete release of DOX from DOX-SPIOs. These results suggest that loading DOX into SPIOs does not have an effect on DOX activity following release.

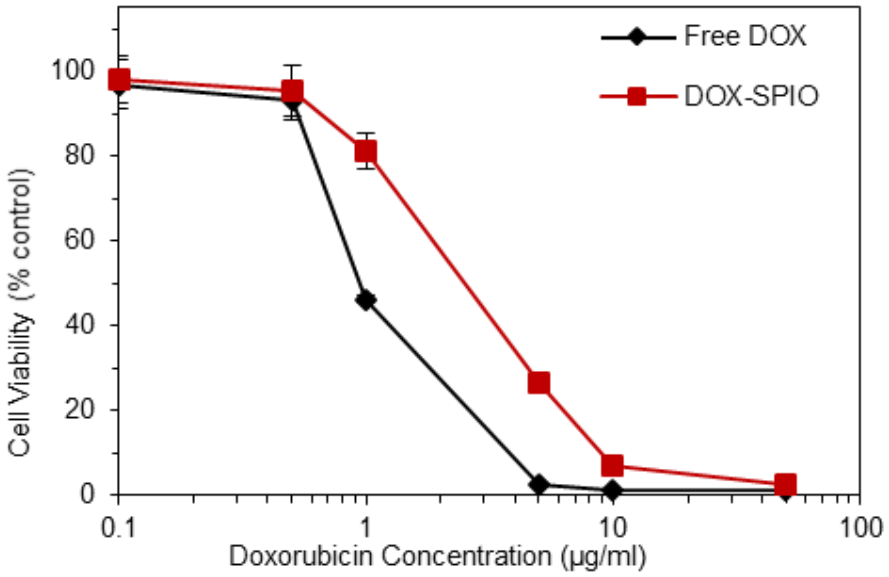

Fig. 3-13 Comparative dose response. Cell viability of HeLa cells incubated with equivalent DOX concentrations of either free DOX or DOX-loaded PEG 2000 SPIOs for 48 hours. Measurements were taken with an MTT assay normalized to an untreated control. Error bars represent standard error.

Combinatorial MFH and DOX delivery

In order to demonstrate the potential of SPIOs for combined cancer chemotherapy and hyperthermia, the effect of SPIO-induced MFH together with SPIO-based DOX delivery was determined through the assessment of cell viability. To observe a combinatorial effect, a mild thermal dose and short DOX-SPIO incubation with cells were chosen such that the combined effect would not be concealed by the death of the entire cell population by either treatment individually. By varying the treatment parameters, it was found that with a 100 μg Fe/ml (16.6 μg DOX/ml) concentration of DOX-SPIOs, neither a 1-hour MFH nor 3-hour DOX-SPIO incubation resulted in total cell death. **Fig. 3-14A** shows the temperature profile for the media, SPIO, and DOX-SPIO samples when exposed to the AMF for one hour. The SPIO and DOX-SPIO solutions reached 43^{o}C within 20 minutes while the media held a temperature of ~37^{o}C (**Fig. 3-14A**). The oscillation in the temperature curves is due to the water running through the inductor coil used to maintain the baseline temperature of 37^{o}C. Thus, applying AMF for 1 hour should subject HeLa cells to the apoptotic temperature regime (43-46^{o}C) with the necessary duration (~30 minutes) to trigger apoptosis.[146]

As shown in **Fig. 3-14B**, incubation with SPIOs alone (i.e., without DOX loading) or the presence of an AMF in the absence of SPIOs did not cause a significant drop in cell viability, indicating that SPIO incubation or magnetic field exposure alone does not affect cell viability. We found that water bath heating of HeLa cells at 43°C for 1 hour and SPIO-based MFH for 1 hour decreased cell viability to 57 $\pm$ 7% and 54 $\pm$ 10%, respectively, showing a comparable effect. SPIO-based DOX delivery decreased cell viability to 64 $\pm$ 11% after 3 hours of incubation, although it was not as dramatic as the free DOX, which is in agreement with the results from the dose response experiment. Based on the results of the release study shown in **Fig. 3-6**, only ~15% of the loaded DOX was released from the SPIOs after 3 hours, equivalent to a 2.49 μg/mL DOX concentration available to affect the cells (in comparison with 16.6 μg/mL in the free DOX case). Using the dose response curve

shown in **Fig. 3-13** a DOX concentration of ~2.5 μg/mL correlates to a reduction in cell viability by ~50%, consistent with the result shown in **Fig. 3-14B**.

HeLa cells subjected to the multimodal approach of DOX-SPIO delivery and SPIO-based MFH exhibited a lower cell viability (32 $\pm$ 9%) than either of the single modality treatments, namely drug delivery with DOX-SPIOs (64 $\pm$ 11%) or SPIO-based MFH (54 $\pm$ 10%) alone (**Fig. 3-14**). As shown in **Fig. 3-15**, we observed a reduction in cell attachment and an altered cell morphology of the DOX, MFH or DOX/MFH combinatorial treated cells (c, d, f, g) compared to the control cells (a, b, e), further confirming the effect of DOX-SPIO delivery and SPIO-based MFH. The combinatorial effect was consistent with the calculated additive response based on the decrease in cell viability observed in the individual treatments (**Fig. 3-14**).

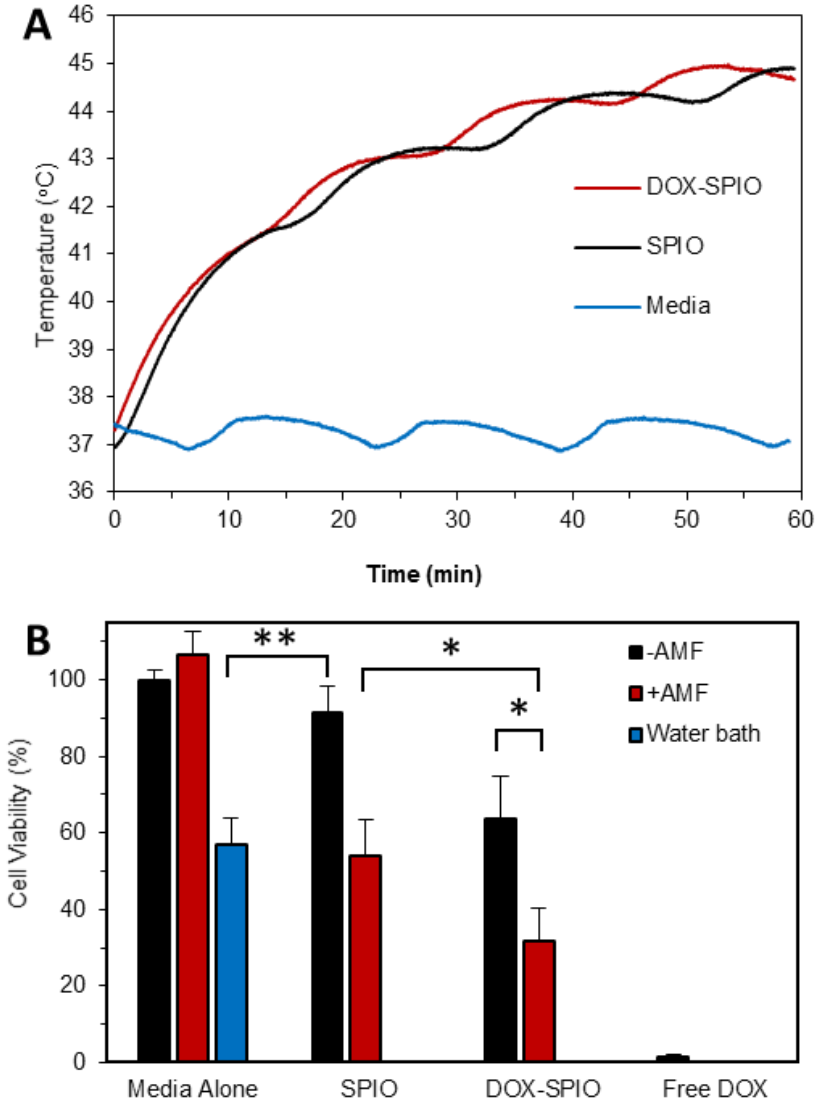

Fig. 3-14 Combined SPIO-based DOX delivery and SPIO-induced MFH. The viability of HeLa cells was determined following treatment with media alone, water bath heating (43ºC), just PEG 2000 SPIO (without DOX), DOX-loaded PEG 2000 SPIOs, or free DOX. Each of the indicated groups had samples with or without a 1 hour exposure to an AMF (23.77 kA/m, 355 kHz). (A) Temperature profiles during AMF treatment of media, SPIO, DOX-SPIO samples. (B) Cell viability measured 24 hours after treatment using an MTT assay. Error bars represent standard error. *P < 0.05, **P<0.01 using ANOVA coupled with Tukey HSD Test.

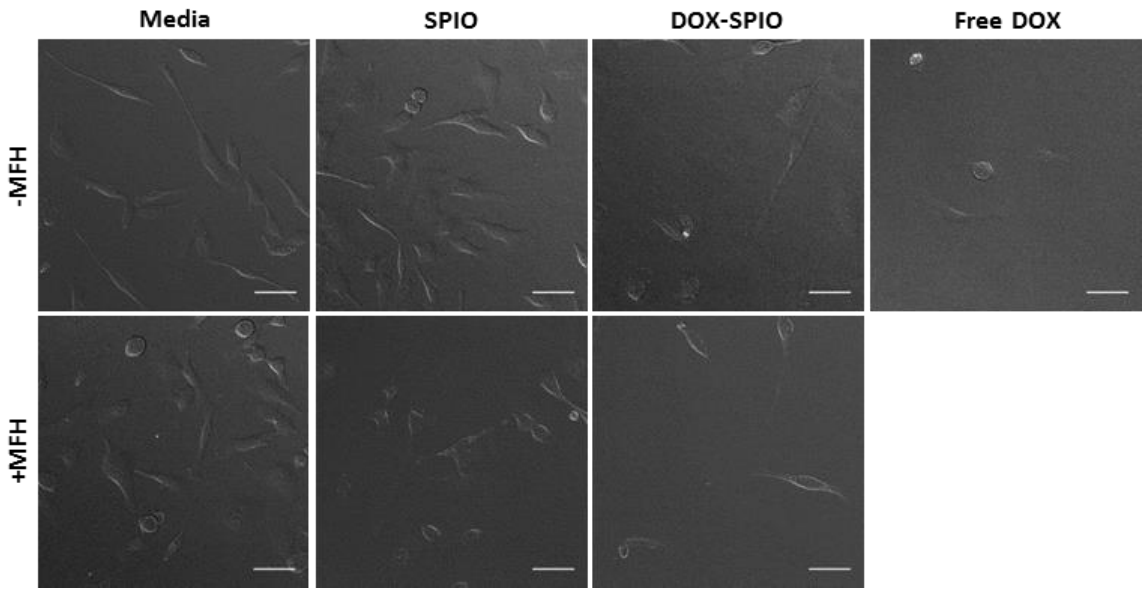

Fig. 3-15 Cell morphology following DOX/hyperthermia treatment. Phase contrast images of HeLa cells 24 hours post treatment with media alone, just SPIOs without DOX), DOX-SPIOs, or free DOX. Each of the indicated groups had samples with or without a 1 hour exposure to an AMF (23.77 kA/m, 355 kHz). Scale bar = 25 μm.

Circulation half-life and biodistribution

To understand the fate of the DOX-SPIO's following systemic injection, circulation half-life and biodistribution studies were performed. Following a tail vein injection, the blood concentration of the DOX-SPIOs exhibited an exponential decay with a calculated circulation half-life of approximately 100 minutes (**Fig. 3-16A**). This is a significant improvement over free DOX where 90% is removed from circulation within the first few minutes following injection.[77] Despite Doxorubicin's inherent fluorescence, DiR was co-loaded onto the SPIOs because it has a much higher extinction coefficient and quantum yield suitable for *ex vivo* fluorescent imaging.[147] The DiR-DOX-SPIOs were intravenously injected and sacrificed 24 hours later for *ex vivo* organ analysis using the IVIS imaging system (IVIS Spectrum; Caliper LifeSciences, Alameda, CA). The majority of the SPIOs were localized in organs associated with the RES (liver and spleen) and the kidneys though there was noticeable uptake in the tumor indicating good tumor targeting through the EPR effect. There was minimal uptake in the heart and lungs and no detectable signal in the muscle tissue (**Fig. 3-16B**) which is promising for limiting nonspecific toxicity of Doxorubicin which is known for its cardiotoxicity.[75] These results are consistent with a previous quantitative PET biodistribution study using ^{64}Cu-labeled phospholipid-PEG coated SPIOs.[63]

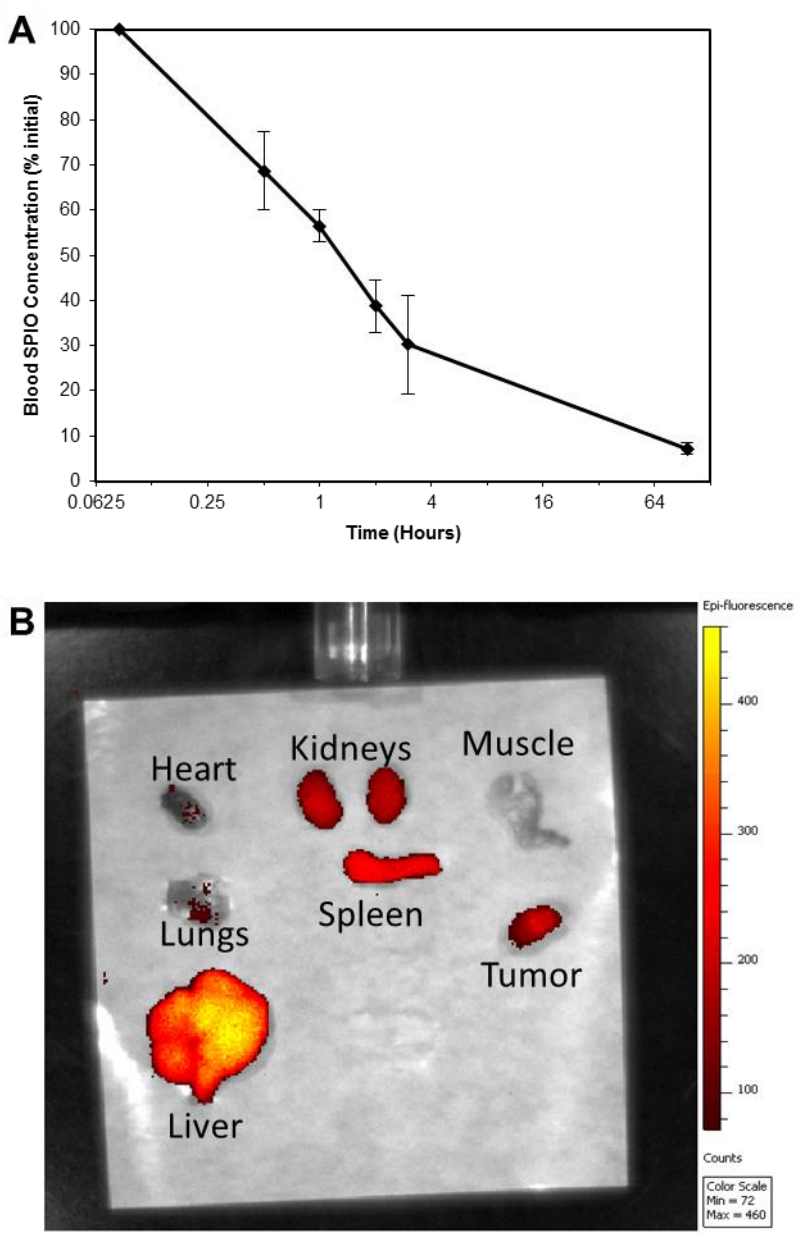

Fig. 3-16 Circulation half-life and biodistribution. (A) Normalized blood SPIO concentration measurements following intravenous injection of DOX-SPIOs (100 μg Fe) (n=3) of blood draws measured using ferrozine assay. (B) *Ex vivo* fluorescent imaging of mouse organs one day after intravenous injection of DiI-labelled DOX-SPIOs (100 μg Fe) measured with the IVIS imaging system. Signal represents DiI fluorescence.

Discussion

In the present work a combinatorial chemotherapy-hyperthermia cancer treatment was developed utilizing a phospholipid-PEG coating for SPIOs. Two different PEG lengths (2000, 5000 Da) were used to examine the influence on drug loading/release and MFH. Phospholipid-PEG is an amphiphilic molecule that associates with the surface of the SPIO through interdigitation of its lipid tails with the hydrophobic carbon chains of the oleic acid surfactant layer present on the iron oxide cores from the thermal decomposition synthesis.[64] The hydrophilic outer PEG chains are exposed to the aqueous environment, preventing protein opsonization and macrophage recognition.[148, 149] Longer PEG lengths have been associated with reduced protein adsorption and longer circulation half-life.[149, 150]

The amphiphilic nature of the coating layer enables drug loading due to hydrophobic/hydrophilic and electrostatic interactions between DOX and phospholipid-PEG.[151] This drug loading method does not require complex conjugation steps and can achieve high payloads similar to micelle-based drug delivery.[59, 125, 151] The negatively charged phosphate group in the phospholipid-PEG layer may aid drug loading through electrostatic interactions with the positively charged amine group on the DOX. The results shown in **Fig. 3-5** suggests that PEG 5000 shielded the negatively charged phosphate group more than that of PEG 2000, demonstrating that the high loading capacity is driven by a combination of electrostatic and hydrophobic/hydrophilic interactions between DOX and the SPIO coating layer. These interactions are consistent with previous results on DOX loading into lipid-PEG micelles.[151] The sustained release of DOX from the SPIOs helps maintain relevant drug concentrations within a tumor over long periods of time which can increase treatment efficacy and reduce dosing frequency. The slower release rate for SPIOs with PEG 5000 suggests the longer PEG length inhibits diffusion of DOX out of the SPIOs. Furthermore, the incomplete drug release found with both PEG lengths suggests that some DOX molecules were buried deep in the coating layer, thus difficult to be released due to

their interactions with the hydrophobic lipid layer. The maximum loading capacity with our SPIO formulation (31% wt) is significantly higher than the ionic bond-based loading (0.8 % wt) employed by Alexiou to deliver mitoxantrone to rabbits using their starch coated SPIOs.[20] The loading was also much higher than a similar passive loading into pluronic coated SPIOs (8.2% wt).[84] The high drug loading allows for lower overall iron delivery to achieve a therapeutic response.

The susceptibility to heat varies between different types of cancer in terms of duration and temperature, eliciting a range of cellular responses.[90, 146] While a one hour 44^{o}C treatment HeLa and U87 cells triggered a large increase in apoptosis rates, MCF7 cells were relatively resistant to hyperthermia through 45^{o}C. Reducing the duration to thirty minutes shifted the apoptosis peak temperature up to 46^{o}C for the HeLa and U87 cells (**Fig 3-7**). Cells are most sensitive to heat during mitosis, so the lower efficacy of hyperthermia with the MCF7 cells could be a result of the longer doubling time (38 hours) compared to HeLa (18 hours) and U87 (24 hours).[97, 152-154]

The complicated interactions of chemotherapeutics and hyperthermia depend on the mechanism of action of the drug and if proteins involved are denatured by the hyperthermia. The enhancement of cell death with hyperthermia was studied for Doxorubicin and two other drugs, Camptothecin, and Paclitaxel, which have been shown to be amenable for phospholipid-PEG loading.[137-140, 155, 156] Paclitaxel is a microtubule stabilizing agent which interferes with cell division, and the lack of a synergistic response in HeLa cells agrees with results for other cancer cell types.[157-159] On the other hand, Camptothecin acts by stabilizing the topoisomerase I-DNA complex to prevent DNA religation and disrupt DNA replication during mitosis. Combining Camptothecin with hyperthermia has been less studied, but a few reports indicate that the interplay could be timing and drug concentration dependent.[160, 161] For the concurrent delivery and range of concentrations (0-1000 nM) used in this study, an enhanced effect was seen above 50 nM. The exact interaction between DOX and elevated temperature

remains elusive, since there are conflicting reports on whether the combined effect is additive, superadditive, or threshold-like when used in conjunction with hyperthermia.[100-103] Our results with water bath heating display a potential synergistic behavior at concentrations near the IC50 (1 μg/ml) (**Fig 3-10**).

Applying the DOX-loaded SPIOs to HeLa cells, we observed a slower accumulation of DOX into the cell nucleus when delivered via SPIOs compared to free DOX which may be attributed to the facts that DOX must be released from SPIOs prior to translocation and that burst release takes ~6 hours. The SPIOs were also internalized into the cells and could provide an alternative form of drug entry into the cell instead of relying on diffusion through the cell membrane. This pathway for drug delivery could prevent triggering of drug efflux pumps that reduce intracellular drug concentrations and factor into multidrug resistance. Once within the cell, the intracellular MFH appears to trigger vesicle disruption allowing the contents to be released. Similar macromolecule release has been observed with gold nanospheres and EGFR-targeted iron oxide nanoparticles.[109, 162] Additional studies are needed to further characterize the release, though there are exciting opportunities for cytosolic delivery of genetic material and other macromolecules.

One of the benefits of the passive loading used here is the drug can be loaded in its native form without any chemical medication. By comparing the efficacy of the free drug against the delivery via SPIO, the IC50 was only marginally increased, most likely due to release kinetics rather than a loss in drug function. The higher IC50 could be mitigated by increased accumulation of the drug to the tumor through SPIO delivery. While a synergistic response could not be determined with the combination of MFH and DOX-SPIO delivery, nevertheless, our results suggest that a combinatorial treatment is more effective than using either treatment alone. Furthermore, the drug delivery kinetics coupled with the narrow window of synergistic behavior seen in **Fig. 3-10** could mask the potential for a synergistic response.

Besides drug loading, the phospholipid-PEG's main function is to impart favorable pharmacokinetics to the nanoparticle and thus the drug cargo. Stability in biological fluids, prevention of macrophage recognition, and proper size are all necessary for *in vivo* performance following systemic injection. The 28 nm hydrodynamic diameter is within the ideal size range to avoid glomerular filtration in the kidney (> 6nm) and small enough to extravasate through fenestrations within the tumor endothelial layer for EPR targeting (<100 nm).[163, 164] Thus, the long circulation half-life (~100 minutes) seen with our SPIO allows for multiple passes through the circulation to enable accumulation within the tumor (**Fig 3-16**). Although the fluorescent signal in the tumor indicates SPIO accumulation, MFH requires high iron concentrations to reach therapeutically viable temperatures for cancer treatment. An intratumoral delivery strategy was used to attain the local SPIO concentration needed for MFH and is described in Chapter 6.

Conclusion

Conventional chemotherapy of cancer is often compromised by systemic toxicity and hyperthermia alone does not have the required efficacy for therapeutically viable cancer treatment. To address these limitations, in this work, we demonstrate that phospholipid-PEG coated SPIOs have the potential to concurrently deliver Doxorubicin and generate heat for an enhanced multimodal cancer treatment. We investigated the role of PEG length in both treatment modalities, and identified phospholipid-PEG 2000 as the optimal coating that offers a high drug loading capacity of 30.8 ± 2.2% w/w (DOX/iron). We found that the phospholipid-PEG coated SPIOs were capable of raising the local temperature to apoptotic levels and a sustained DOX release without affecting drug activity. The multimodal hyperthermia-DOX treatment delivered by these SPIOs was more effective in causing cell death over the individual modalities. This SPIO-based approach offers many potential benefits for more effective cancer treatment. In addition to the capability of combined chemotherapy and hyperthermia, the superparamagnetic property of the SPIOs

provides T_2 contrast for magnetic resonance imaging (MRI) as well as the ability to accumulate in specific tissues or organs by applying an external magnetic field locally.[8, 9, 11, 13, 165] The phospholipid-PEG coating can also facilitate specific cell targeting by covalently attaching targeting ligands to the PEG chain, and fluorescence imaging by loading a lipophilic dye into the coating layer.[9, 65] Therefore, by utilizing these multifunctional abilities, it is possible to integrate diagnostic imaging with targeted drug delivery and hyperthermia to track drug-loaded SPIOs *in vivo* and further enhance the efficacy of cancer treatment by increasing specific accumulation of SPIOs in tumor.

CHAPTER 4

DEVELOPING SUPERPARAMAGNETIC IRON OXIDE NANOPARTICLES FOR HYPERTHERMIA-INDUCED CONTROLLED RELEASE

Abstract

Superparamagnetic iron oxide nanoparticles (SPIOs) are a unique drug delivery platform able to generate a local stimuli (heat) deep within the body which could be used to trigger a payload release mechanism. To investigate this potential, we synthesized SPIOs with a mixed coating composition of different phospholipid (DPPC) and phospholipid-polyethylene glycol conjugates (DSPE-PEG 2000) molar ratios using the dual solvent exchange technique. The mixed coating composition did not alter loading of the dye rhodamine 6G nor heat generation through magnetic fluid hyperthermia. Further, the phase transition of the DPPC was not observed when integrated in our SPIO system. This study demonstrates the flexibility of the dual solvent exchange method to control the incorporation of different amphiphilic molecules into the SPIO coating layer.

Introduction

Chemotherapy is currently one of the most common forms of treatment for patients with various forms of cancer. Although existing anti-cancer drugs are effective in inhibiting tumor growth and killing cancer cells, patients often suffer significant side effects which can be as harmful as the cancer itself. For this reason, better localization and accumulation of chemotherapy agents in the tumor through controlled drug release could avoid systemic toxicity and enable a higher therapeutic dose, leading to better efficacy and reduced side effects.

Nanoparticle-based drug delivery was envisioned to address the systemic toxicity problem by favorable biodistribution into the tumor through the enhanced permeability and retention effect and active targeting mechanisms such as the attachment of cancer cell-specific ligands to the surface of the particle. Initial results with liposomal carriers showed some improvement over free drug administration, leading to the development of the FDA approved DOXIL, but clinical outcomes did not reach expected levels.[75] Most nanoparticle delivery systems rely on concentration gradients to drive drug release, so release begins upon entering circulation and also occurs in nonspecific tissues where the nanoparticles accumulate. Furthermore, the initial burst release characteristic of many of these systems can cause a majority of the drug to be released during the circulation time. Therefore, uncontrolled release could potentially offset the advantages of using nanoparticle carriers.

To achieve better control of drug delivery when using nanoparticle carriers, a number of controlled release mechanisms have been studied such as enzymatically degradable and pH sensitive drug release methods which take advantage of the abundance of specific enzymes or the low pH found in the tumor microenvironment.[10, 166, 167] Other methods employ an exogenous activation modality such as light, ultrasound, or heat to trigger the drug release.[168-170] Thermal sensitive liposomes utilized phase transition lipids in their construction for enhanced release when brought above a specific temperature.[171-174] A critical factor with stimuli-responsive release is the source of the activation energy and ensuring that the stimulus can reach the location of the drug carrier *in vivo*, providing sufficient energy to trigger the release mechanism. A novel strategy to address this spatial issue is to couple the energy source and drug carrier regionally. The most well-studied of these coupled systems involve gold nanoparticles which convert infrared light to heat, triggering a release of the drug payload.[175-177] Gold nanoparticle are able to convert light energy to heat at high efficiencies, but limited by the penetration depth of light through tissue.

Superparamagnetic iron oxide nanoparticles (SPIOs) have been proposed as a drug delivery agent that can overcome the penetration limitations of other systems since their heat generation is mediated by exposure to an alternating magnetic field (AMF) which is not attenuated by biological tissue. The majority of the work on temperature-sensitive coatings for SPIOs has focused on the phase transition polymer poly(N-isopropylacrylamide) (PNIPAM),[178-183] but the biocompatibility of PNIPAM has come under question.[184] Further, the release profiles following phase transition only show moderate increases in the release rate over those measured at body temperature, so alternative phase transition coatings are sought after.[185] Phospholipids are naturally occurring molecules that make up the cell membrane and their PEG conjugates have been widely used in liposome and micelle nanoparticle formulations.[59, 60, 76, 186] Phospholipids have a sharp phase transition from a conformationally ordered gel phase to a conformationally disordered liquid fluid phase which coincides with a 20% decrease in size.[187] The phase transition temperature for these molecules can be tuned to above body temperature for thermally controlled release by varying the chain length and the phosphate head group of the molecule.[188, 189] Temperature sensitive liposomes have shown promising results by taking advantage of this phase transition for a controlled release of doxorubicin, but they require an exogenous heat source to trigger the release.[171, 190, 191]

This study aimed to develop a thermo-responsive coating for SPIOs to enable a specific and effective release through magnetic fluid hyperthermia. To this end, we incorporated a 16 carbon chain lipid (DPPC), whose transition temperature is 41^{o}C, into the DSPE-PEG coating of our SPIOs. Although a temperature dependent release was not observed with the inclusion of DPPC, the particles could still achieve high loading capacities and heat generation and demonstrate the potential to tailor the coating composition.

Methods

Synthesis of iron oxide nanoparticles

Iron oxide nanoparticle cores of 14 nm diameter were synthesized by an adapted published procedure.[29] Iron acetylacetonate (12 mmol), 1,2-hexadecanediol (60 mmol), oleic acid (72 mmol), and oleylamine (72 mmol) were mixed in benzyl ether (60 ml) in a 500 ml round bottom flask and magnetically stirred. A vacuum was applied for 40 minutes, then the solution was raised to 120^{o}C by a heating mantle attached to a temperature controller. After another 40 minutes, the vacuum was removed and replaced by a flow of Nitrogen. The solution was then raised to 200^{o}C and held for 2 hours before ramping to 300^{o}C and holding for 1 hour. The solution was then cooled to room temperature and ethanol (240 ml) was added to separate and precipitate the nanoparticle cores via three rounds of centrifugation. Finally, the cores were redispersed in toluene.

Dual solvent exchange coating method

To coat 1 mg Fe of SPIOs, 200 µl of the ferrofluid at 5 mg/ml Fe was varying ratios of 1,2-dipalmitoyl-sn-glycero-3-phosphocholine (DPPC) and 1,2-distearoyl-sn-glycero-3-phosphoethanolamine-N-[amino(polyethylene glycol)-2000] (DSPE-PEG-amine) in 400 µl of chloroform in a 100 ml round bottom flask. The amount of coating molecules was determined based on a ratio of 8 coating molecules per nm^2 SPIO surface area. Then, 4 ml of DMSO was incrementally added followed by a 30-minute incubation at room temperature. The toluene and chloroform was removed via vaporization under vacuum. Afterwards, 20 ml of deionized water was then slowly added to the solution. DMSO was removed and replaced with deionized water through three rounds of centrifugation in Vivaspin 20 centrifugal filter tubes with molecular weight cut-off 100 kDa (Sartorius, Goettingen, Germany). Finally, the solution was passed through a 0.2 µm HT Tuffryn

syringe filter membrane (Pall Life Sciences, Ann Arbor, MI) and stored in deionized water at 4^{o}C.

Iron concentration measurement

Iron content of samples was determined using a ferrozine assay. Briefly, 50 µl of sample was mixed with 50 µl of 12 M HCl and incubated at room temperature for 30 minutes. Then, 240 µl of 2 M NaOH, 50 µl of 4 M ammonium acetate, 110 µl 5% hydroxylamine HCl, and 500 µl water were added to the solution sequentially. After 30 minutes of incubation, 50 µl of the solution were mixed with 0.02% ferrozine solution in a 384 well plate. Light absorption was read at 562 nm with 810 nm as the reference wavelength using a microplate reader (Safire2, Tecan Group Ltd., Männedorf, Switzerland). The absorption was compared to a molecular iron standard to determine the concentration. The number of SPIOs per gram of iron was estimated to be 1.35E17 based on the volume of a spherical 14 nm diameter SPIO and the density of magnetite (5.17 g/cm^3) assuming the cores were made up of Fe_3O_4.

Characterization

Transmission electron microscopy (TEM)

The average core diameter of the SPIOs was measured via transmission electron microscopy. The polymer coating layer on the SPIOs was visualized by negative staining with phosphotungstic acid on glow discharged copper grids prior to imaging. TEM images were recorded with a transmission electron microscope (Hitachi H-7500, Tokyo, Japan) connected to a CCD camera. The negative staining and TEM procedures were conducted by the Robert P. Apkarian Integrated Electron Microscopy Core at Emory University. The images were analyzed using ImageProPlus® software.

Quantification of total lipid on SPIOs

The amount of lipid coating molecules (DPPC and DSPE-PEG-amine) was quantified based on the phosphate concentration. Each of the lipids contains a phosphate group. To release the phosphate group from the lipid molecule, 50 µg Fe of coated SPIO was pipetted into a glass test tube and heated in an oil bath to 100°C to evaporate the water. 300 µl of perchloric acid was then added to each sample and heated to 160°C for 20 min. The samples were then allowed to cool to room temperature before adding 300 µl of 10 N NaOH followed by 2.4 ml of DI water to neutralize the perchloric acid. The total phosphate in the solution was then quantified with a Malachite green phosphate detection assay kit (R&D Systems) using a standard made of free DSPE-PEG-amine. The phosphate concentrations were then normalized to the amount of SPIO in the solution as measured by a ferrozine assay.

Quantification of DSPE-PEG-amine on SPIOs

The amount of DSPE-PEG-amine on the SPIOs was measured using a fluorescamine assay. Briefly, the SPIO samples were dispersed in PBS at 100 µg/ml Fe and then 200 µl was pipetted into a 96-well quartz plate. To each well, 50 µl 3 mg/ml fluorescamine dispersed in acetone was added and incubated for 20 minutes. The fluorescence intensity was then measured with a microplate reader (ex = 395, em = 470). The data was compared against a standard composed of DSPE-PEG-amine and 100 µg/ml Fe of DSPE-PEG-coated SPIOs and normalized to the amount of SPIO in the solution as measured by a ferrozine assay.

Dynamic light scattering

The hydrodynamic diameter of the coated SPIOs was measured using a dynamic light scattering device (DynaPro Nanostar, Wyatt Technology, Santa Barbara, CA). The SPIOs were dispersed in deionized water at 100 µg/ml Fe and measured at 25°C. The mass-weighted size distribution was reported.

Differential scanning calorimetry

The phase transition temperature was measured using a differential scanning calorimeter (TA DSCQ200, TA Instruments, New Castle, DE). A 20 µl sample of coated SPIO at 300 µg/ml Fe was prepared in a hermetically sealed aluminum pan and measured with a temperature range of 25 – 65^{o}C and heating rate of 10^{o}C min^{-1} under a nitrogen atmosphere. A reference water sample was used to normalize the heat flow data. The pans were equilibrated in the DSC cell at 25^{o}C for 10 minutes before the heating run.

Dye loading

SPIOs were incubated for 24 hours at 100 µg/ml overnight at 4^{o}C in a solution containing 40 µg/ml Rhodamine 6-G to allow for incorporation into the coating. The loading capacity was determined by centrifuging the SPIOs and separating the top and bottom fractions for dye absorbance and iron concentration measurements with a UV-vis spectrophotometer and a colorimetric ferrozine assay, respectively.

Dye release

The drug release profile was characterized by first concentrating 200 µg Fe of dye loaded SPIOs through a 2100 g centrifugation for 30 min. The supernatant was removed to take out any free dye in solution and replaced with 400 µl of fresh DI water. 200 µl samples were then transferred to a 96-well plate along with equivalent concentration free dye controls. The transient absorbance was measured at 525 nm using a microplate reader with a measurement time of 30 minutes and 1 minute read intervals. For the hyperthermia release measurements, a 15 minute temperature ramp to 43^{o}C was added to the beginning of the measurement procedure.

Hyperthermia properties

A 1 ml volume of coated SPIOs at 0.4 mg/ml Fe was placed inside a polystyrene-insulated 7.5-turn, 2.54 cm inner diameter inductor coil (EasyHeat 2.4kW, Ameritherm, Scottsville,

NY). An alternating magnetic field (23.77 kA/m, 355 kHz) was generated within the coil, causing the SPIOs to produce heat. The resulting temperature rise in the ferrofluid was measured over three minutes with a fiber optic temperature probe (FLUOTEMP, Photon Control Inc., Burnaby BC, Canada) and recorded in real time. The slope of the linear region of the temperature vs. time plot was normalized to a water sample and used to calculate the SAR using the equation below:

$$SAR = \frac{1}{m_{Fe}} C_{H_2O} m_{H_2O} \left(\frac{dT}{dt}\right)$$

where m_{Fe} is the mass of the iron in the sample, C_{H_2O} is the specific heat of water, m_{H_2O} is the mass of the water, and $\frac{dT}{dt}$ is the temperature rise of the fluid.

Results

Nanoparticle synthesis

Superparamagnetic iron oxide cores were synthesized using a thermal decomposition technique to produce monodisperse iron oxide cores of 6 nm in diameter stabilized with an oleic acid oleylamine surfactant layer.[51] To confer aqueous solubility to the nanoparticle cores, the SPIOs were coated with a combination of 1,2-dipalmitoyl-sn-glycero-3-phosphocholine (DPPC) and 1,2-distearoyl-sn-glycero-3-phosphoethanolamine-N-[amino(polyethylene glycol)-2000] (DSPE-PEG-amine) at different percentages (0-75%) of the total lipid using a dual solvent exchange method.[64] The presence of the coating layer was confirmed through TEM imaging of the coated SPIOs negatively stained with phosphotungstic acid, as demonstrated by the white halos surrounding the dark iron oxide cores (**Fig. 4-1A,B**). Comparing the TEM images, the incorporation of DPPC does not appear to change the coating coverage on the SPIOs.

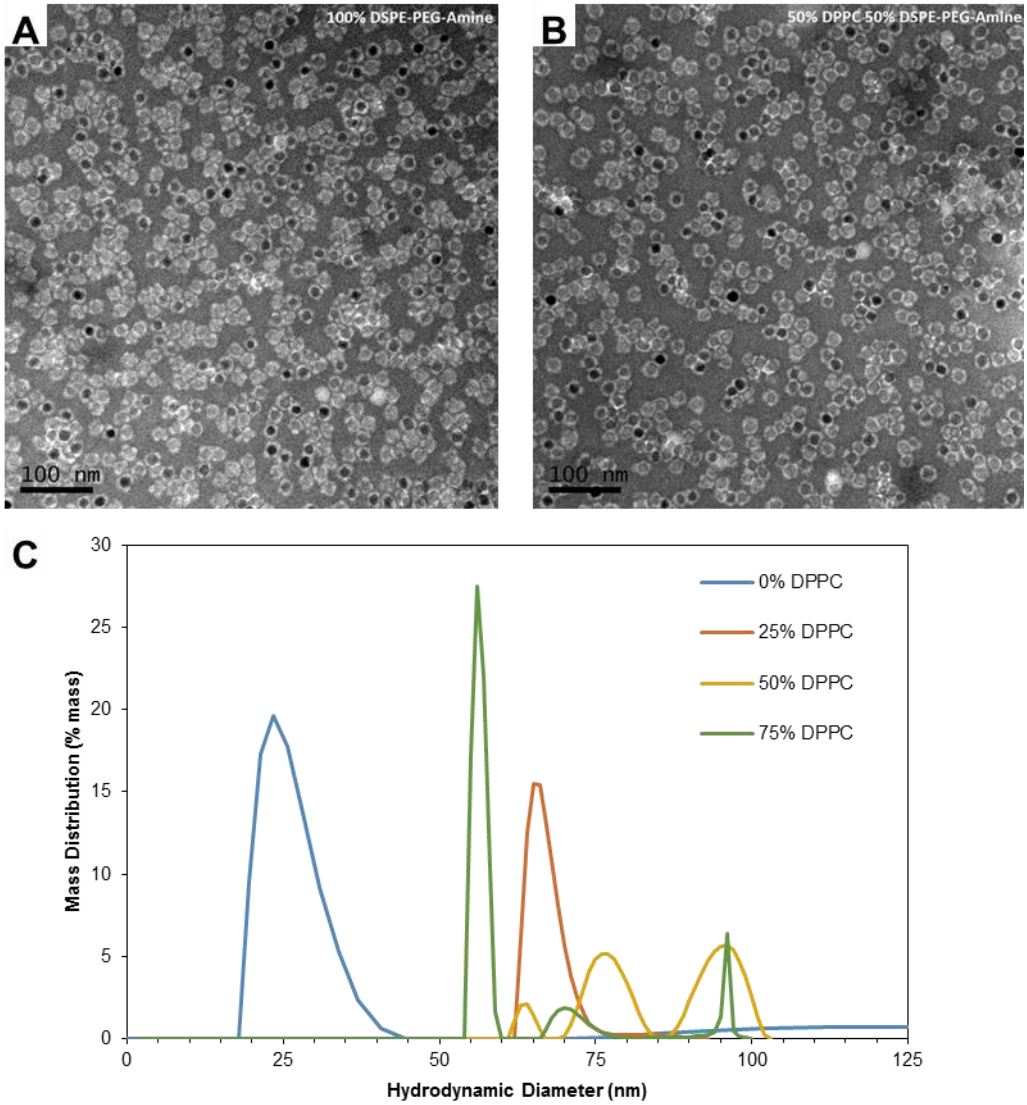

Fig. 4-1 Size measurements of iron oxide nanoparticles. Negatively stained TEM images of SPIOs coated with (A) 100% DSPE-PEG-Amine and (B) 50% DSPE-PEG-Amine and 50% DPPC. (C) Hydrodynamic size measurements of coated SPIOs measured by dynamic light scattering.

Size measurements

To examine the hydrodynamic diameter of the particles after coating, the sizes of the particles were measured using dynamic light scattering. The 0% and 20% DPPC cores displayed a single sharp peak at 23 and 66 nm, respectively, while the rest of the DPPC samples displayed multiple peaks between 50-100 nm (**Fig. 4-1C**). The 23 nm hydrodynamic diameter displayed by the 0% DPPC cores is consistent with the estimated size of the DSPE-PEG-amine coating (~14 nm) and suggests stable, single cores surrounded by the phospholipid-PEG coating. The larger sizes of the 25-75% DPPC coated SPIOs suggests clustering of the iron oxide cores within the phospholipid coating. The lack of clustering in the TEM images could be masked by artifact from the sample preparation. The change in coating above 20% DPPC is in agreement with a study of DPPC/DSPE-PEG micelles which saw a sharp increase in aggregation numbers and size above the 20% DPPC mark.[186]

Coating composition

To investigate how the initial ratios of DPPC to DSPE-PEG-amine used in the coating process relate to the final surface composition of the coated SPIOs, the relative amount of amine groups to total phosphates was measured for the 0, 25, 50, 75% DPPC samples. The amine and phosphate content were measured using a fluorescamine assay and malachite green assay, respectively, using standards made with free DSPE-PEG-amine and then normalized to the iron content measured with a ferrozine assay. As the DPPC percentage was increased from 0 to 75%, the phosphates per nanoparticle increased linearly from 3000 to 6900 (**Fig. 3-3a**). To determine the surface density of the coating molecules, the number of phosphates was related to the surface area of the nanoparticles and found to increase from 3.74 to 8.58 phosphates per nm^2 between 0 to 75% DPPC (**Fig. 3-3a**). For amine content, the opposite trend was seen as the number of amines per particle decreased from 2860 to 1080 for 0 to 75% DPPC, corresponding to a decrease of 1.78 to 0.67 amines

per nm^2 (**Fig. 3-3b**). The amine content displayed a large decrease between 0% and 25% DPPC which corresponds to a fifty percent reduction in amines with smaller changes for 50% and 75% DPPC. The total number of amines for the 0% DPPC SPIOs (2860 amines per particle) was consistent with the total number of phosphates (3000 phosphates per particle) which follows that all of the phosphates on those particles should be contributed by the DSPE-PEG-amine. The percentage of DSPE-PEG-amine to total phospholipid on the particles was determined by normalizing the amine quantities to the total phosphates and found to be 95%, 38%, 22%, and 16% for the 0, 25, 50, 75 % DPPC SPIOs.

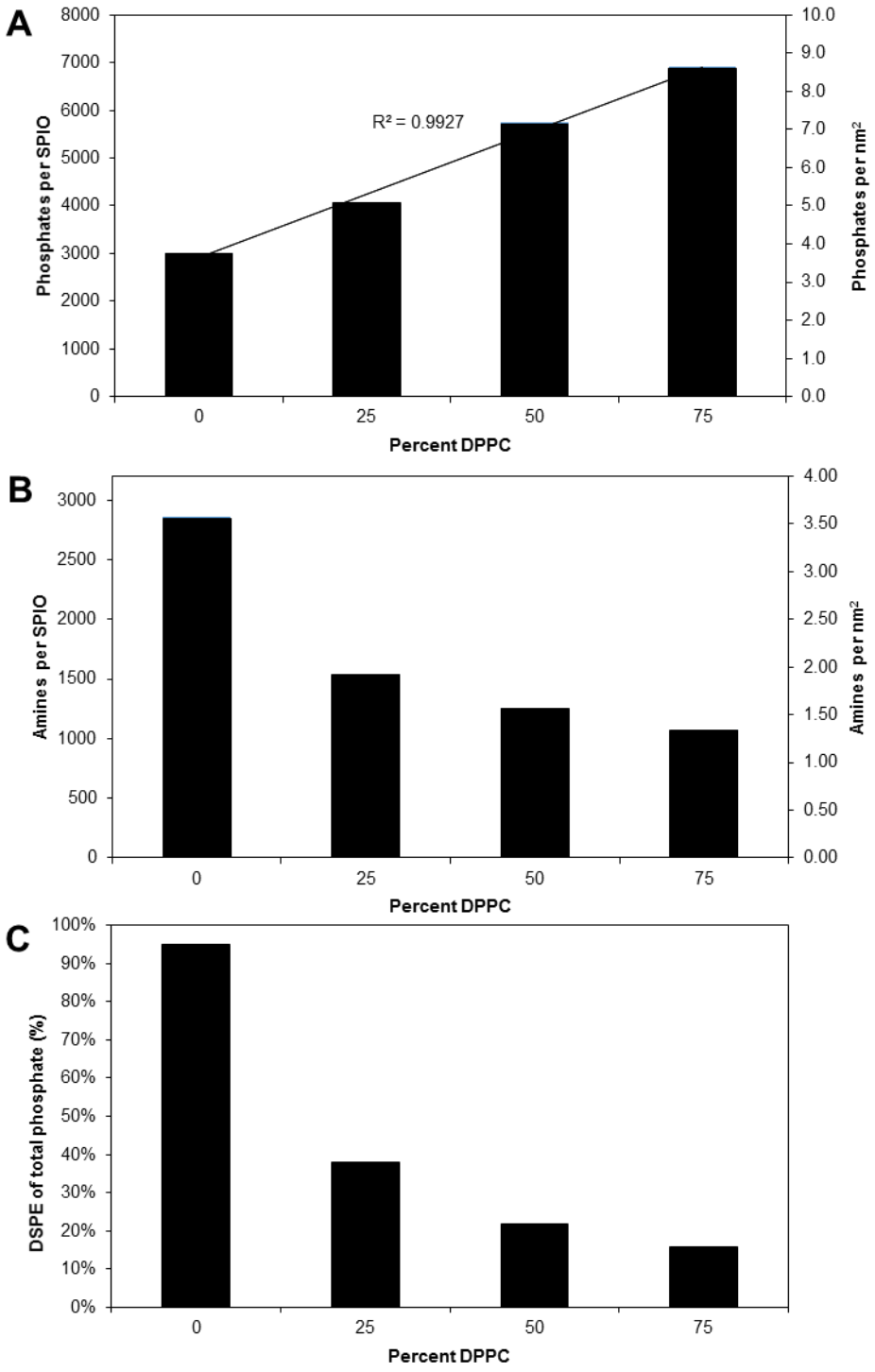

Fig. 4-2 Coating composition of nanoparticles. (A) Malachite green phosphate measurements and (B) fluorescamine amine group measurements of SPIOs coated with varying percentages of DPPC and DSPE-PEG-amine. (C) Calculated percentage of DSPE of total coating molecules based on phosphate and amine measurements.

Phase transition temperature

To examine the phase transition temperature of the lipids coating the SPIOs, endothermic transitions of the 75% DPPC SPIO sample were measured with a differential scanning calorimeter (DSC). The lack of a clear endothermic peak indicates that a phase transition could not be identified in this manner (**Fig. 4-3**).

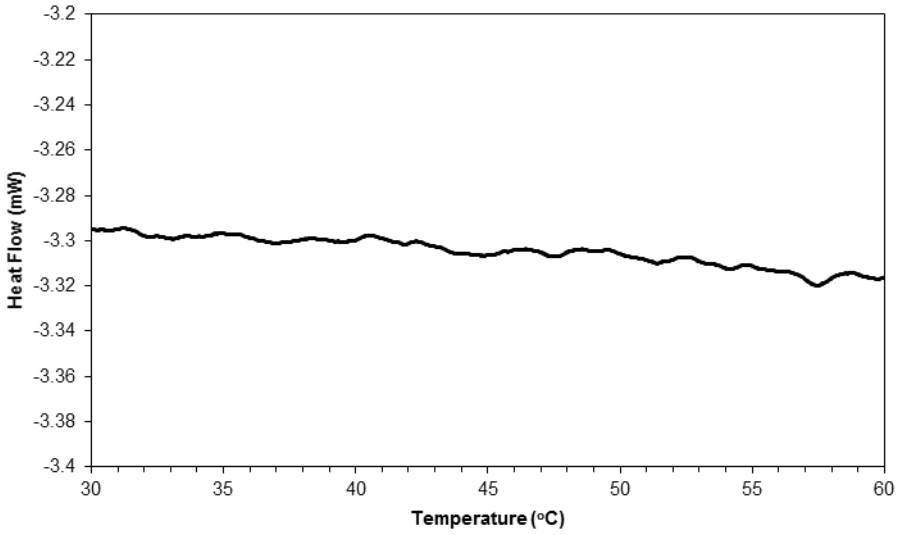

Fig. 4-3 Differential scanning calorimetry scan of 75% DPPC SPIOs.

Dye loading

The dye rhodamine 6G was used as an analog for a poorly soluble drug to determine loading and release properties with the DPPC SPIOs. The dye was mixed with the SPIOs and incubated overnight for the dye to partition into the hydrophobic lipid layer due to hydrophilic/hydrophobic interactions. The loading ratio was ~4.5% w/w dye/Fe for the three DPPC percentage samples tested, suggesting that the addition of DPPC to the coating layer did not affect the loading kinetics for rhodamine 6G (**Fig. 4-4A**).

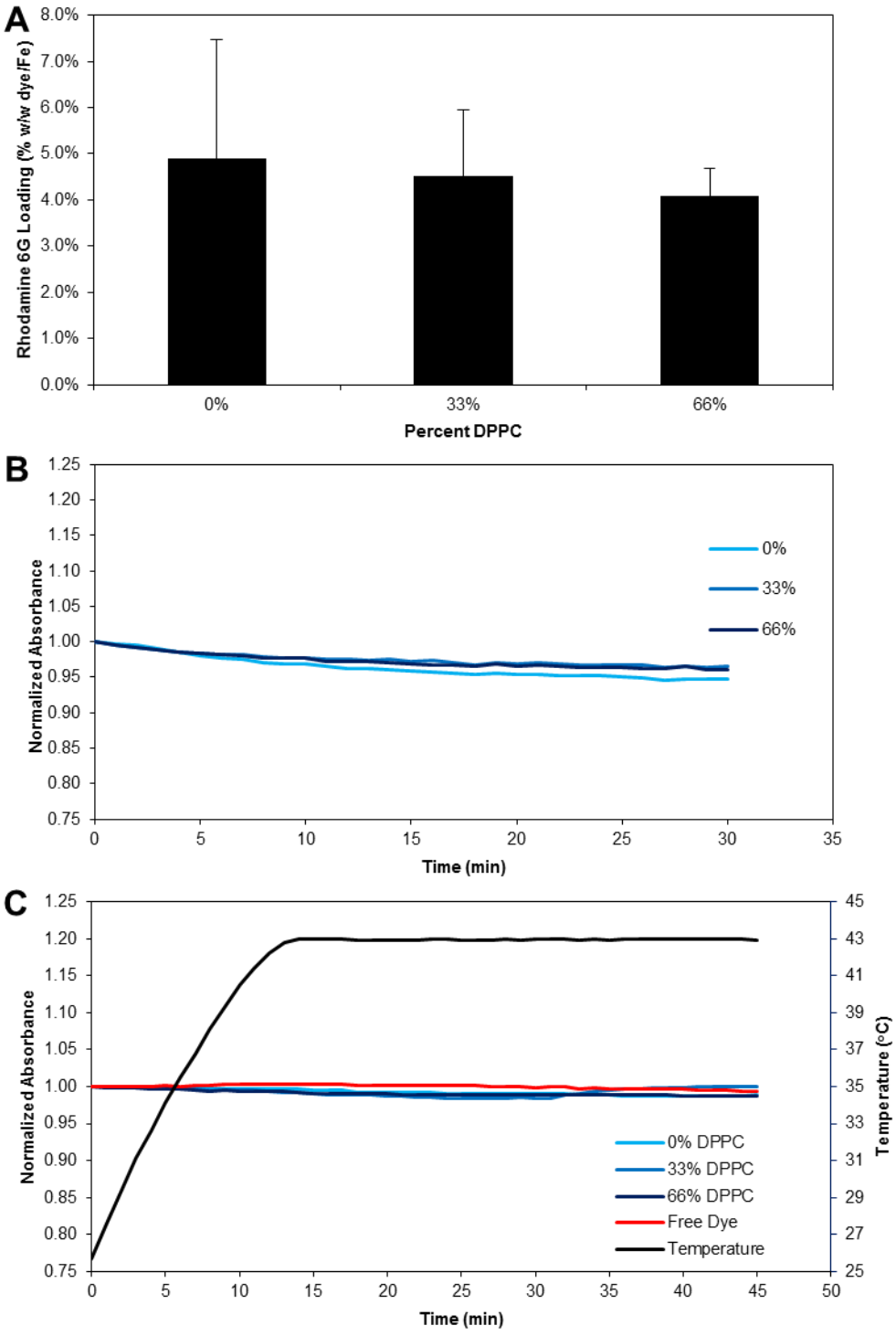

Fig. 4-4 Rhodamine 6G loading and release from DPPC/DSPE-PEG coated SPIOs. (A) Loading capacity of 0, 33, and 66% DPPC coated SPIOs following 24 hour incubation. Transient changes in normalized dye absorbance at (B) room temperature and (C) ramp to 43^{o}C. Error bars represent standard error.

Dye release

The existence of a temperature-dependent release of rhodamine 6G from the DPPC SPIOs was tested by monitoring transient changes in the dye absorbance resulting from precipitation of the dye molecule in the aqueous environment. There was no detectable change in the rhodamine signal throughout the measurement time at 25^{o}C suggesting that the dye remained within the SPIO coating and was not released (**Fig. 4-4B**). When heated to 43^{o}C, there was still no change in absorbance which is in agreement with the DSC results that did not display evidence of a phase transition in this temperature range.

Coating composition effect on heat generation

To examine if the coating composition of the SPIOs affects their efficiency in magnetic fluid hyperthermia applications, the specific absorption rates of the SPIOs was compared. The specific absorption rates ranged between 220-360 W/g, but there were no significant differences between the DPPC coating compositions (**Fig. 4-5**).

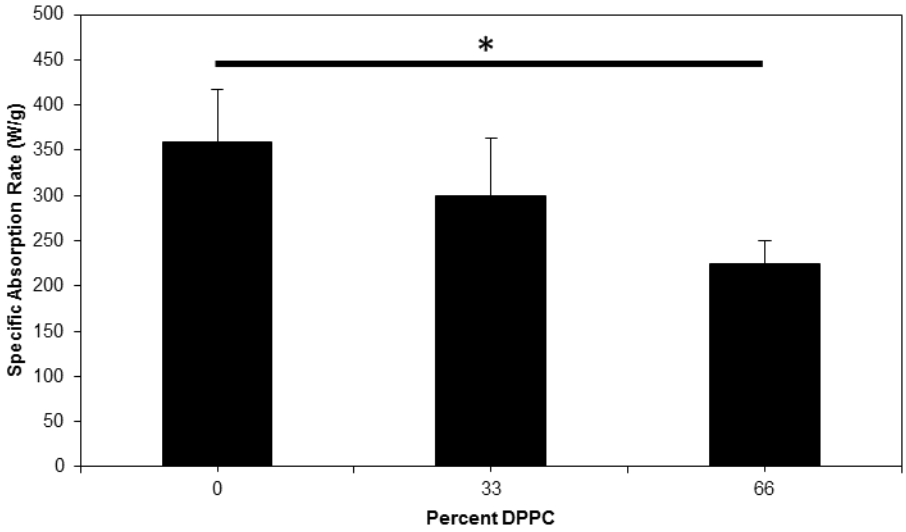

Fig. 4-5 Specific absorption rates of 0, 33, and 66% DPPC coated SPIOs determined by heating aqueous samples during exposure to an alternating magnetic field of 23.77 kA/m and 355 kHz. Error bars represent standard error. * = No significant difference (one-way ANOVA $p>0.05$)

Discussion

DPPC was incorporated into the phospholipid-PEG coating of SPIOs with the goal of thermosensitive release. Replacing some of the phospholipid-PEG with DPPC compromised the stability of the coated SPIOs as noted by the large size and multimodal populations (**Fig 4-1**). The dual solvent exchange coating process is governed by the amphiphilic nature of the phospholipid-PEG coating molecules to trigger self-assembly in polar solvents. The lack of the long hydrophilic PEG chain on the DPPC molecules may not be amphiphilic enough for single core coating to be energetically favorable.[192] The poor coating was also evident in the low yield of the SPIOs after coating which limited the breadth and extent of the subsequent experiments. These results suggest that while incorporation of other molecules into the coating layer is possible, careful consideration of the amphiphilicity is required when replacing large amounts of the DSPE-PEG.

Despite the heterogeneous size distributions, the initial lipid ratios used in the coating translated well to the final relative lipid surface composition on the SPIOs, illustrating the fine level of control possible with the dual solvent exchange coating method. The increasing lipid surface density with increasing DPPC percentage suggests that there is less steric hindrance and/or electrostatic repulsion from the small, neutral charge head group of the DPPC compared to the long PEG chain on the DSPE-PEG-amine. The lack of the long PEG chain on the DPPC could allow the molecule to fit into gaps on the SPIO surface which the DSPE-PEG would be too large for. It is worth noting that the higher lipid surface density conflicts with the larger hydrodynamic size for the DPPC particles, as an increase in size would reduce the total surface area for the same number of particles. The sharp drop in the amine density with only a low percentage of DPPC suggests that initially the DPPC replaces positions originally held by the DSPE-PEG-amine on the SPIO surface, but a certain amount of hydrophilic PEG is needed for the structure to be structurally stable. The stability of the micelle-SPIO structure is in contrast to liposomes whose phospholipid bilayers do not rely upon large amounts of PEG for stabilization.

Both dye loading and heat generation were unaffected by the DPPC. Ashok et al. observed a similar trend in the solubilization of the drug diazepam in mixed DPPC/DSPE-PEG 2000 micelles, but with DPPC/DSPE-PEG 5000 micelles, increasing DPPC coating composition corresponded to a two-fold higher drug loading.[186] In comparison to a similar study involving micelles composed of DSPE-PEG and DPPC, the incorporation of DPPC increased loading of the poorly soluble drug paclitaxel by 50% for the same lipid concentration.[140] The differences in loading seen with our SPIO system could reflect either the unique structure of the lipid layer surrounding the iron oxide or specific interactions of drugs with the phospholipid.

The large differences in hydrodynamic radius with increasing DPPC percentages would suggest that the heat generation is occurring through Néelian relaxation which is unaffected by coating size. If the increase in size is attributed to clustering of iron oxide cores within phospholipid-PEG micelles, there should be magnetic interactions between the closely spaced magnetic cores that would alter the heat generation, further putting into question the dynamic light scattering data.[193, 194]

Taken together, the lack of a noticeable endothermic peak in the differential scanning calorimetry measurements and unchanging rhodamine absorbance throughout heating to 43^{o}C preclude the potential for temperature sensitive release with the mixed DPPC coating. With the limited amount of material available for the DSC measurement, the instrument could have lacked the sensitivity required to accurately register a phase transition in the sample. On the other hand, it has been shown in mixed lipid/lipid-PEG bilayers that increasing the molar percentage of lipid-PEG reduces the main transition enthalpy, and the reduction is exacerbated with longer lipid and PEG lengths.[188, 189, 195] The DSPE-PEG percentage of coating may still be too high even with 75% DPPC to elicit a sharp phase change response at the relevant hyperthermia temperatures.The dye release study confirms that the SPIOs are insensitive to the temperature change, though a longer dialysis release study with a larger amount of sample could be more accurate.

Conclusion

In this study we have demonstrated a well-controlled incorporation of DPPC and DSPE-PEG through the dual solvent exchange coating method. The initial coating ratios between the DPPC and DSPE-PEG matched well with the final composition of the SPIO coatings, though the stability of the SPIO structure at higher DPPC percentages is debatable. The poorly soluble dye rhodamine 6G was loaded into the SPIOs, demonstrating the potential for loading poorly soluble drugs. Increasing the amount of DPPC in the coating did not affect drug loading nor heat generation efficiencies. In order to achieve true temperature-controlled release, incorporation of higher amounts of DPPC in relation to DSPE-PEG while maintaining particle stability may be required to show a strong phase transition through hyperthermia.

CHAPTER 5

ANALYZING THE EFFECT OF IRON OXIDE CORE SIZE ON MAGNETIC FLUID HYPERTHERMIA AND MAGNETIC RESONANCE IMAGING

Abstract

Iron oxide nanoparticles (IONP) possess the unique ability to be used in both a diagnostic and therapeutic capacity for cancer treatment by utilizing their inherent magnetic resonance contrast and potential to generate local heat when exposed to an alternating magnetic field (AMF). In order to minimize the delivered dose and ensure peak efficiency for clinical translation, the optimal design criteria for IONP are under investigation. To this end, we synthesized an extensive array of iron oxide cores from 6 to 40 nm to study the effects of core size on heat generation and MRI contrast *in vitro* and in a xenograft mouse tumor model. Heat generation and T_2 relaxivity increased linearly with core size up to 2844 W/g Fe and 850 $mM^{-1}s^{-1}$, respectively, which are the highest values recorded for IONPs. Further, the intratumoral IONP distribution could be visualized using MRI, and the 40 nm particles generated sufficient heat to reach apoptotic temperatures *in vivo*. This study demonstrates the importance of considering core size when developing IONPs for MRI and hyperthermia in cancer treatment.

Introduction

Magnetic nanoparticles have tremendous potential to improve cancer therapy and diagnostics through their heat generation and magnetic resonance contrast properties,

though current clinical use has been limited due to inadequate efficiencies in these areas. In order to achieve translational success, significant improvements in the specific absorption rate (SAR) and relaxivity of magnetic nanoparticles are required. The magnetic behavior governing SAR and relaxivity is strongly dependent on the particle core size. Recent advances in the synthesis of iron oxide nanoparticles (IONPs) through thermal decomposition have given researchers the ability to finely tune the particle size to within a few nanometers for distinct and monodisperse populations.[45, 51, 196] This level of size control prompts an in-depth, well-controlled investigation of the influence of core size to enhance magnetic fluid hyperthermia (MFH) and magnetic resonance imaging (MRI) for theranostic cancer therapy.

Magnetic fluid hyperthermia is the mechanism by which magnetic particles generate local heat when exposed to an alternating magnetic field (AMF).[106] The increased local temperature can be applied as a cancer therapy, as raising the temperature to ~43^{o}C for 30-60 minutes can trigger apoptosis in cancer cells.[88, 90, 91] Reaching the proper temperature while minimizing the delivered dose is a critical goal for effective and efficient treatment, thus optimizing the physicochemical properties of the particles for maximum heat generation has been the focus of current research in the field.[194, 197-199] For small, superparamagnetic particles (<25 nm), theoretical predictions suggest that the heating mechanism occurs through its fastest relaxation process, Néelian or Brownian, but for larger, ferrimagnetic particles, hysteretic losses dominate.[106, 200] Previous studies have found that heat generation is core size-dependent but have been relatively narrow in scope with only a small number of sizes tested without encompassing the full spectrum of sizes now obtainable with modern synthesis methods.[199, 201-204]

In the diagnostic field, magnetic particles are being developed for their contrast capabilities in magnetic resonance cancer imaging. The local magnetic fields created by IONPs when influenced by an external magnetic field accelerate the dephasing rate of Larmor precession in nearby water protons, resulting in negative contrast on a T_2-weighted MRI scan.[114, 115] Previous reported work suggests that MR contrast has a size cutoff above which the particles shift from the size-dependent motion averaging regime (MAR) to the size-independent static dephasing regime (SDR).[114, 115, 205] Specifically, work from Lee et al. indicates that increasing the size of iron oxide nanocubes above 22 nm results in decreased relaxivity, though the core size increase was coupled with a large increase in the hydrodynamic radius (>200 nm) so that the particles would be too large for either of the MAR or SDR.[206] Other studies investigating the core size effect on MR contrast have also been fairly limited in number of sizes to compare or do not take into account sizes above 20 nm.[49, 107, 207, 208] Therefore, experimental validation of the MAR and SDR transition by comparing particles systematically spanning the expected cutoff is essential for determining the optimal size for MRI applications.

Although there have been a number of solution-based studies examining the effects of core size on MR contrast and MFH, only limited efforts have examined how the size effects translate to a physiological environment. In this work, we synthesized an extensive array of stable, monodisperse IONPs ranging from 6-40 nm to enable investigation of core size-dependent parameters and to test the theoretical size regimes on both MFH and MR contrast. To date, the described work utilizes the largest range of sizes for IONPs, spanning across the presumed superparamagnetic limit.[200, 209] With this complete array of eight different sizes, we investigated the effect of core size on the MFH and MRI capability of the IONPs in solution, when incubated with cancer cells *in vitro*, and in a mouse xenograft

tumor model. Nanoparticles with a 40 nm core were determined to be the optimal size for visualization of the distribution within the tumor through MRI and for heating to apoptotic temperatures *in vivo* with a minimal injected dose of 50 μg Fe. The results of this study highlight the potential of IONP above the superparamagnetic size cutoff to deliver therapeutically viable heating and diagnostically relevant MR contrast for cancer therapy.

Methods

Chemicals

Iron acetylacetonate ($Fe(acac)_3$ 99%), 1,2-hexadecanediol (technical grade, 90%), oleic acid (technical grade, 90%), and oleylamine (technical grade, 70%), toluene (≥99.9%), chloroform (99%), dimethyl sulfoxide (DMSO 99%) benzyl ether (98%), hydrochloric acid, hydroxylamine HCl, sodium hydroxide, ammonium acetate, ferrozine, and thioglycolic acid (≥98%) were purchased from Sigma-Aldrich and used as received; 1,2-distearoyl-sn-glycero-3-phosphoethanolamine-N-[methoxy(polyethylene glycol)-2000] (ammonium salt) (DSPE-PEG 2000) were purchased from Avanti Polar Lipids.

Numerical simulations of magnetic fluid hyperthermia

Numerical simulations were conducted on Matlab using the linear response theory equations developed by Rosensweig.[106] The parameters used in the studies are based on previously determined properties in Chapter 3 and reports by Lartigue et al. and Rosensweig as shown in **Table 5-1**.[106, 107]

Table. 5-1 Magnetic fluid hyperthermia numerical simulation parameters.

Parameter	Value
Boltzman Constant	1.38E-23 m^2kg/s^2K
Temperature	298K
Magnetic Permeability of Free Space	1.26E-6
Volume Fraction of IONP	1.9E-4
Viscosity of Water	6.92E-4 Ns/m^2
τ_0	1E-9
Magnetic Saturation	437 kA/m (84.6 emu/g)
AMF Field Strength	36 kA/m
AMF Frequency	355 kHz
Magnetic Anisotropy	50 kJ/m^3

Synthesis of iron oxide nanoparticles

Iron oxide nanoparticle cores were synthesized by an adapted published procedure.[51] Iron acetylacetonate (12 mMol), 1,2-hexadecanediol (60 mMol), oleic acid (72 mMol), and oleylamine (72 mMol) were mixed in benzyl ether (60 ml) in a 500 ml round bottom flask and magnetically stirred. A vacuum was applied for 40 minutes, then the solution was raised to 120^{o}C by a heating mantle attached to a temperature controller. After another 40 minutes, the vacuum was removed and replaced by a flow of Nitrogen. The solution was then raised to 200^{o}C and held for 2 hours before ramping to 300^{o}C and holding for 1 hour. The solution was then cooled to room temperature and ethanol (240 ml) was added to separate and precipitate the nanoparticle cores via three rounds of centrifugation. Finally, the cores were redispersed in toluene.

Dual solvent exchange coating method

To coat 1 mg Fe of IONPs, 200 µl of the ferrofluid was mixed with DSPE-PEG in 400 µl of chloroform in a 100 ml round bottom flask. The amount of DSPE-PEG was determined based on a ratio of 8 DSPE-PEG molecules per nm^2 IONP surface area. Then, 4 ml of DMSO was incrementally added followed by a 30-minute incubation at room temperature. The toluene and chloroform was removed via vaporization under vacuum. Afterwards, 20 ml of deionized water was then slowly added to the solution. DMSO was removed and replaced with deionized water through three rounds of centrifugation in centrifugal filter tubes (Vivaspin 20, 100 kDa cutoff size). Finally, the solution was passed through a 0.2 µm syringe filter (Acrodisc, 0.2 µm, d13mm) and stored in deionized water at 4ºC.

SQUID magnetization measurements

Magnetization measurements on uncoated iron oxide cores were carried out using a superconducting quantum interference device (SQUID) magnetometer (Quantum Design MPMS-5S, San Diego, CA). Field-dependent magnetization curves were measured at 5 K and 300 K as a function of the external magnetic field in the range of $0\text{-}5x10^4$ Gauss.

Transmission electron microscopy (TEM)

The average core diameter of the IONPs was measured via transmission electron microscopy. The polymer coating layer on the IONPs was visualized by negative staining with phosphotungstic acid on glow discharged copper grids prior to imaging. TEM images were recorded with a transmission electron microscope (Hitachi H-7500, Tokyo, Japan) connected to a CCD camera. The negative staining and TEM procedures were conducted by the Robert P. Apkarian Integrated Electron Microscopy Core at Emory University. The average diameter of the core populations were analyzed using ImageProPlus® software.

Dynamic light scattering

The hydrodynamic diameter of the coated IONPs was measured using a dynamic light scattering device (DynaPro Nanostar, Wyatt Technology, Santa Barbara, CA). The IONPs were dispersed in deionized water at 100 µg/ml Fe and measured at 25ºC. The mass weighted diameter and polydispersity index were reported.

Iron concentration measurement

Iron content of samples was determined using a ferrozine assay. Briefly, 50 µl of sample was mixed with 50 µl of 12 M HCl and incubated at room temperature for 30 minutes. Then, 240 µl of 2 M NaOH, 50 µl of 4 M ammonium acetate, 110 µl 5% hydroxylamine HCl, and 500 µl water were added to the solution sequentially. After 30 minutes of incubation, 50 µl of the solution were mixed with 0.02% ferrozine solution in a 384 well plate. Light absorption was read at 562 nm with 810 nm as the reference wavelength using a microplate reader (Tecan Safire2, Switzerland). The absorption was compared to a molecular iron standard to determine the concentration.

T_2 relaxivity

The T_2 relaxivity of the IONPs was measured with a 0.47T Minispec Analyzer MQ20 (Bruker, Fremont, CA) using the Carr-Purcell-Meiboom-Gill (CPMB) pulse sequence. Each core size was prepared by diluting in deionized water at a range of concentrations from 0.04-0.72 mM Fe. The T_2 relaxivity was calculated as $1/T_2$ divided by the molar iron concentration by fitting the data to a linear regression.

Magnetic fluid hyperthermia

A 1 ml volume of coated IONPs at 400 µg/ml was placed inside either a 5-turn, 2.54 cm inner diameter or 5-turn, 5.00 cm inner diameter (large coil) inductor coil which was insulated with polystyrene (Ameritherm 1kW, Scottsville, NY). An alternating magnetic field with a field strength of 23.8 kA/m or 13.3 kA/m, for the 2.54 cm and 5.00 cm coils respectively, and a frequency of 325 kHz was generated within the coil, causing the IONPs

to produce heat. The resulting temperature rise in the ferrofluid was measured with a fiber optic temperature probe (Lumasense m3300, Oakland, NJ) and recorded in real time. The slope of the linear region of the temperature vs. time plot was normalized to a water sample and used to calculate the SAR using the equation below:

$$SAR = \frac{1}{m_{Fe}} C_{H_2O} m_{H_2O} \left(\frac{dT}{dt}\right)$$

where m_{Fe} is the mass of the iron in the sample, C_{H_2O} is the specific heat of water, m_{H_2O} is the mass of the water, and $\frac{dT}{dt}$ is the temperature rise of the fluid.

MRI solution phantom

Aqueous solutions of each of the core sizes were prepared at 5 µg/ml and a water control. MR imaging was performed using a Bruker 7 T small animal MRI instrument with a 60 mm surface coil (Pharmascan, Bruker). The samples were imaged using a spin-echo sequence (TR = 1000 ms. TE 67.5 ms, matrix size = 256×256, FOV = 4 cm).

Cell culture

U87 glioblastoma cells were obtained from ATCC, USA and cultured in T75 cell culture dishes following ATCC instructions. Cells were grown in Dulbecco's Modified Eagle's Medium (DMEM) (Sigma-Aldrich) supplemented with 10% fetal bovine serum (ATCC). Cultures were replenished with fresh media every other day and passaged upon reaching 70% confluence.

In vitro magnetic hyperthermia treatment

500,000 U87 cells were put into cryovials along with either 6, 19, or 40 nm IONPs at 200 µg/ml or untreated and suspended in media with 10 mM HEPES. Each condition had a –MFH and +MFH sample, and the –MFH samples were put in the cell culture incubator while the +MFH samples were placed in the 5.00 cm inductor coil surrounded by

polystyrene insulation. The +MFH samples were exposed to an AMF (13.3 kA/m, 325 kHz) for one hour. Following the treatment, the –MFH and +MFH cells were seeded into 96 well plates at 15,000 cells per well. After 24 hours, the cell viability was measured using an MTT assay. Briefly, the media in the wells was replaced with phenol red-free DMEM with 0.5 mg/ml MTT (3-(4,5-dimethylthiazol-2-yl)-2,5-diphenyltetrazolium bromide, Invitrogen) and incubated at 37ºC for 2 h. The formazan crystals were dissolved in 200 µl of DMSO and the absorbance was read at 570 nm with 810 nm as the reference. The cell viability was normalized to the untreated control.

To visually study cell death, 20,000 cells were seeded into a –AMF or +AMF strip of a 96 well stripwell plate and left overnight for attachment. The media was replaced with fresh media, or media with 200 µg/ml Fe of 6 nm, 19 nm, or 40 nm IONP. The –AMF strips were put in the cell culture incubator while the +AMF strips were placed in the 5.00 cm inductor coil surrounded by polystyrene insulation. The +AMF strips were exposed to an AMF (13.3 kA/m, 325 kHz) for one hour and then returned to the incubator. After 24 hours, the cells were stained with propidium iodide (PI, 4 µM) and calcein AM (2 µM) for 30 minutes at room temperature. The cells were then imaged under a confocal microscope.

Glioblastoma xenograft tumor model

All animal procedures were conducted with the approval of the Institutional Animal Care and Use Committee at the Georgia Institute of Technology. Xenograft tumors are induced in athymic nude mice by subcutaneously injecting 3M U87 cells suspended in PBS into the right flank. Tumors were monitored until they reached the appropriate size for experimentation.

In vivo magnetic fluid hyperthermia

Tumor-bearing mice with tumors ~750 mm^3 in size were anesthetized with 1.5% isoflurane and injected intratumorally with either 10 µl of 6, 19, 40 nm IONPs (50 µg Fe) or saline

over 10 minutes using a syringe pump. The animal was then placed within the large inductor coil and the fiber optic temperature probe was inserted into the center of the tumor cannulated with an 18G syringe needle. The animal was then exposed to an AMF (13.3 kA/m, 325 kHz) for one hour while recording the intratumoral temperature.

In vivo MR imaging

In vivo MR imaging was performed using a Bruker 7 T small animal MRI instrument with a 38 mm surface coil (Pharmascan, Bruker). Tumor-bearing mice were imaged using a spin-echo sequence (TR = 1000 ms. TE increased from 12 ms to 144 ms with an increment of 12 ms. Matrix size = 256×256, FOV = 30 mm). Images were taken before and after intratumoral injection of IONPs (50 µg in 10 µl), and following the 1 hour AMF treatment.

Tumor Growth

Tumor-bearing mice with tumors ~175 mm^3 in size were anesthetized with 1.5% isoflurane and injected intratumorally with 10 µl saline, IONP (5 mg/ml Fe), IONP-DOX (5 mg/ml Fe, 1.7 mg/ml DOX), or free DOX (1.7 mg/ml DOX) over 10 minutes using a syringe pump. The IONP mice were further divided into –/+MFH groups with the +MFH mice undergoing a one hour AMF exposure (13.25 kA/m, 325 kHz) following IONP injection. Tumors were measured daily via calipers and the size was determined by calculating the volume of an ellipsoid using two axis:

$$V = \frac{4}{3}\pi a b^2,$$

where V is volume, a is the larger axis radius and b is the smaller axis radius. Mice were sacrificed at the end of one week or if the size reached 1.5 cm in either direction.

Results

Magnetic fluid hyperthermia theoretical parameter dependencies

An initial investigation of the core size effect on heat generation in relation to both intrinsic and extrinsic properties of MFH was conducted. For single domain superparamagnetic IONPs, the linear response theory can be used to estimate the heat generation from Néelian or Brownian relaxation. Néelian relaxation describes the realignment of the particle's magnetic moment with the external field by overcoming the anisotropic energy barrier. The relaxation time is a product of the anisotropy constant *K*, nanoparticle core volume V_M, and temperature T:

$$\tau_N = \frac{\sqrt{\pi}}{2}\tau_0 \exp\left(\frac{KV_M}{k_BT}\right) / \sqrt{\left(\frac{KV_M}{k_BT}\right)},$$

where τ_0 is generally 10^{-9}s. The competing relaxation process, Brownian, involves the physical rotation of the particle to align the dipole with the field direction and operates on the characteristic time:

$$\tau_B = \frac{3\eta V_H}{k_BT},$$

where η is the viscosity of the solution and V_H is the hydrodynamic volume.[106, 210] The faster of the two processes determines the total relaxation time according to $1/\tau = 1/\tau_N + 1/\tau_B$, and for an aqueous solution of phospholipid-PEG SPIOs, the relaxation time with respect to core size is given in **Figure 5-1**. Néelian relaxation clearly dominates for particles smaller than ~12 nm and above this size, Brownian relaxation takes over.

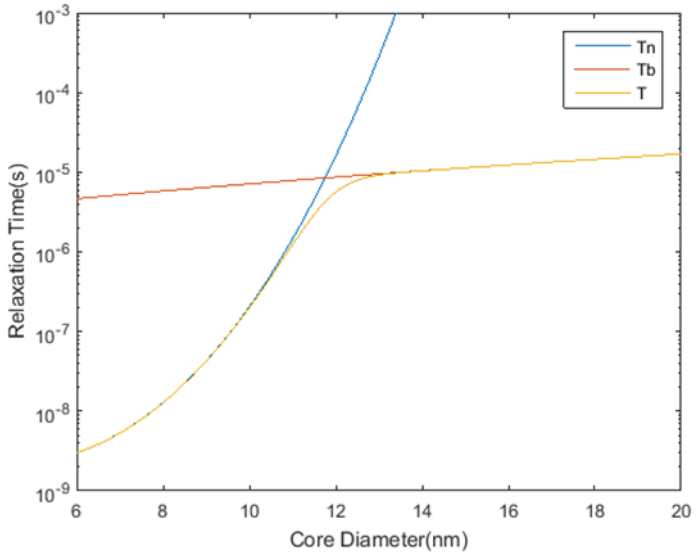

Fig. 5-1 Effect of core size on relaxation times estimated for an aqueous solution of phospholipid-PEG coated SPIOs at room temperature (K=50 kJ/m^3).

All nanoparticles have some degree of polydispersity within their populations. Knowing the strict size dependency on heat generation, it was important to understand how controlling the polydispersity through improved synthesis techniques could enhance MFH. Using the model developed by Rosensweig,[106] the theoretical heat dissipation could be calculated through:

$$SAR = 2\pi v \frac{\mu_0 x_0 H_0^2}{2p} \frac{2\pi v\tau}{1+(2\pi v\tau)^2},$$

where μ_0 is the vacuum magnetic permeability, p is the volume fraction of nanoparticles, τ is the total relaxation time, x_0 is the chord susceptibility, H_0 and v are the external magnetic field strength and frequency, respectively. The chord susceptibility can be expressed as $\mu_0 M_s^2 V_M H_0 / (k_B T)L(\xi)/\xi$, with $L(\xi)$ as the Langevin function, $\xi=\mu_0 M_s^2 V_M H/(k_B T)$, and M_s as the saturation magnetization of the nanoparticles. The specific absorption rate, a measure of the heat generation per mass of IONP, was estimated and plotted as a function of size and polydispersity as shown in **Fig 5-2**. The highest heating efficiencies are found in the size range of Néelian relaxation with size increases above 15

nm showing minimal heating. The strong size dependence of specific absorption rate is observed by the very narrow peak for maximum heating which drops dramatically beyond ~1 nm from the critical size. The peak broadens with increasing polydispersity, as the population distribution has more particles outside of the optimal heating size. There is also a peak shift towards smaller sizes due to Brownian relaxation remaining unchanged as core polydispersity increases and minimal Néelian heating at smaller core sizes (<6 nm).

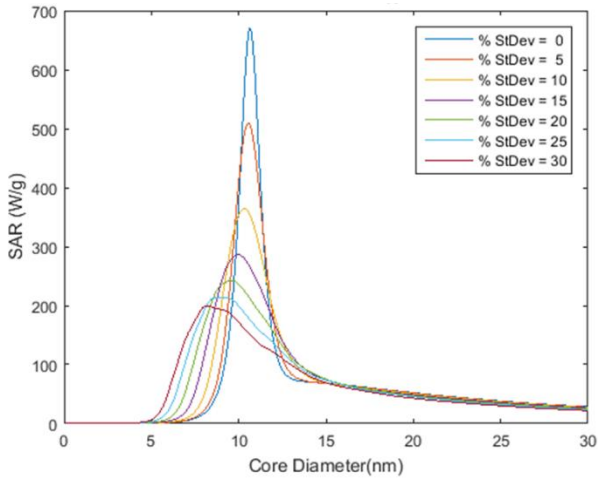

Fig. 5-2 Influence of polydispersity on magnetic fluid hyperthermia as a function of core size.

To examine the extent of magnetic anisotropy's influence on the Néelian relaxation-size relationship, a range of anisotropy values reported in the literature for iron oxide nanoparticles in the superparamagnetic size regime were modeled.[107] Increasing magnetic anisotropy of the material shifted the Néelian relaxation curves toward longer relaxation times which causes the shift to Brownian relaxation to occur at smaller particle sizes (**Fig. 5-2A**). Further, when the anisotropy was increased from 25 kJ/m^3 to 200 kJ/m^3, the size for peak heating efficiency decreased from ~14 nm to ~6.5 nm, respectively (**Fig. 5-2B**).

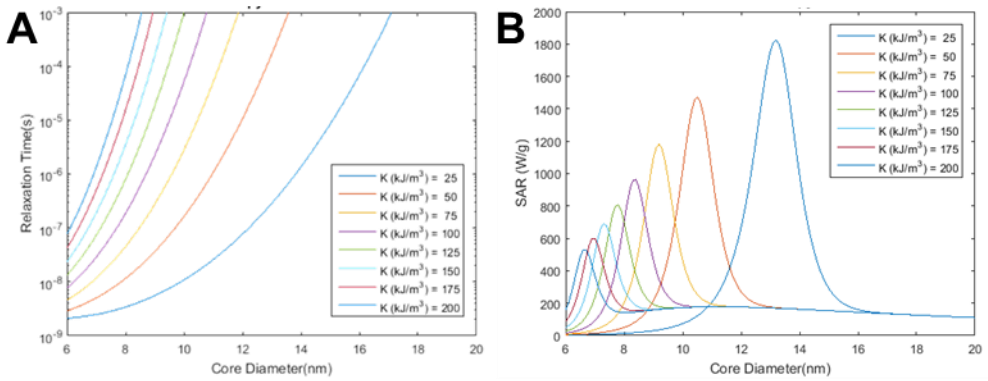

Fig. 5-3 Effect of magnetic anisotropy on (A) Néelian relaxation time and (B) specific absorption rate.

The alternating magnetic field is the extrinsic factor determining how heat generation changes with respect to core size. As shown in **Fig. 5-4**, increasing AMF frequency has a linear relationship with SAR, but also slightly shifts the SAR maximum toward smaller core sizes. In contrast, the heat generation increases proportionally to the square of the magnetic field strength, though there is no change in the optimal core size.

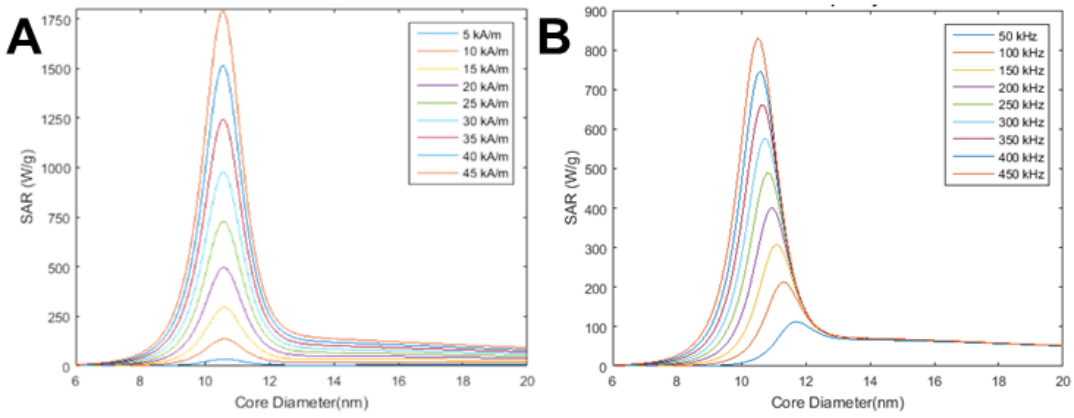

Fig. 5-4 Effect of magnetic anisotropy on (A) Néelian relaxation time and (B) specific absorption rate.

As stated previously, the linear response theory only applies to superparamagnetic single domain nanoparticles, larger multidomain and ferrimagnetic particles are assumed to generate heat through hysteretic losses which are dependent on the size of the hysteresis

loop in the MH curve rather than a direct dependence on core size.[211] While Néelian relaxation is thought to be the most efficient heating process, recent reports of IONPs in the ferrimagnetic regime and at the transition size between single and multidomain have shown remarkable heating efficiencies.[212, 213] The numerical simulations shown here prompted us to experimentally examine the core size-SAR relationship to determine the transition size between the heating mechanisms and confirm the trends observed for the different parameters.

Nanoparticle synthesis and coating

Iron oxide cores were synthesized using a thermal decomposition iterative regrowth technique to produce monodisperse iron oxide cores of 6 nm in diameter which can then be grown to larger sizes through iterative regrowth steps to achieve an array of eight different core sizes up to 40 nm (**Fig. 5-5A-H**).[51] The 40 nm size was the limit for stable and monodisperse populations that could be synthesized in this manner. The narrow core size distribution allows for valid comparison between IONP populations with average core sizes that differ by only a few nanometers and demonstrates the advantage of using the thermal decomposition synthesis method over co-precipitation methods which result in polydisperse core populations.[214]

To confer aqueous solubility and prevent protein opsonization and macrophage recognition, the IONPs were coated with phospholipid-PEG 2000 using a dual solvent exchange method.[64, 148, 149] The average size increase over the core diameter after coating (~14 nm), is consistent with the estimated size of the coating molecule (**Table 1**). The uniform size of the coating layer across the different cores is necessary to control for influences of hydrodynamic radius on the distance of water molecules to the core surface, which is important for MRI and friction induced by Brownian relaxation for MFH.[65, 106] Negative staining of the TEM grid reveals the presence of the coating layer as demonstrated by the white halos surrounding the dark iron oxide cores (Error! Reference

source not found.**I**). It is important to note that the size shown on the negative stain TEM image does not accurately reflect the hydrodynamic diameter of the IONP, since the drying process results in contraction of the PEG chains.

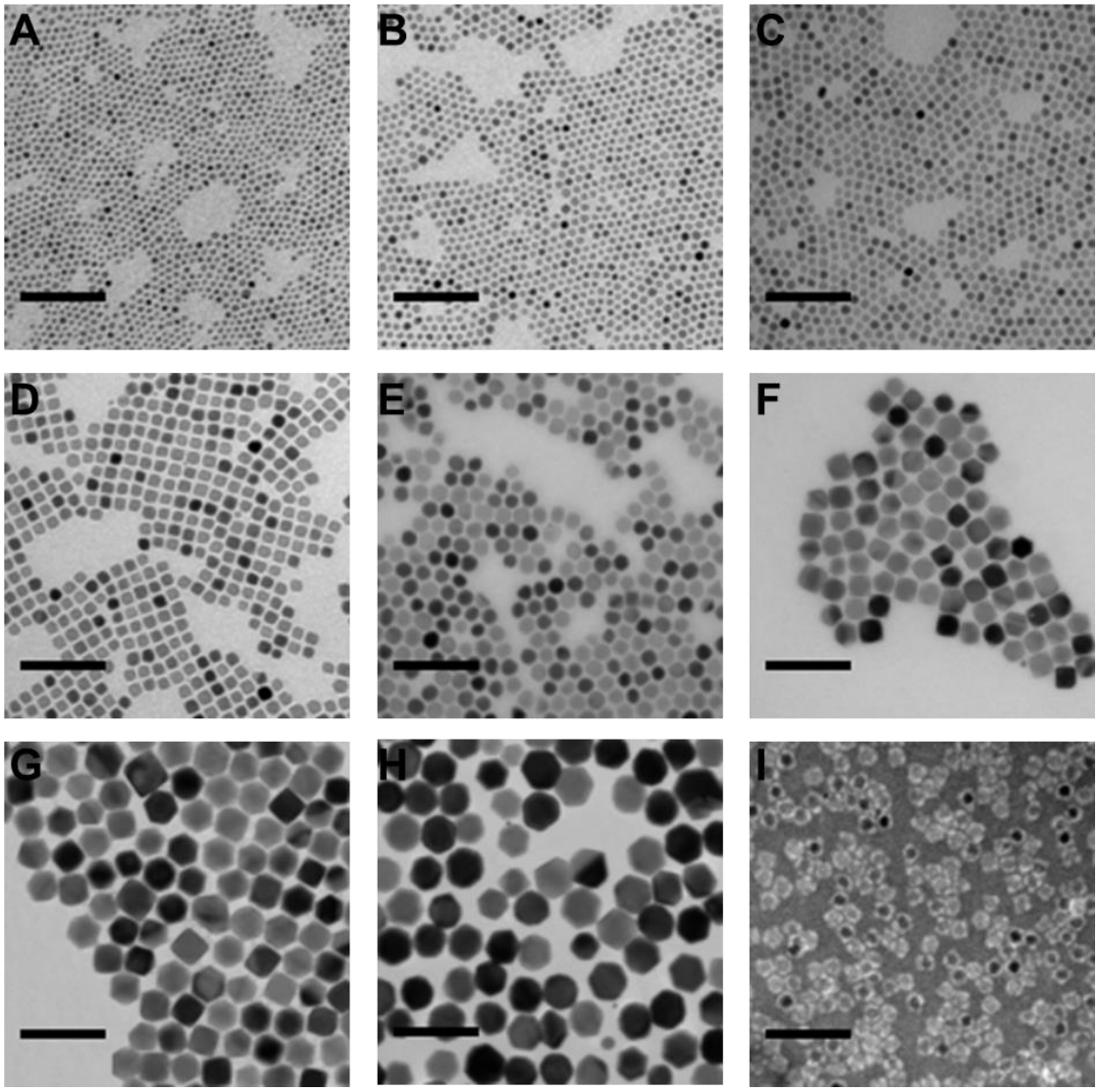

Fig. 5-5 Transmission electron microscopy images of uncoated SPIOs core: (A) 6 nm, (B) 8 nm, (C) 10 nm, (D) 15 nm, (E) 19 nm, (F) 25 nm, (G) 32 nm, and (H) 40 nm. (I) Coated 15 nm SPIOs negatively stained with phosphotungstic acid. Scale bar represents 100 nm.

Table. 5-2 Average core sizes and hydrodynamic diameters of IONP populations.

Sample	Core Diameter (nm)	Hydrodynamic Diameter (nm)	Polydispersity Index
6	5.6 ± 0.9	21.2	0.01
8	7.9 ± 1.1	20.8	0.04
10	10.3 ± 1.0	19.5	0.05
15	14.7 ± 1.4	35.8	0.08
19	19.1 ± 1.6	32.4	0.11
25	24.9 ± 2.4	37.2	0.16
32	31.9 ± 3.2	48.2	0.14
40	39.6 ± 3.8	52.4	0.01

Magnetic properties

Iron oxide particles in the nanometer size range are characterized by their superparamagnetism which describes the random orientation switching of the internal magnetic moment at room temperature due to the low thermal energy barrier.[215] The superparamagnetic property is inherently size-dependent, as above an estimated threshold diameter (~25 nm), iron oxide particles transition to a ferrimagnetic state possessing remnant magnetization, thus rendering them unsuitable for biomedical use due to self-aggregation.[209, 216-218] To assess whether the range of cores in this study remain in the superparamagnetic regime, the magnetization of the IONP samples was measured. The M-H curves for the IONPs of all core sizes exhibit superparamagnetic behavior at room temperature with no hysteresis, minimal coercivity and remanent magnetization, and high magnetic saturation up to ~125 emu/g, which approaches that of bulk magnetite (**Fig. 5-6**). The smaller cores below 10 nm in diameter exhibit a reduced saturation magnetization in contrast to larger sizes, suggesting a nonferrimagnetic frustrated surface layer having a greater influence on the total magnetization due to the larger surface-area-to-volume ratio at smaller diameters (**Fig. 5-6B)**.[203, 219-221] Comparing the 300K and 5K data, there was little change in terms of saturation magnetization and only a small increase in magnetic

remanence, suggesting the blocking temperature is above room temperature (**Fig. 5-6C,D**).To investigate the blocking temperature, the magnetizations of the cores during zero-field cooling (ZFC) and field cooling (FC) were measured. Interestingly, only the 6 and 8 nm cores displayed distinct blocking temperatures of 53K and 80K, respectively, while the magnetization of the 15 and 19 nm cores increased up through 300K (**Fig 5-7A,B**). The blocking temperature below room temperature is one of the defining properties of superparamagnetism as it implies the anisotropic energy barrier has been overcome to allow random magnetization reversals. At ~100K, the 25, 30, and 40 nm cores suddenly increase in magnetization followed by a slow increase through 300K which may indicate a mixed population of superparamagnetic and ferrimagnetic cores. The transition from the superparamagnetic single domain to the ferrimagnetic multidomain is expected to coincide with a rapid increase in coercivity, but no size dependent coercivity change was observed in the array of cores tested.[212, 222-224] Furthermore, the lack of hysteresis in the field dependent magnetization curves for all the cores provides additional evidence for superparamagnetism at room temperature. While it is difficult to properly identify the magnetic regime of the cores, the lack of remanent magnetization upon removal of the external field is the key feature needed for biomedical applications to prevent spontaneous aggregation.

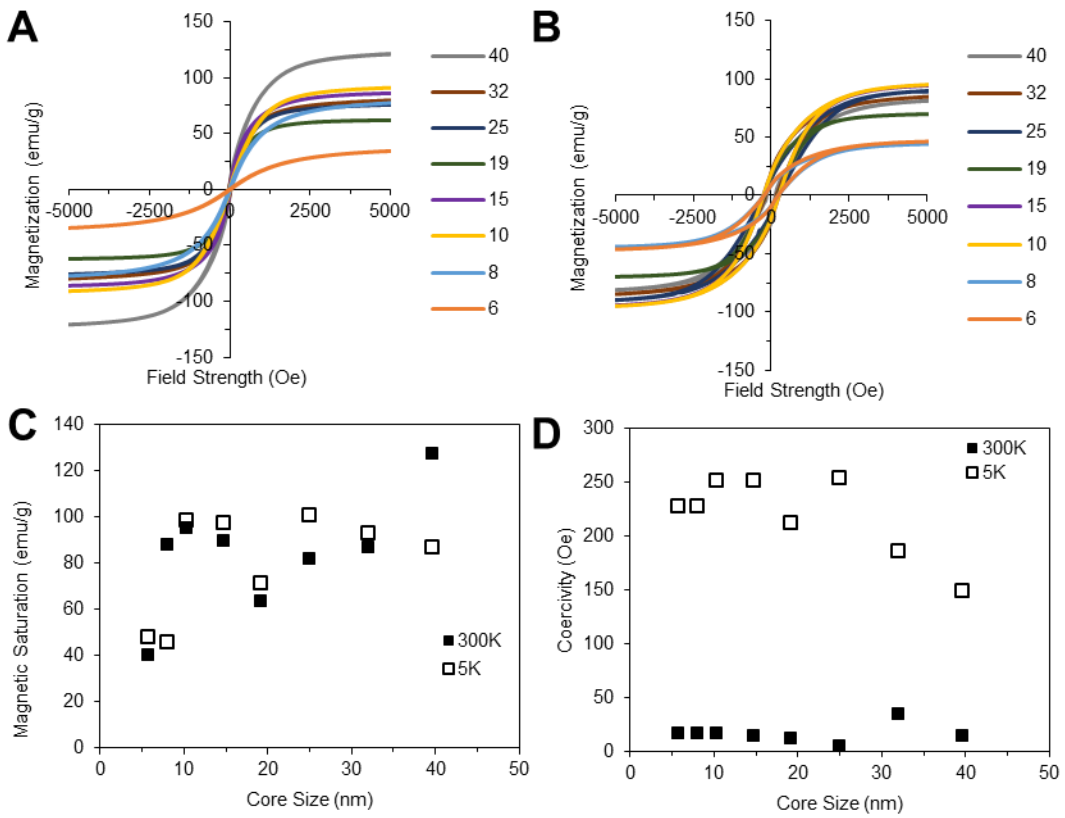

Fig. 5-6 Magnetic properties of IONP cores. Field-dependent magnetization curves at (A) 300K and (B) 5K. (C) Magnetic saturation and (D) coercivity of different core sizes at 5 and 300K.

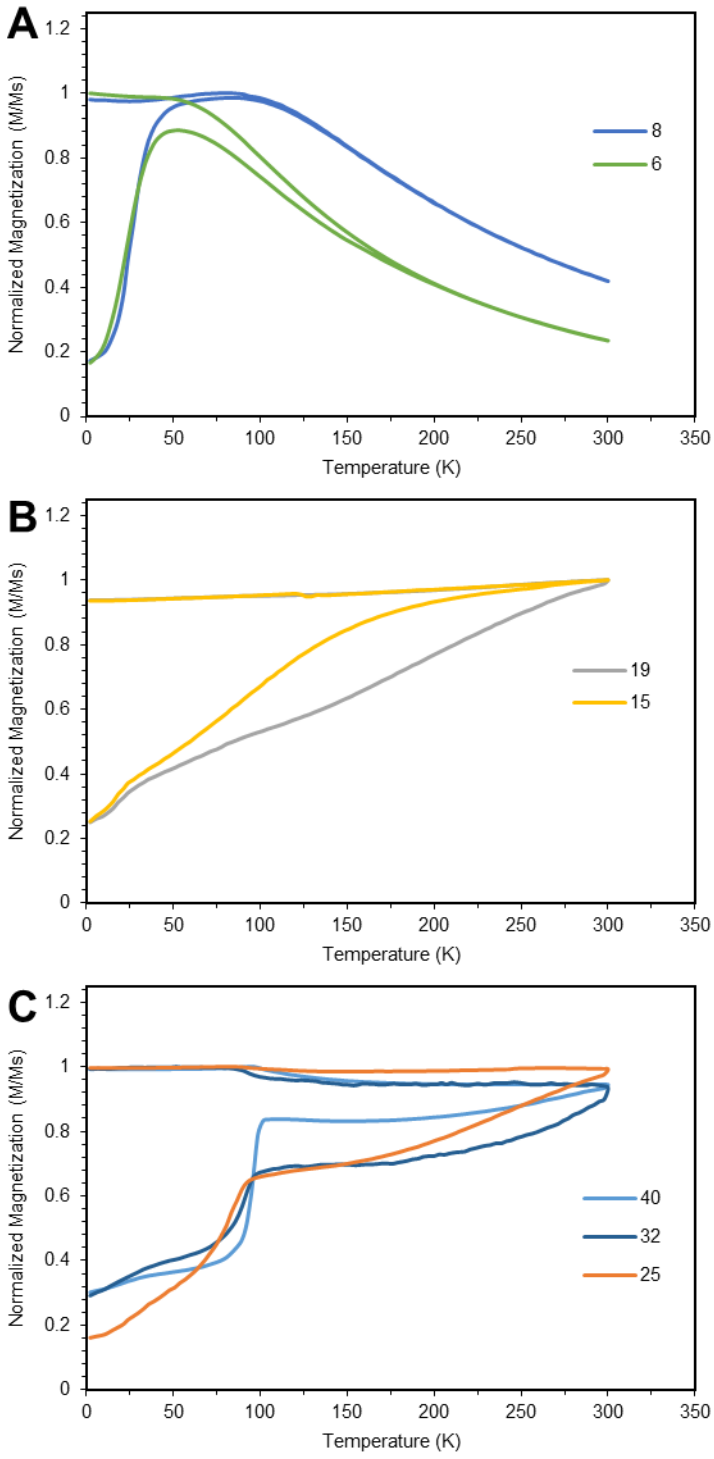

Fig. 5-7 Zero-field cooling (ZFC) and field cooling (FC) magnetic susceptibility of (A) 6 and 8 nm, (B) 15 and 19 nm, and (C) 25, 32, and 40 nm cores measured at 100 Oe.

Magnetic fluid hyperthermia properties

When magnetic nanoparticles are exposed to an alternating magnetic field, they generate heat through either hysteretic losses or a combination of Néelian relaxation and/or Brownian relaxation.[106, 107] The type of heating mechanism determines how the specific absorption rate (SAR), a measure of the heat generation per unit mass of magnetic material, is influenced by the size both in terms of the average core diameter and polydispersity of the population. For all of the cores in this study, the magnetization curves display superparamagnetic behavior with minimal hysteresis (**Fig. 5-6**) suggesting that the primary mechanism of heat generation can be attributed to Néelian and Brownian relaxation rather than hysteretic losses.[106, 107]

To determine the effect of core size on heat generation, aqueous solutions of the coated cores (400 μg Fe/ml) were exposed to an alternating magnetic field at two different field strengths (23.8 kA/m and 13.3 kA/m). The temperatures of the ferrofluids were measured as a function of time and the slopes of the heating profiles (**Fig. 5-8A,B)** were used to calculate the SAR for each of the core sizes, as described in the Methods section. By increasing the field strength from 13.3 kA/m to 23.8 kA/m, there was an average 1.99-fold increase in SAR which is roughly equivalent to the 1.79-fold difference in field strengths for the range of sizes tested (**Fig. 5-8C**). The linear increase of SAR with increasing field strength is consistent with previous studies that examined how AMF parameters relate to SAR, though is inconsistent with the theoretical predictions (**Fig. 5-4**).[204, 225] For both field strengths, there was very low heating below 10 nm and a linear relationship between core size and SAR above 10 nm in size (**Fig. 5-8C**). The consistent trend in the SAR for all the samples above 10 nm in size suggests that the same heat generation mechanism is occurring for this size range. The samples less than 10 nm in size may produce too little heat to be accurately measured with the experimental setup used. The maximum SAR was achieved with the 40 nm cores at 1535 W/g and 2844 W/g with

the 13.3 kA/m to 23.8 kA/m field strengths, respectively, and surpasses the highest reported SAR values thus far in bacterial magnetosomes and iron oxide nanocubes.[204, 226]

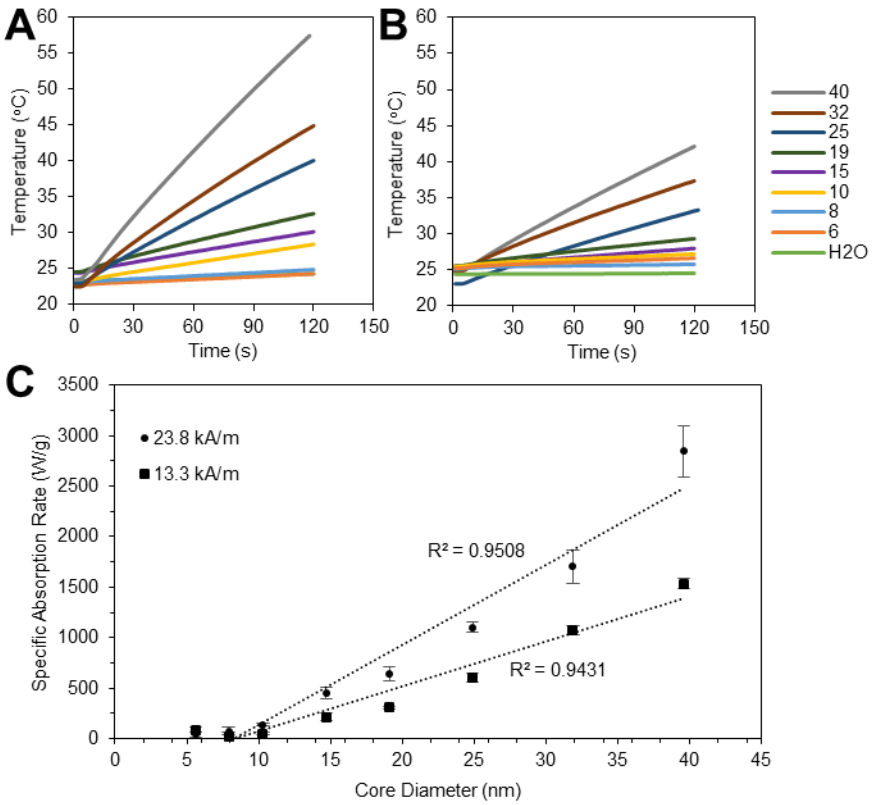

Fig. 5-8 Heat generation core size dependence. Transient heating profiles of the coated core samples for an AMF of (A) 23.8 kA/m, 325 kHz and (B) 13.3 kA/m, 325 kHz, and (C) calculated specific absorption rates. Error bars denote standard error.

To test whether Néelian or Brownian relaxation was the underlying heat generation mechanism, the SARs of IONPs with 6, 19, and 40 nm diameters suspended in a high viscosity solution was compared to the SAR values obtained in water samples (**Fig. 5-9**). The higher viscosity should increase heat generation if Brownian relaxation is dominant by increasing the rotational friction of the particles in the solution.[201] The lack of an increase in SAR with the glycerol compared to water suggests that Brownian relaxation is not a major contributing factor to heat generation and that Néelian relaxation is dominating.

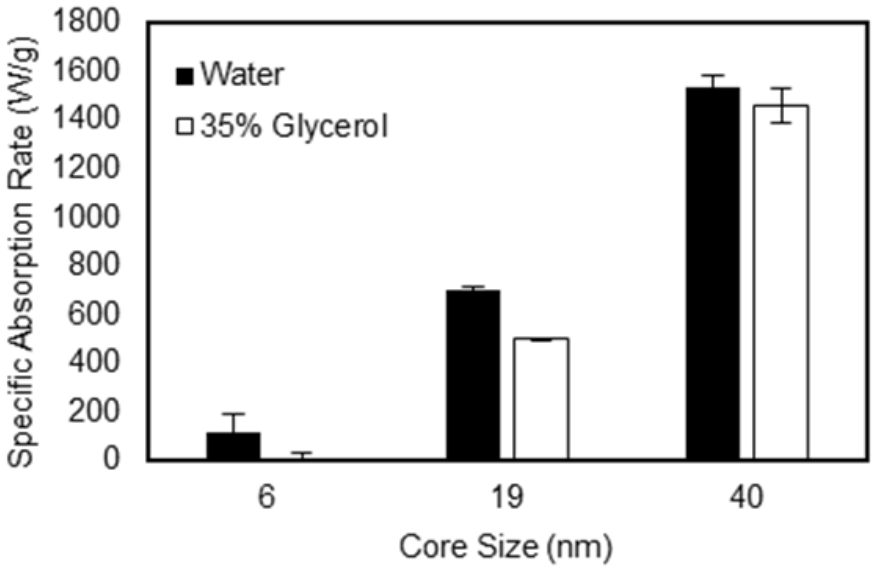

Fig. 5-9 Effect of solvent viscosity on heat generation. Calculated specific absorption rates of 6, 19, and 40 nm cores measured in water or 35% glycerol. Error bars denote standard error.

Core size effect on magnetic resonance contrast

To study the relationship between the magnetic core size of iron oxide nanoparticles and their relaxometric property for MRI, the T_2 contrast of the IONPs was assessed by measuring the T_2 relaxivity (defined as $1/T_2$ normalized by molar concentration of Fe

atoms) for each of the IONP samples at a range of iron concentrations using a 0.47 T device. A linear increase in the relaxivity was observed with respect to core size (**Fig. 5-10A,B**), with the highest relaxivity occurring in the 40 nm IONPs at 850 $mM^{-1}s^{-1}$, higher than the previously thought maximum found with iron oxide nanocubes.[206] The difference in contrast can also be visually observed in the MR image taken with a 7 T MRI scanner (**Fig. 5-10C**).

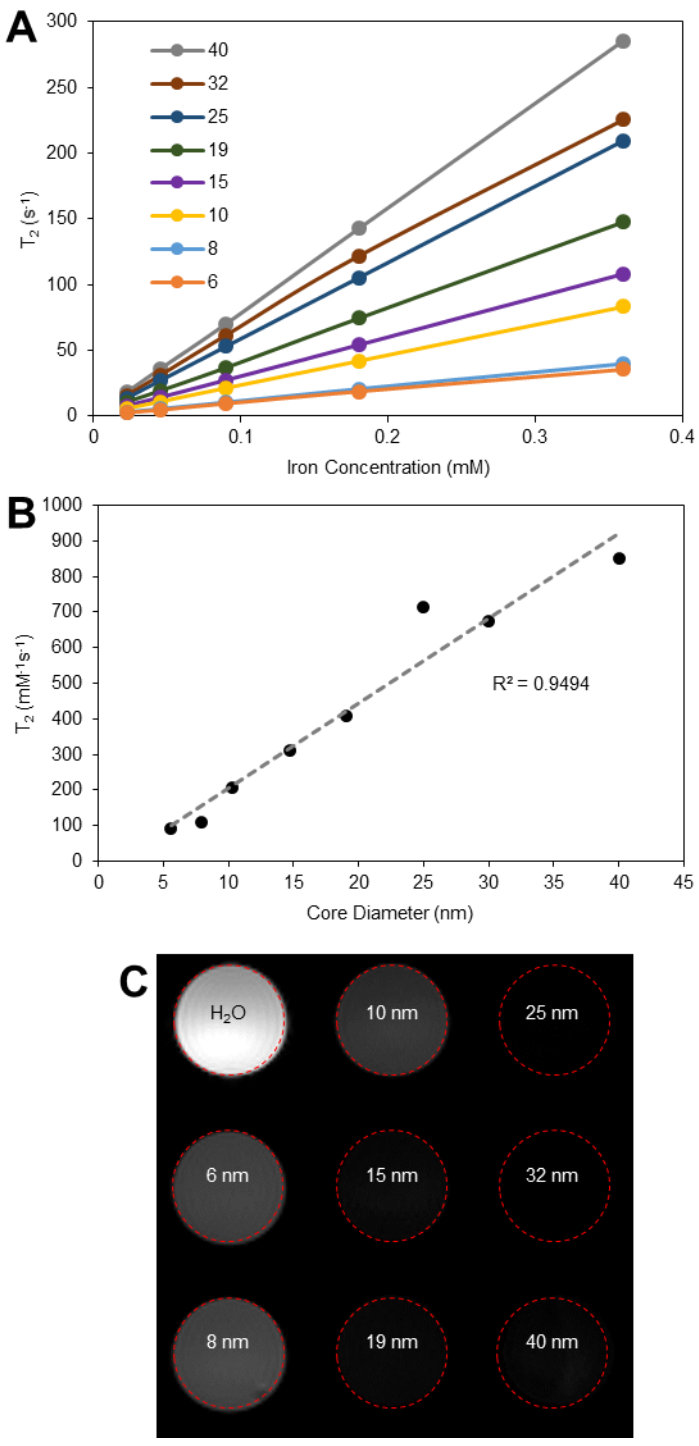

Fig. 5-10 T_2 relaxation of core sizes. (A) T_2 relaxation times, (B) T_2 relaxivity, and (C) T_2 contrast of the coated core samples at 5 µg/ml Fe.

Effect of hyperthermia on cell viability

Glioblastoma multiforme (GBM) is an aggressive and invasive brain cancer in which surgical resection is difficult to perform and thus alternative treatment measures such as local hyperthermia treatment are sought after.[227] For this reason, the U87 glioblastoma cell line was chosen to investigate the effect of core size on the efficacy of magnetic fluid hyperthermia treatment using three core sizes (6, 19, 40 nm) which encompass the general size range used in this study. AMF treatment itself did not affect cell viability, nor did the IONPs display toxicity (**Fig. 5-11A**). The effect of magnetic fluid hyperthermia ranged from little effect for the 6 nm cores, to a partial decrease (24%) in cell viability for the 19 nm cores, to complete cell death for the 40 nm cores (**Fig. 5-11A**). These cellular responses correspond to the maximum temperatures attained: 34^{o}C, 45^{o}C and 75^{o}C for the 6, 19, and 40 nm cores, respectively (**Fig. 5-11B**), as apoptosis in cancer cells is triggered between 41-46^{o}C and higher temperatures cause thermal ablation.[88-91] A live dead assay was also performed on U87 cells attached to a stripwell during AMF treatment to visually confirm the results of the MTT assay. Only cells treated with 40 nm SPIOs and exposed to an AMF displayed substantial cell death, consistent with the MTT results (**Fig. 5-12**). It is worth noting that the temperatures attained under MFH depend on IONP concentration, AMF parameters, and thermodynamics of the environment, thus the viability results illustrate the order of magnitude differences of heating between these core sizes.

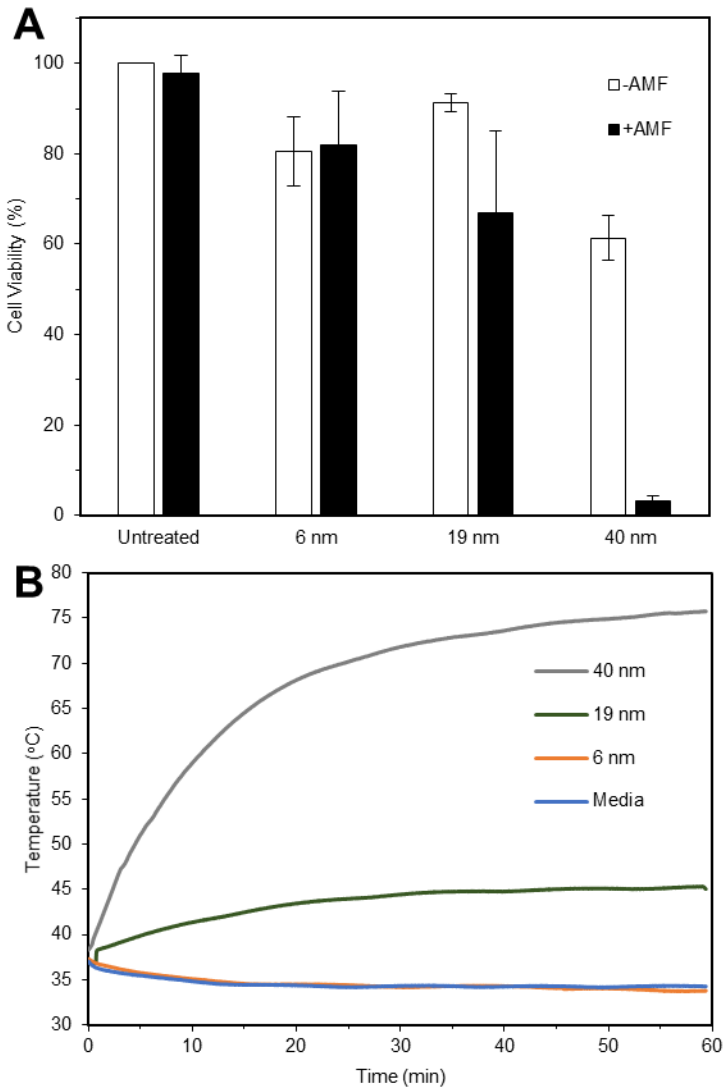

Fig. 5-11 MFH effect on cell viability. (A) Temperature profiles of SPIOs suspended in cell culture media at 200 µg/ml when exposed to an AMF (13.25 kA/m, 325 kHz). (B) Cell viability of U87 cells 24 hours after treatment of untreated media alone, 6 nm, 19 nm, and 40 nm coated SPIOs with and without a one hour AMF treatment. Measurements were taken with an MTT assay normalized to an untreated control. Error bars represent standard error.

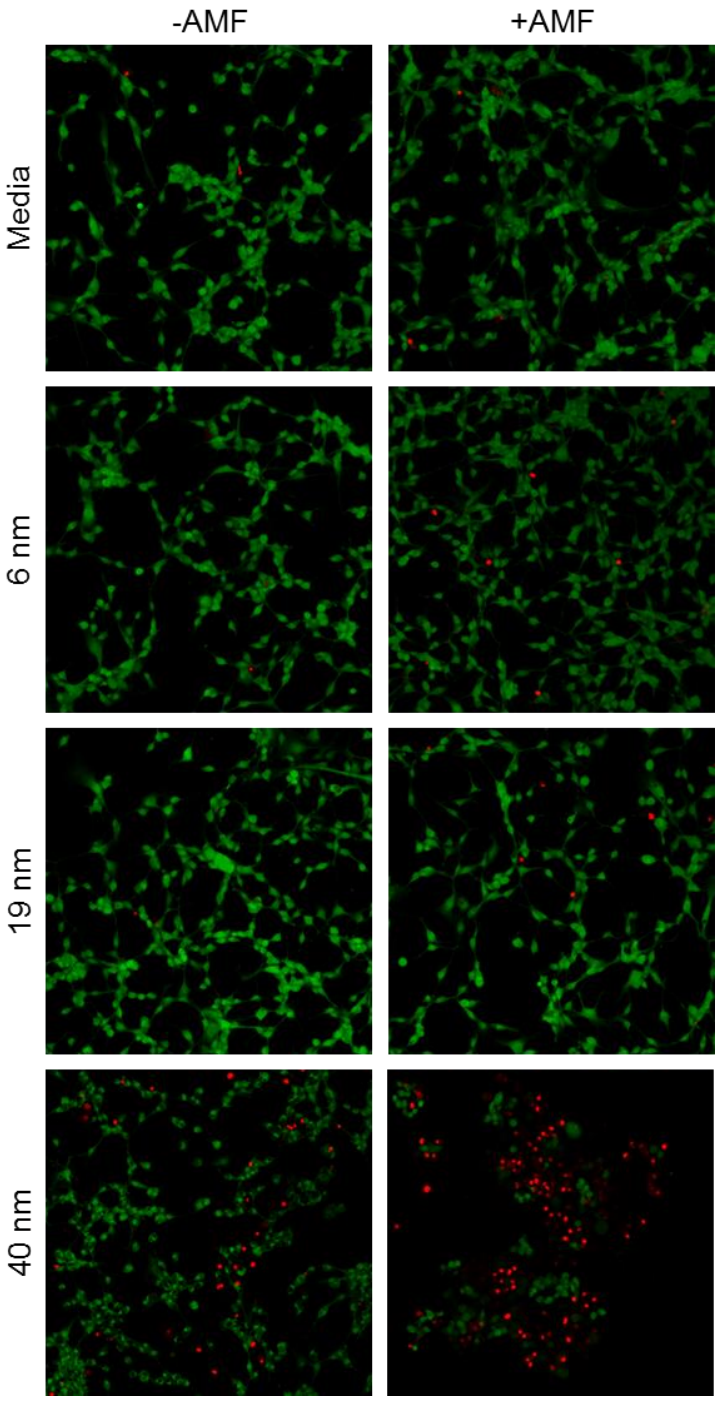

Fig. 5-12 Live/dead stain of magnetic fluid hyperthermia-mediated cell death. Confocal images of U87 cells co-stained with Calcein AM and PI 24 hours after treatment of media alone, 6 nm, 19 nm, or 40 nm coated SPIOs with and without a one hour AMF treatment in a stripwell.

In vivo magnetic fluid hyperthermia and magnetic resonance imaging

The tumor tissue represents a heterogeneous microenvironment for MRI in terms of water content and complicated thermodynamics for MFH due to homeostatic temperature regulation mechanisms which are difficult to recapitulate in an *in vitro* model. Thus, in order to evaluate the IONPs in a more clinically relevant cancer model, the three core sizes used in the *in vitro* study (6, 19, 40 nm) were tested in a mouse xenograft tumor model. U87 tumors were grown subcutaneously in athymic mice and injected intratumorally with 50 µg Fe of IONPs or 10 µl of saline. MR images taken before and after injection display the sharp contrast of the IONPs inside the tumor (**Fig. 5-13**). The border of the injection volume can be clearly seen even with the 6 nm cores.

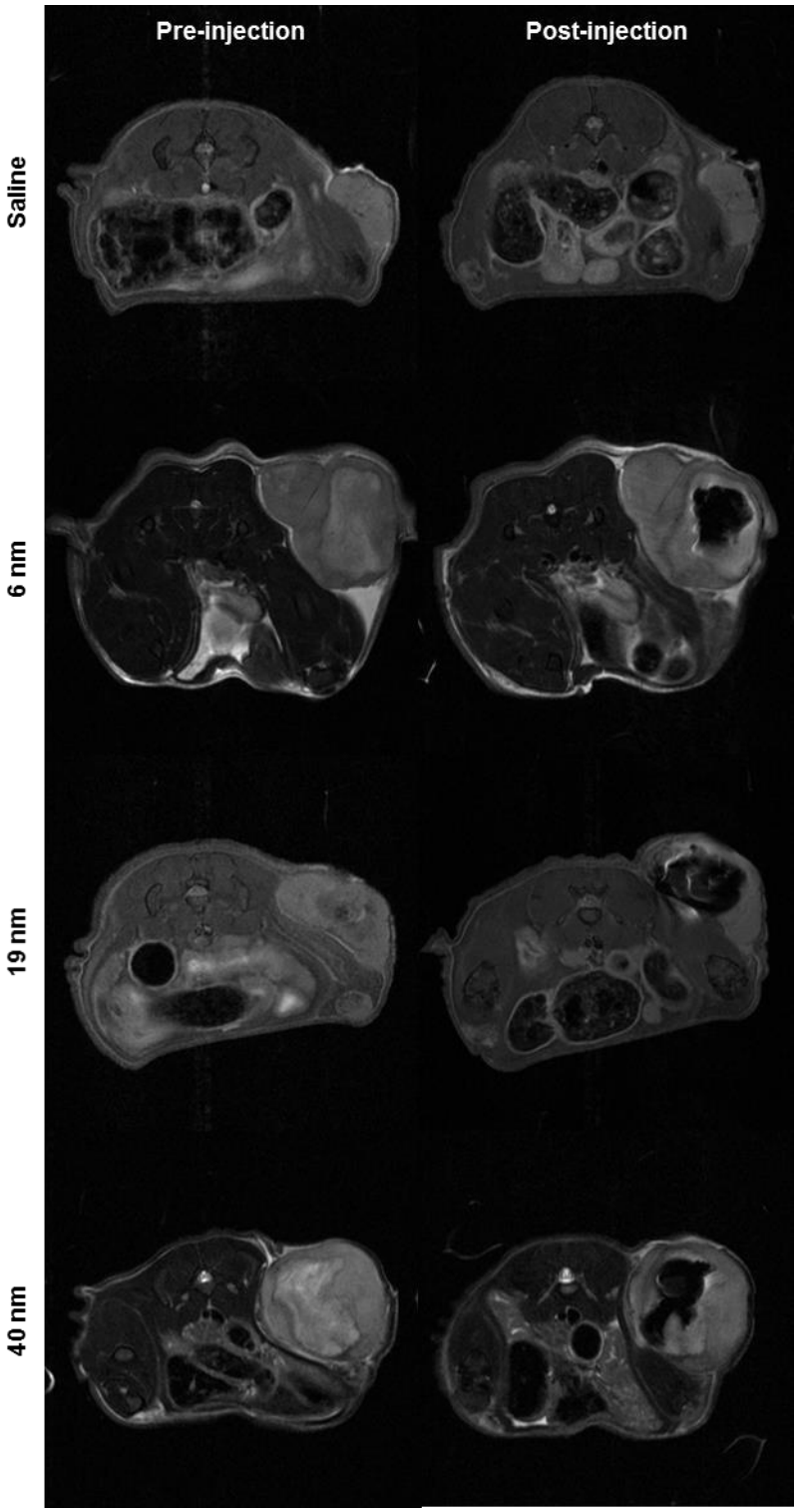

Fig. 5-13 In vivo MRI contrast. T_2 weighted MRI images of mouse tumors before and after 10 μl injection of saline, 6 nm, 19 nm, or 40 nm IONPs at 5 mg/ml Fe.

Following imaging, the mice were exposed to an AMF (13.25 kA/m, 325 kHz) within an inductor coil for one hour (**Fig. 5-14**) which did not change IONP distribution within the tumor (**Fig. 5-15**). During AMF treatment, the temperature within the tumor was measured using the fiber optic temperature probe. The tumors injected with the 6 nm cores did not exhibit an increase in temperature when compared to the saline control, while the 19 nm and 40 nm cores caused a temperature increase of 2.5^{o}C and 10.1^{o}C, respectively (**Fig. 5-16**). The differences in the temperatures attained *in vivo* roughly correspond to the differences in SAR values measured in solution and during heating *in vitro*. Only the 40 nm cores were able to reach the apoptotic temperature threshold of 41^{o}C during the course of the treatment. In comparison with other studies that inject on the order of milligrams of iron or field strengths up to 56 kA/m, we were able to achieve substantial *in vivo* heating using only 50 µg of IONP and an AMF of 13.25 kA/m and 325 kHz.[39, 228, 229]

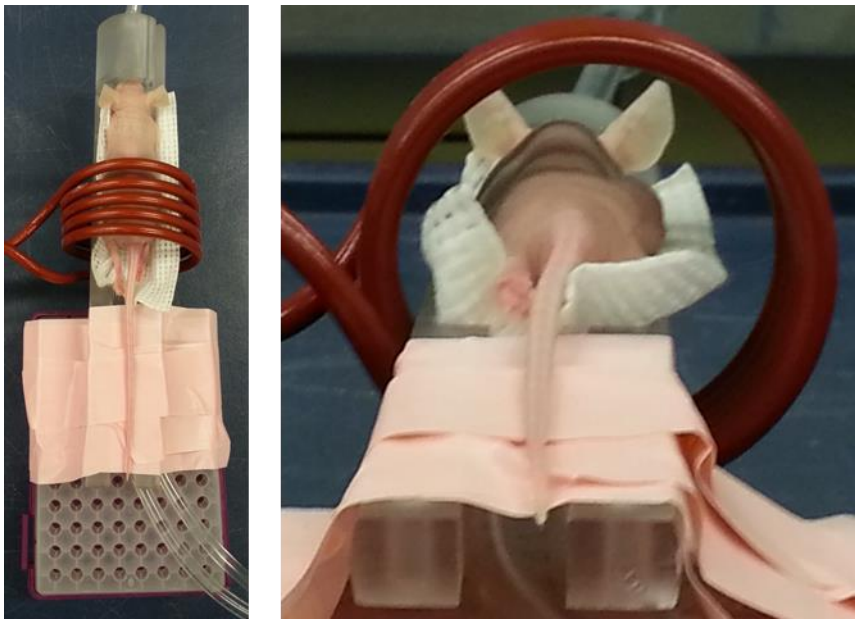

Fig. 5-14 In vivo MFH set up. Tumor-bearing mouse is placed within 5.00 cm inner diameter coil with heating pad underneath to maintain whole body temperature while under 1.5% isoflurane anesthesia.

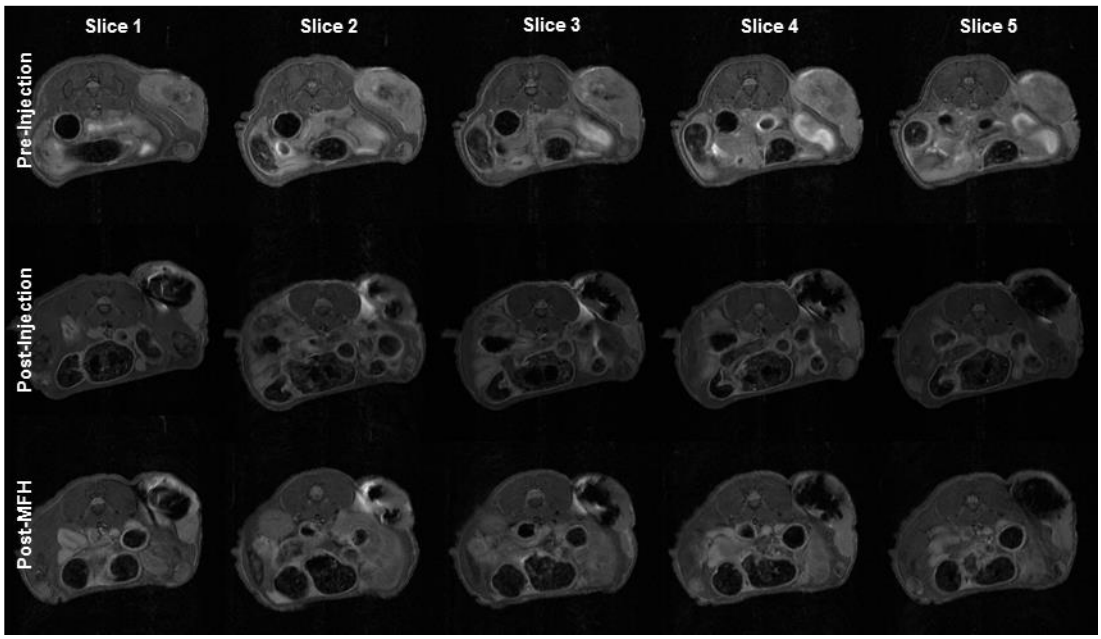

Fig. 5-15 MRI images pre-injection, post-injection, and post-MFH for 19 nm IONP. T_2-weighted MRI images of mouse tumors before and after 10 µl injection of 19 nm at 5 mg/ml Fe, and after 1 hour AMF (13.25 kA/m, 325 kHz) treatment under 1.5%.isoflurane anesthesia.

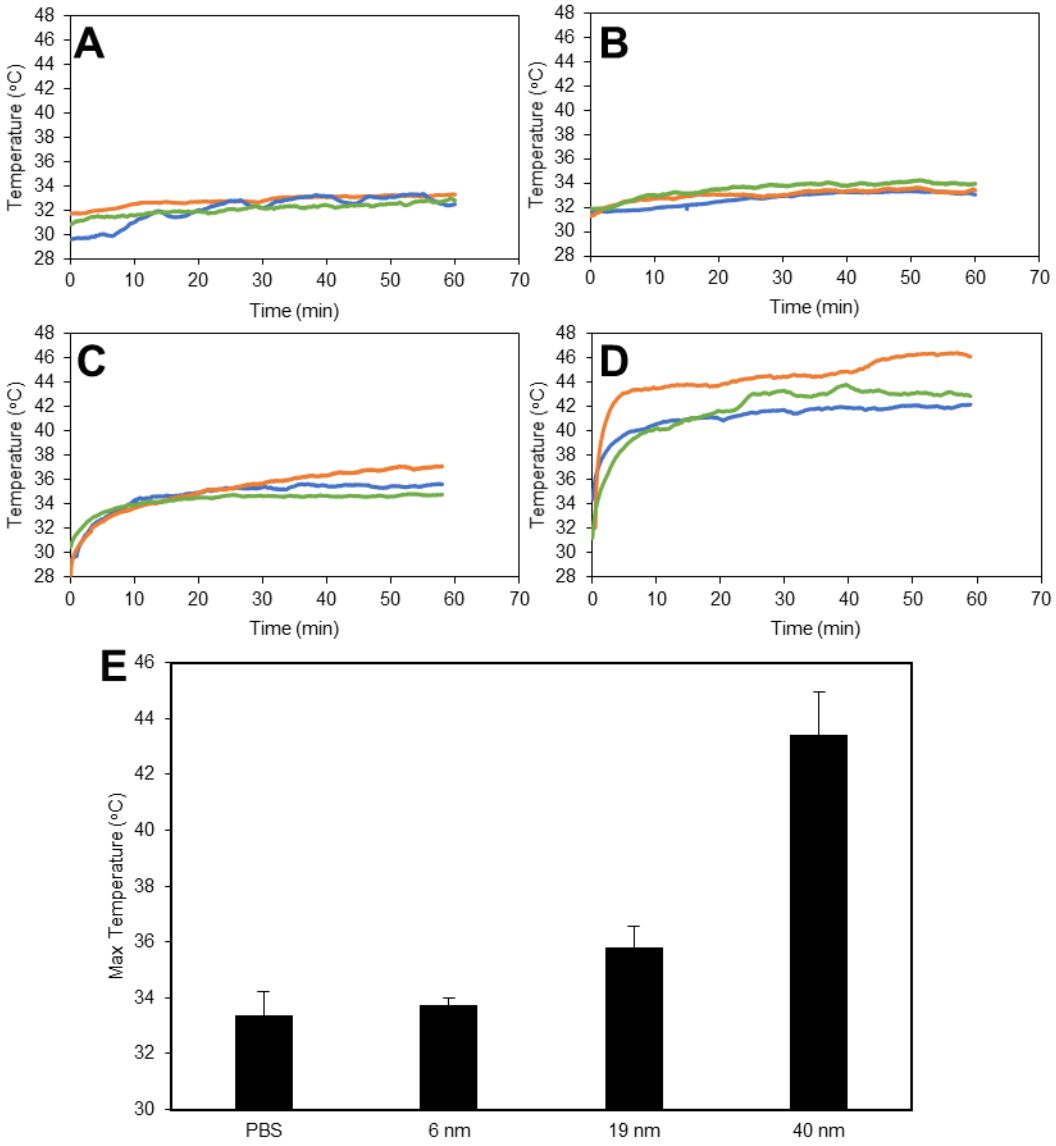

Fig. 5-16 *In vivo* MFH. Temperature profiles of three mouse xenograft tumors injected with 10 µl of (A) saline, (B) 6 nm, (C) 19 nm, or (D) 40 nm SPIOs at 5 mg/ml Fe and exposed to an AMF (13.25 kA/m, 325 kHz) for one hour, and (E) average maximum intratumoral temperature during treatment. Error bars denote standard error.

To observe the physiological effects of the hyperthermia, the tumors were analyzed histologically with a TUNEL apoptosis stain directly following treatment (**Fig. 5-17**). Only the 40 nm IONP-treated tissue exhibits strong TUNEL staining, which is consistent with the temperature measurements since the 40 nm IONPs were the only tested size that reached the apoptotic temperatures during the AMF treatment (**Fig. 5-16**).

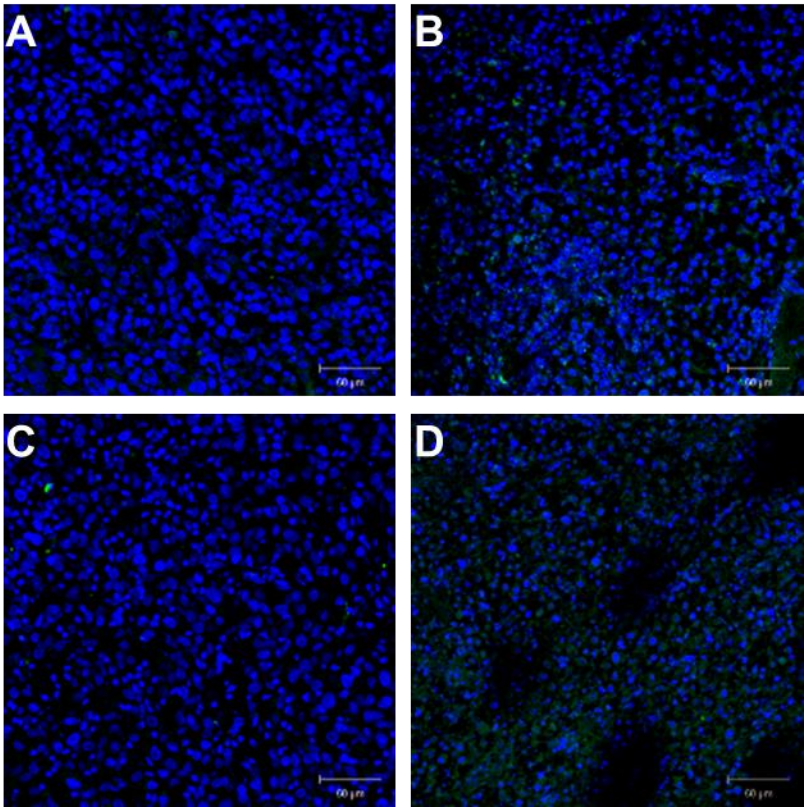

Fig. 5-17 TUNEL apoptosis stain of tumors treated with (A) saline, (B) 6 nm, (C) 19 nm, or (D) 40 nm IONPs at 5 mg/ml Fe and exposed to an AMF of 13.25 kA/m, 325 kHz for one hour. The images displayed in (A-D) are overlays of two channels where cell nuclei are labelled in blue with Hoechst and TUNEL staining is in green.

Combined effect of magnetic fluid hyperthermia and DOX delivery on tumor growth

With the high intratumoral temperatures and evidence of apoptosis attained through MFH with the 40 nm IONPs, we next investigated the efficacy on tumor growth inhibition. This study also opened the opportunity to reexamine IONP-based DOX delivery in an *in vivo* setting. The 40 nm IONPs were able to load DOX at 34% w/w (DOX/Fe) which is consistent with the loading efficiency of the 14 nm IONPs in Chapter 3. Mice bearing ~175 mm^3 tumors were intratumorally injected with 10 µl saline, IONP (5 mg/ml Fe), IONP-DOX (5 mg/ml Fe, 1.7 mg/ml DOX), or free DOX (1.7 mg/ml DOX). The IONP-treated mice were further divided into –/+MFH groups with the +MFH mice undergoing a one hour AMF exposure (13.25 kA/m, 325 kHz) following IONP injection. Free DOX displayed the most growth inhibition most likely due to the high immediate availability of the drug compared to IONP release. Compared to the saline control, all of the treatments excluding free DOX displayed similar growth inhibition through day six (**Fig 5-18**). At day 7, differences between the treatment groups were seen with IONP-based MFH having slightly improved efficacy compared to IONP-DOX, and the combination of the two treatment modalities further reducing tumor growth. It is expected that continuing growth to further time points would expand the differences between treatments as the growth rates became more exponential, but IACUC protocol limits the extent of such tumor growth and at large sizes, some of the tumors started developing ulcers requiring the animal to be sacrificed.

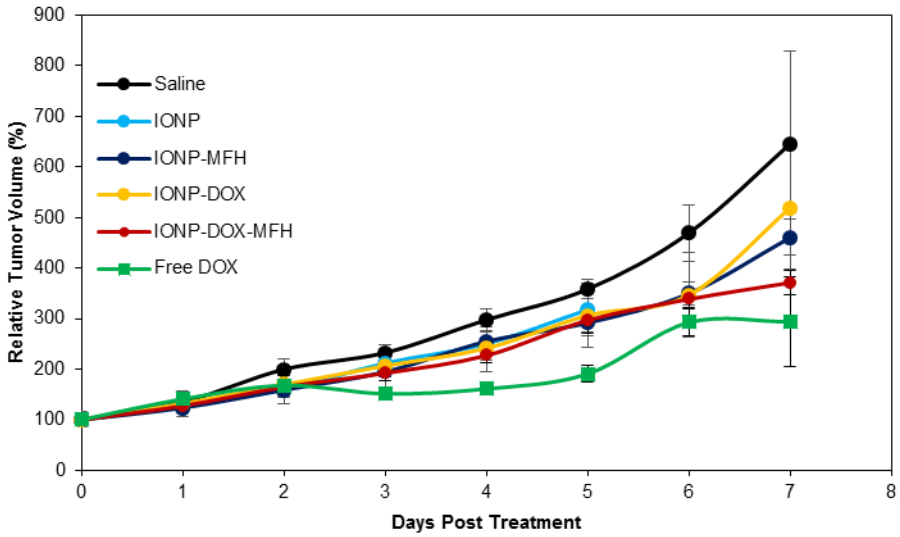

Fig. 5-18 *In vivo* magnetic fluid hyperthermia and DOX treatment tumor growth inhibition. Error bars represent standard error based on 5-7 mice per group.

Discussion

In order for IONPs to realistically impact the fields of cancer hyperthermia therapy and diagnostics, significant efficiency benchmarks must be overcome before they will be viewed as a worthwhile technology for clinical and commercial translation. Due to the body's natural homeostatic temperature regulation methods such as vascular perfusion, power densities up to 20-40 W/kg at the intended location are necessary to reach therapeutically viable temperatures above 42°C.[230, 231] Even for small tumors, a large quantity of heat-mediating IONP would need to be distributed throughout the tumor to ensure total cell death and eliminate the chance of remission. While it is conceivable to increase the heat delivered by raising the magnetic field strength and frequency, there are physiological limits before induction of eddy currents cause non-specific heating in the tissue. Atkinson and Brezovich determined that a field strength-frequency product of 4.85 x 10^8 A $m^{-1}s^{-1}$ was the limit before patients felt discomfort and could no longer tolerate the treatment, though this maximum tolerable dose would vary depending on the size of the

region exposed to the AMF, duration of the treatment, and the equipment producing the AMF.[232, 233] Moreover, the concentration of IONP delivered is limited by cost and safety concerns with the long term biocompatibility of the particles. Therefore, enhancement of MFH must come from optimizing the efficiencies of the particles themselves. As an imaging contrast agent, IONP rely upon MRI which offers high spatial resolution and depth penetration, but sensitivity is far below other modalities such as positron emission tomography (PET) or near-infrared fluorescence (NIRF). While several IONP formulations have been FDA approved and are commercially available for use as MR contrast agents, many have been discontinued due to poor clinical performance. These IONPs were synthesized using coprecipitation methods and characterized by poor control of the size and crystallinity. There is much room for improvement and optimization using modern advanced synthesis techniques that could enhance T_2 relaxivity and bring about the next generation of IONP contrast agents.

There are many nanoparticle properties which contribute to SAR and T_2 relaxivity such as size, shape, crystallinity, and magnetic response to an external field, though core size is the one property that researchers have the most direct control over and is tied to many of the other factors. The MFH numerical simulations in **Fig. 5-1** through **5-4** illustrate the interdependence of core size with polydispersity, magnetic anisotropy, and the external field, but these trends are only relevant in the context of superparamagnetism. As the size increases, IONPs are theorized to transition from superparamagnetic to single then multidomain ferrimagnetism which corresponds with heat generation transitioning from Néelian to Brownian relaxation and finally hysteretic losses. MR contrast is expected to follow similar regime shifts from the MAR to SDR at a certain particle size. Other works have examined core size arrays that encompass solely one magnetic regime, but it is difficult to accurately compare results between these studies due to inconsistent particle compositions and magnetizations stemming from unique synthesis protocols. By using a single thermal decomposition method to synthesize a systematic array of IONP between 6-

40 nm in size, we expected to encounter the multiple transition states for magnetic response, MFH, and MR contrast. The linear increase of both T_2 relaxivity and SAR with increasing core size does not support the existence of regime transitions within the size range tested here (**Figs. 5-8 and 5-10**). According to previous findings on T_2 relaxivity, the theoretical size limit where the MAR transitions to SDR is ~30 nm.[114, 115] This transition marks the size where water diffusion no longer occurs at a faster time scale than the resonance frequency shift caused by the IONPs, and the relaxivity becomes core size-independent. The linear increase in relaxivity up to 40 nm suggests that the cores are all in the MAR and the size limit of this regime is still yet to be reached for our IONPs.

While the size relationship for MR contrast could be justified by assuming all of the particles are within the MAR, the MFH size dependence cannot be neatly described in the existing theoretical frameworks. The room temperature SQUID magnetization curves of the cores are characteristic of superparamagnetism such that hysteretic losses for heat generation would be minimal and thus could not explain the increase in SAR past the optimal size predicted by the numerical simulations (**Figs. 5-6**). Deviations from the linear response theory have been observed by others with respect to the SAR dependences on size, anisotropy, and external field parameters.[203, 213, 225] The linear increase in SAR is inconsistent with iron oxide nanocube studies that investigated cores above 20 nm in size that found a decrease in SAR above this size threshold.[201, 204, 213] Guardia et al. determined that for iron oxide nanocubes, the relationship of edge length to SAR was dependent on the AMF field strength; a shift occurs between 12-24 kA/m causing 35 nm particles to greatly increase in SAR relative to 14, 19, and 24 nm particles.[225] The described phenomenon with nanocubes does not appear to apply to our nanoparticles, as a linear increase in SAR was observed with field strengths of 13.3 and 23.8 kA/m. A reexamination of the assumptions behind the linear response theory and transition to hysteretic losses may be necessary to characterize the SAR results described here.

The importance of optimizing for SAR and T_2 relaxivity was demonstrated through the translation to *in vitro* and *in vivo* environments. For the same concentration of 6, 19, and 40 nm IONPs, local temperatures vary between remaining unchanged, reaching apoptotic levels, or inducing thermal ablation, respectively (**Fig. 5-11**). The range of these temperatures correspond to stark differences in the cellular response to the treatment. Delivery of IONP to the tumor remains challenging even with intratumoral injection due to the poor control over distribution through the tissue. The theranostic utility of the IONP platform aided in identifying the borders of the ferrofluid within the tumor through MRI. Intratumoral temperature homogeneity is necessary for successful therapy and is facilitated by proper distribution of IONP. Unfortunately with the thermal probe available, a spatial profile of the temperature distribution could not be measured.

The 40 nm cores were able to increase the tumor temperature to apoptotic levels by delivering only 50 µg of iron to the tumors, demonstrating the reduction in dose afforded by the high heating efficiency compared to other studies requiring milligrams of IONPs (**Fig. 5-16**).[111, 228, 234-236] The reduced temperatures achieved during tumor MFH compared to the *in vitro* studies could be attributed to thermal energy transfer through the skin and to other tissues through blood flow. Although cell death could be observed histologically after the treatment, the overall inhibition of tumor growth even with combined DOX delivery was underwhelming (**Fig. 5-18**). The subpar efficacy of this preliminary *in vivo* study prompts the use of a multiday treatment regimen similar to the one used in the study by Troyer et al. Higher concentrations of IONPs or increased AMF field strength could also be utilized, but care was taken to prioritize apoptosis over induction of thermal ablation which could harm adjacent healthy tissue. Tuning the delivered thermal dose in conjunction with drug delivery to elicit a controlled apoptotic response within the growing tumor will require a more comprehensive parametric study to be conducted in the future.

Conclusion

Developing IONPs for MRI and/or MFH biomedical applications requires careful consideration of the physicochemical properties of the particles in order to achieve peak efficiencies. Magnetic core size plays a critical role in the optimization process, as there exists strong dependencies for relaxivity and SAR that encompass specific size regimes where the governing mechanisms of these processes shift. In this work, we examined the influence of core size for MRI and MFH in solution, *in vitro*, and *in vivo* using a systematic array of IONPs from 6-40 nm in diameter with a controlled and uniform phospholipid-PEG coating. For both relaxivity and SAR, there was a linear dependence on core size up through 40 nm in size, suggesting the particles are within the size-dependent motion averaging regime for MR contrast, but the heating generation mechanism is unclear. Using an intratumoral injection, nanoparticles with cores of 6, 19, and 40 nm provided a high degree of contrast to clearly delineate the IONP distribution within the tumor. The 40 nm cores displayed the highest recorded T_2 contrast and heat generation, causing cell death *in vitro* and *in vivo* even at low concentrations. Future studies will require further refinement of the synthesis process in order to create larger, monodisperse superparamagnetic core populations to experimentally probe the limits of the MRI and MFH size regimes. This work describes the therapeutic and diagnostic potential of iron oxide nanoparticles above the presumed superparamagnetic limit to reach clinically relevant levels in order to improve cancer treatment.

CHAPTER 6

FUTURE CONSIDERATIONS

In this work, phospholipid-PEG coated iron oxide nanoparticles were developed and optimized in terms of their core size and coating for effective drug delivery, heat generation, and magnetic resonance contrast. The drug loading mechanism utilizes partitioning of poorly soluble molecules into the lipid coating layer of the IONPs to create a drug delivery platform with high loading capacity which does not require chemical conjugation. Combining the drug delivery and hyperthermia potential of these IONPs has enabled an enhanced cancer therapy that could be a novel tool for oncologists looking to use multimodal treatments for their patients. By increasing the core size to 40 nm, the heat generation and MR contrast reached the highest recorded values to date. This work systematically covers a large range of sizes that span the magnetic regimes of magnetic nanoparticles and examines how the trends seen *in vitro* translate to a physiological environment. The observed results suggest that the predicted size cutoffs for these magnetic regimes may need to be reconsidered in the light of the experimental evidence.

The studies in Chapter 3 illustrate how the concurrent delivery of Doxorubicin and heat contributed to an enhanced cell death. The discrepancies between the interaction of chemotherapeutics and hyperthermia amongst other work demonstrate the complexity of this interaction. The timing and sequence of the two treatment modalities has been shown to play a role in the cellular response where a clear difference in efficacy is observed between heat treatment before, during, or after drug exposure.[97, 100, 237, 238] In the context of SPIO-based hyperthermia and drug delivery, the asynchronous timing of each modality is further complicated by the transient release profile of the drug from the nanoparticles. Future studies aiming to maximize the therapeutic response to combination treatment should plan the timing of hyperthermia in relation to the drug release kinetics.

To better understand the interplay between magnetic fluid hyperthermia and chemotherapy, studies could be designed to probe components of the signaling pathway leading to apoptosis. Cleavage of Caspase-3 and PARP1 are well-characterized late-stage events in the mitochondrial pathway of apoptosis that can be identified via western blotting.[239-242] Bcl-2 and Bcl-xL are anti-apoptotic proteins upstream of mitochondrial cytochrome c release, and their suppression is another viable marker for apoptosis.[243-245] By monitoring various stages of the apoptotic pathway, the protective effect of heat shock proteins can be examined. The heat shock proteins, the most prominent being HSP 70, are the cell's inherent defense against heat stress by acting as chaperones to refold denatured proteins and inhibiting multiple stages of the apoptotic signaling cascade.[246, 247] The upregulation of the heat shock proteins following hyperthermia is associated with the development of thermal tolerance to subsequent heat treatments. The anti-apoptotic capacity of the heat shock proteins can also reduce drug efficacy due to the shared apoptotic pathways of hyperthermia and chemotherapy. Minimizing the induction and impact of the heat shock proteins through proper timing of hyperthermia will help prevent resistance to the overall therapy. Another strategy used by Ito et al. involved co-delivery of the HSP 90 inhibitor, geldanamycin, and ferromagnetic particle hyperthermia resulting in a complete tumor regression compared to the individual treatments.[248] Future studies could investigate loading HSP inhibitors onto our IONPs for a similar goal.

There are several areas where the *in vivo* studies in this work could be expanded. The setup and protocol used for the mouse magnetic fluid hyperthermia was an initial proof of concept to characterize the transient temperature profiles using the various core sizes. To design the experiments for maximum therapeutic response, a number a modifications could be employed. The ectopic subcutaneous xenograft tumor model suffices as a first step for testing treatments due to the ease and speed of induction, but it does not properly recapitulate the actual tumor microenvironment of the cancer cells in the native tissue. An orthotopic tumor model where the human cancer cells are transplanted into the same tissue

in the mouse as the cancer cells originated from would be a more realistic model. The tumors would not be amenable to caliper measurement, so in order to measure tumor growth, the cancer cell line used would need to express a fluorescent protein or luciferase to be monitored with an optical imaging system. In the case of glioblastoma, an orthotopic model is especially challenging with respect to transplantation and imaging due to the presence of the skull surrounding the tissue. Magnetic resonance imaging would need to be used to measure tumor size, though the extremely low throughput makes large scale studies difficult.

A larger animal model would also be beneficial for the hyperthermia studies. With intratumoral injections, the tumor needed to reach approximately 750 mm^3 before the syringe could be properly inserted. At that stage of tumor development, the growth rate is very rapid with the tumor reaching the IACUC mandated size endpoint within a week's time. This left a narrow window to perform the treatment and monitor the effects on tumor growth. Working with larger tumors in a rat model would facilitate longer growth studies that could be started at an earlier stage in tumor development. Further, multiday treatment regimens and an intratumoral injection spread across several sites within the tumor could be realized to improve overall treatment efficacy. Multiple hyperthermia treatment would allow for an analysis of the heat generation efficiency over repeated AMF applications, and the therapy would mirror the multiple dosing regimens of conventional chemotherapy and radiotherapy. Spreading the SPIO delivery into multiple smaller injections allows for better spatial control that can be tailored to the dimensions of the tumor, ensuring a more homogeneous heating throughout the tumor.

The *in vivo* MFH temperature measurements in Chapter 5 were limited to a single point within the tumor due to the relative size of the thermal probe to the tumor. A critical factor in cancer treatment is ensuring that the entirety of the tumor tissue receives the necessary treatment dose for cell death. Hyperthermia therapy works on the same principle, so an understanding of the spatial temperature profile within the tumor would improve

thermal dosimetry and could prevent unwanted heating in the surrounding tissue. The MRI IONP distribution information could be used to model the temperature profile with knowledge of the SAR of the particles. Quantitative IONP concentration data is difficult to determine with MRI, and the concentrations used for MFH intratumoral injection are high enough to saturate the MR signal. A rough estimate could be determined based on the volume of distribution and the known amount of SPIO injected. A modeling approach using Pennes bioheat equation similar to the one used by Kappiyoor et al. and Salloum et al. could then map spatial temperature profiles during MFH.[249, 250]

As eluded to previously, longer term *in vivo* studies that focus on biodistribution, metabolic breakdown, and the measurement of the IONP properties over time would aid our understanding of the interactions between IONPs and the body. The long term fate of the IONPs following intratumoral injection is worth investigating as a single nanoparticle injection could facilitate continued hyperthermia treatment, sustained drug release, and MR contrast long after the initial delivery. Clearance out of the tumor and degradation of the nanoparticles are two mechanisms that could hinder long term functionality of the IONPs. Clearance could occur through diffusion into lymphatic vessels or assisted by macrophage uptake. The DSPE-PEG coating stability has not yet been characterized for extended periods of time in a physiological environment, and if compromised, it may not effectively prevent macrophage recognition. It would be interesting to examine how the core size plays a role in IONP clearance since previous work using polymeric nanoparticles found larger particles were phagocytized more efficiently by macrophages.[251]

Metabolism of iron oxide nanoparticles once in the body is still poorly understood. A few studies investigating how IONPs are metabolized by cells in the RES found evidence of the nanoparticles breaking down over the course of three months with a characteristic decrease in their superparamagnetic property.[23, 252] Loss of superparamagnetism and reduction in saturation magnetization would thus hinder long term use as contrast agents or mediators for hyperthermia. It is presumed that the iron is converted to poorly magnetic

species which are incorporated into the proteins ferritin and hemosiderin. In this context, core size and the PEG length would be important factors affecting the rate of SPIO degradation to study. The smaller surface area to volume ratio for larger sized cores would be beneficial to slow the degradation process and maintain superparamagnetism for longer periods of time. Furthermore, a longer PEG length could protect the metallic core from enzymatic degradation as well.

One of the main issues faced in this work and with the current state of nanoparticle development is that only a few percent of systemically delivered nanoparticles localize to the tumor when relying upon the EPR effect. In order for systemic deliver of nanoparticles to be viable for magnetic fluid hyperthermia, IONP accumulation in the tumor needs to be improved. Active targeting through the conjugation of targeting ligands to the surface of the nanoparticle, whether they be antibodies, peptides, or small molecules, allows specific binding of the nanoparticles to a cell type of interest. It is critical to choose the proper target as the receptor needs to be highly expressed on the targeted cell for efficient binding, but under expressed on off-target cells to prevent nonspecific interactions. This issue is most prevalent with cancer therapy as it is difficult to find targets solely unique to the malignant cells which are not expressed by their healthy neighboring cells.[253] Another complication is the inherent heterogeneity such that even for a particular type of cancer, a universally effective target is rare and requires in-depth characterization of the subclass of an individual's cancer.

Conventional targeting has focused on receptors present on the cancer cells themselves, though these studies have been met with modest success as there is limited penetration into the tumor interstitium following extravasation from the vasculature.[254] One possible targeting strategy is the use of ligands specific to tumor vasculature endothelial markers. The angiogenic vessels within the tumor overexpress both $\alpha v\beta 3$ and $\alpha v\beta 5$ integrins which could be targeted without needing penetration into the tumor for binding.[255-257] By not relying upon the initial extravasation due to the EPR effect, early

stage tumors or metastases that have yet to develop the leaky vasculature necessary for the EPR effect could be targeted.

An alternative targeting strategy would be to utilize methods to increase tissue penetration. Drug penetration through the tumor is reliant upon Fick's law and due to the high interstitial pressure, diffusion only occurs to distances of about 40-50 μm, leaving many cells at sublethal drug concentrations.[258, 259] Nanoparticles are much larger in size in comparison to small molecules, further reducing diffusion distances as characterized by the Stokes-Einstein equation. Recent work involving tumor-penetrating peptides such as iRGD can bind to the tumor vasculature through the RGD motif and then be shuttled through tumor tissue along an endocytic bulk transport pathway due to the CendR motif.[260-262] Conjugating this peptide to the IONPs could enhance distribution within the tumor following systemic or intratumoral injection.

The superparamagnetic property of the IONPs can also be applied towards accumulation and penetration into the tumor through either magnetic targeting or magnetic fluid hyperthermia. Magnetic targeting relies upon the response of IONPs within a magnetic field gradient to cause an attractive or repulsive force. The magnitude of the force is governed by:

$$F = (\nabla B^2)\frac{\chi V_c}{2\mu_0},$$

where ∇B is the gradient of the magnetic field, χ is the magnetic susceptibility of the IONP, V_c is the magnetic core volume, and μ_0 is the magnetic permeability of free space.[263] A larger core size will be beneficial for this function as it was for MR contrast and MFH. The magnetic force can be used to move IONPs to the perimeter of the tumor blood vessels to promote extravasation and/or resist the hydrodynamic drag forces from blood flow to enhance retention within the tumor. This approach has seen success in a squamous cell carcinoma rabbit model to deliver the drug mitoxantrone using an intraarterial injection and an electromagnet to generate the magnetic field gradient.[264] Schleich et al.,

combined magnetic targeting with αvβ3 integrin targeting to improve delivery of Paclitaxel to colon carcinomas in mice.[265] Once within the tumor, the magnetic force could be used to drag the IONPs past conventional diffusion limits for a wider intratumoral distribution. Designing the appropriate setup to generate magnetic field gradients for clinical use will be challenging especially for tumors located deep in the body and will require extensive magnetic field modeling.[266, 267]

Hyperthermia has been shown to enhance extravasation of liposomes by increasing the size of the pores in the tumor endothelium.[164] With IONPs capable of generating local heat within the tumor through MFH, a feedforward mechanism could be envisioned where accumulation of IONPs within the tumor could help additional IONPs extravasate into the tumor, increasing the local concentration and thus increasing the local temperature. The timing and temperatures used for hyperthermia-enhanced IONP accumulation would need to be well-controlled as has been seen with liposomes.[268] The increased blood flow associated with inflammation temperatures (up to 42^{o}C) can also enhance extravasation until nanoparticle concentrations able to sustain apoptotic temperatures are reached.

A conscious design choice when developing the IONPs in this work was to avoid using chemical conjugation for drug loading in order to leave open the potential for additional functionalities. The PEG chains on the outer surface of the IONPs can easily incorporate functional groups such as amine, carboxyl, or maleimide for a host of conjugation methods to employ. Previous work in our lab has utilized this conjugation potential to attach antibodies targeting folate and VEGF, chelators for radiolabeling, and the RGD peptide.[64, 65] Radiolabeling offers an accurate quantitative measure to perform biodistribution studies through PET imaging, and targeting ligand conjugation enables active targeting to further enhance specificity for IONP delivery. Drugs not amenable to passive loading into the lipid layer of the SPIO could be conjugated to the surface which also facilitates multi-drug loading and triggered drug release mechanisms. Dilnawaz et al. developed an IONP capable of loading both Paclitaxel and Rapamycin into the glycerol

monooleate coating and conjugated the HER2 antibody for cancer targeting.[85] This type of multidrug loading and active targeting could be applied to our DSPE-PEG coated IONPs.

Conjugation of additional functionalities comes at the price of raising the complexity of the particle, making synthesis more costly, difficult, and time-consuming. Optimization for each of the functionalities can also lead to conflicting priorities such that the final design incorporates many functions, but is subpar at each.[253] Lastly, increased complexity raises the bar for regulatory hurdles that must be overcome to eventually achieve the ultimate goal of clinical translation. The greater number of moieties present on the nanoparticle necessitate further characterization to ensure safety in a regulatory landscape already cautious to the idea nanoparticle therapeutics. These tradeoffs should be weighed early in design as well as during evaluation before each transition step in development. Thus, the design and development of nanoparticles for biomedical applications walks a fine line between achieving greater utility and efficacy against creating an over-engineered particle that loses sight of its original purpose. The tradeoffs of additional functionalities must be weighed against the potential benefits

The iron oxide nanoparticle platform described in this work is unique in relation to other classes of nanoparticles because most of its multifunctionality stems solely from the magnetic metallic core. Magnetic resonance imaging, magnetic fluid hyperthermia, and magnetic guidance all benefit from optimization of similar parameters such as high saturation magnetization, minimal coercivity, high magnetic anisotropy, and large core size. With the exception of very large core size, these properties should not affect biological performance in terms of circulation half-life, biodistribution, extravasation, cell internalization, metabolism, excretion, and overall biocompatibility. We found the 40 nm cores to generate the largest amount of heat and MR contrast, and even with the coating hydrodynamic diameter of 52 nm, the size should not compromise biological performance. The phospholipid-PEG coating that interacts with the environment can be tuned

independent of the core size for the particular functionalities to be utilized. From this work and previous work in the lab, the PEG 2000 length should be optimal for hyperthermia, MRI, and drug delivery.[65] At this point, what remains to be decided is the appropriate surface functionalization, whether it be targeting, tumor penetration, or addition of a secondary imaging modality, that has the most favorable cost/benefit ratio for clinical translation.

REFERENCES

[1] P. Weiss, "La variation du ferromagnétisme avec la température," *Comptes Rendus,* vol. 143, p. 1136, 1906.

[2] E. C. Stoner and E. Wohlfarth, "A mechanism of magnetic hysteresis in heterogeneous alloys," *Philosophical Transactions of the Royal Society of London A: Mathematical, Physical and Engineering Sciences,* vol. 240, pp. 599-642, 1948.

[3] J. Eisenmenger and I. K. Schuller, "Magnetic nanostructures: overcoming thermal fluctuations," *Nature materials,* vol. 2, pp. 437-438, 2003.

[4] L. Néel, "Theory of the magnetic after-effect in ferromagnetics in the form of small particles, with applications to baked clays," *Ann. Geophys.(CNRS),* vol. 5, pp. 99-136, 1949.

[5] W. F. Brown Jr, "Thermal fluctuations of a single-domain particle," *Journal of Applied Physics,* vol. 34, pp. 1319-1320, 1963.

[6] M. Etheridge, N. Manuchehrabadi, R. Franklin, and J. Bischof, "Superparamagnetic iron oxide nanoparticle heating: A basic tutorial," *Nanoparticle Heat Transfer and Fluid Flow,* pp. 97-121, 2012.

[7] P. Chandrasekharan, D. Maity, C. X. Yong, K. H. Chuang, J. Ding, and S. S. Feng, "Vitamin E (D-alpha-tocopheryl-co-poly(ethylene glycol) 1000 succinate) micelles-superparamagnetic iron oxide nanoparticles for enhanced thermotherapy and MRI," *Biomaterials,* vol. 32, pp. 5663-72, Aug 2011.

[8] V. S. Kalambur, B. Han, B. E. Hammer, T. W. Shield, and J. C. Bischof, "In vitro characterization of movement, heating and visualization of magnetic nanoparticles for biomedical applications," *Nanotechnology,* vol. 16, pp. 1221-1233, 2005.

[9] N. Landazuri, S. Tong, J. Suo, G. Joseph, D. Weiss, D. J. Sutcliffe, *et al.*, "Magnetic targeting of human mesenchymal stem cells with internalized superparamagnetic iron oxide nanoparticles," *Small,* vol. 9, pp. 4017-26, Dec 9 2013.

[10] G. Y. Lee, W. P. Qian, L. Wang, Y. A. Wang, C. A. Staley, M. Satpathy, *et al.*, "Theranostic nanoparticles with controlled release of gemcitabine for targeted therapy and MRI of pancreatic cancer," *ACS Nano,* vol. 7, pp. 2078-2089, 2013.

[11] T. R. Sathe, A. Agrawal, and S. Nie, "Mesoporous silica beads embedded with semiconductor quantum dots and iron oxide nanocrystals dual-function microcarriers for optical encoding and magnetic separation," *Analytical Chemistry,* vol. 78, pp. 5627-5632, 2006.

[12] C. Sun, K. Du, C. Fang, N. Bhattarai, O. Veiseh, F. M. Kievit, *et al.*, "PEG-Mediated Synthesis of Highly Dispersive Multifunctional Superparamagnetic Nanoparticles: Their Physicochemical Properties and Function In Vivo," *ACS Nano,* vol. 4, pp. 2402-2410, 2010.

[13] C. T. Yavuz, J. T. Mayo, W. W. Yu, A. Prakash, J. C. Falkner, S. Yean, *et al.*, "Low-field magnetic separation of monodisperse Fe3O4 nanocrystals," *Science,* vol. 314, pp. 964-7, Nov 10 2006.
[14] Y. Ling, K. Wei, Y. Luo, X. Gao, and S. Zhong, "Dual docetaxel/superparamagnetic iron oxide loaded nanoparticles for both targeting magnetic resonance imaging and cancer therapy," *Biomaterials,* vol. 32, pp. 7139-7150, 2011.
[15] X. Yang, J. J. Grailer, I. J. Rowland, A. Javadi, S. A. Hurley, D. A. Steeber, *et al.*, "Multifunctional SPIO/DOX-loaded wormlike polymer vesicles for cancer therapy and MR imaging," *Biomaterials,* vol. 31, pp. 9065-73, Dec 2010.
[16] X. Yang, H. Hong, J. J. Grailer, I. J. Rowland, A. Javadi, S. A. Hurley, *et al.*, "cRGD-functionalized, DOX-conjugated, and 64 Cu-labeled superparamagnetic iron oxide nanoparticles for targeted anticancer drug delivery and PET/MR imaging," *Biomaterials,* vol. 32, pp. 4151-4160, 2011.
[17] H. J. Broxterman, J. Lankelma, and K. Hoekman, "Resistance to cytotoxic and anti-angiogenic anticancer agents: similarities and differences," *Drug resistance updates,* vol. 6, pp. 111-127, 2003.
[18] S. Goodwin, C. Peterson, C. Hoh, and C. Bittner, "Targeting and retention of magnetic targeted carriers (MTCs) enhancing intra-arterial chemotherapy," *Journal of Magnetism and Magnetic Materials,* vol. 194, pp. 132-139, 1999.
[19] B. Chertok, B. A. Moffat, A. E. David, F. Yu, C. Bergemann, B. D. Ross, *et al.*, "Iron oxide nanoparticles as a drug delivery vehicle for MRI monitored magnetic targeting of brain tumors," *Biomaterials,* vol. 29, pp. 487-496, 2008.
[20] C. Alexiou, R. Jurgons, R. J. Schmid, C. Bergemann, J. Henke, W. Erhardt, *et al.*, "Magnetic drug targeting--biodistribution of the magnetic carrier and the chemotherapeutic agent mitoxantrone after locoregional cancer treatment," *J Drug Target,* vol. 11, pp. 139-49, Apr 2003.
[21] L. Gu, R. H. Fang, M. J. Sailor, and J.-H. Park, "In vivo clearance and toxicity of monodisperse iron oxide nanocrystals," *ACS nano,* vol. 6, pp. 4947-4954, 2012.
[22] R. a. Weissleder, D. Stark, B. Engelstad, B. Bacon, C. Compton, D. White, *et al.*, "Superparamagnetic iron oxide: pharmacokinetics and toxicity," *American Journal of Roentgenology,* vol. 152, pp. 167-173, 1989.
[23] K. Briley-Saebo, A. Bjørnerud, D. Grant, H. Ahlstrom, T. Berg, and G. M. Kindberg, "Hepatic cellular distribution and degradation of iron oxide nanoparticles following single intravenous injection in rats: implications for magnetic resonance imaging," *Cell and tissue research,* vol. 316, pp. 315-323, 2004.
[24] B. S. Spinowitz, A. T. Kausz, J. Baptista, S. D. Noble, R. Sothinathan, M. V. Bernardo, *et al.*, "Ferumoxytol for treating iron deficiency anemia in CKD," *J Am Soc Nephrol,* vol. 19, pp. 1599-605, Aug 2008.
[25] S. Qu, H. Yang, D. Ren, S. Kan, G. Zou, D. Li, *et al.*, "Magnetite nanoparticles prepared by precipitation from partially reduced ferric chloride aqueous solutions," *Journal of colloid and interface science,* vol. 215, pp. 190-192, 1999.
[26] Y. S. Kang, S. Risbud, J. F. Rabolt, and P. Stroeve, "Synthesis and characterization of nanometer-size Fe3O4 and γ-Fe2O3 particles," *Chemistry of Materials,* vol. 8, pp. 2209-2211, 1996.

[27] R. S. Molday and D. Mackenzie, "Immunospecific ferromagnetic iron-dextran reagents for the labeling and magnetic separation of cells," *Journal of immunological methods,* vol. 52, pp. 353-367, 1982.
[28] R. Weissleder, G. Elizondo, J. Wittenberg, C. Rabito, H. Bengele, and L. Josephson, "Ultrasmall superparamagnetic iron oxide: characterization of a new class of contrast agents for MR imaging," *Radiology,* vol. 175, pp. 489-493, 1990.
[29] M. Pileni, "Reverse micelles as microreactors," *The Journal of physical chemistry,* vol. 97, pp. 6961-6973, 1993.
[30] Y. Deng, L. Wang, W. Yang, S. Fu, and A. Elaıssari, "Preparation of magnetic polymeric particles via inverse microemulsion polymerization process," *Journal of magnetism and magnetic materials,* vol. 257, pp. 69-78, 2003.
[31] V. Pillai, P. Kumar, M. Hou, P. Ayyub, and D. Shah, "Preparation of nanoparticles of silver halides, superconductors and magnetic materials using water-in-oil microemulsions as nano-reactors," *Advances in Colloid and Interface Science,* vol. 55, pp. 241-269, 1995.
[32] C. T. Seip, E. E. Carpenter, C. J. Connor, V. T. John, and S. Li, "Magnetic properties of a series of ferrite nanoparticles synthesized in reverse micelles," *Magnetics, IEEE Transactions on,* vol. 34, pp. 1111-1113, 1998.
[33] X. Wang, J. Zhuang, Q. Peng, and Y. Li, "A general strategy for nanocrystal synthesis," *Nature,* vol. 437, pp. 121-124, 2005.
[34] K. S. Suslick, M. Fang, and T. Hyeon, "Sonochemical synthesis of iron colloids," *Journal of the American Chemical Society,* vol. 118, pp. 11960-11961, 1996.
[35] T. G. Carreño, A. Mifsud, C. Serna, and J. Palacios, "Preparation of homogeneous ZnCo mixed oxides by spray pyrolysis," *Materials chemistry and physics,* vol. 27, pp. 287-296, 1991.
[36] S. Veintemillas-Verdaguer, M. Morales, and C. Serna, "Effect of the oxidation conditions on the maghemites produced by laser pyrolysis," *Applied organometallic chemistry,* vol. 15, pp. 365-372, 2001.
[37] T. Tillotson, A. Gash, R. Simpson, L. Hrubesh, J. Satcher, and J. Poco, "Nanostructured energetic materials using sol–gel methodologies," *Journal of Non-Crystalline Solids,* vol. 285, pp. 338-345, 2001.
[38] Y. Okamura, H. Takeyama, and T. Matsunaga, "A Magnetosome-specific GTPase from the Magnetic BacteriumMagnetospirillum magneticum AMB-1," *Journal of Biological Chemistry,* vol. 276, pp. 48183-48188, 2001.
[39] E. Alphandery, S. Faure, O. Seksek, F. o. Guyot, and I. Chebbi, "Chains of magnetosomes extracted from AMB-1 magnetotactic bacteria for application in alternative magnetic field cancer therapy," *ACS nano,* vol. 5, pp. 6279-6296, 2011.
[40] C. Murray, D. J. Norris, and M. G. Bawendi, "Synthesis and characterization of nearly monodisperse CdE (E= sulfur, selenium, tellurium) semiconductor nanocrystallites," *Journal of the American Chemical Society,* vol. 115, pp. 8706-8715, 1993.
[41] S. Sun and H. Zeng, "Size-controlled synthesis of magnetite nanoparticles," *Journal of the American Chemical Society,* vol. 124, pp. 8204-8205, 2002.
[42] T. Hyeon, S. S. Lee, J. Park, Y. Chung, and H. B. Na, "Synthesis of highly crystalline and monodisperse maghemite nanocrystallites without a size-selection

process," *Journal of the American Chemical Society,* vol. 123, pp. 12798-12801, 2001.
[43] T.-D. Nguyen and T.-O. Do, *Size-and shape-controlled synthesis of monodisperse metal oxide and mixed oxide nanocrystals*: INTECH Open Access Publisher, 2011.
[44] J. Park, K. An, Y. Hwang, J. G. Park, H. J. Noh, J. Y. Kim, *et al.*, "Ultra-large-scale syntheses of monodisperse nanocrystals," *Nat Mater,* vol. 3, pp. 891-5, Dec 2004.
[45] J. Park, E. Lee, N. M. Hwang, M. Kang, S. C. Kim, Y. Hwang, *et al.*, "One-nanometer-scale size-controlled synthesis of monodisperse magnetic iron oxide nanoparticles," *Angew Chem Int Ed Engl,* vol. 44, pp. 2873-7, May 6 2005.
[46] W. W. Yu, J. C. Falkner, C. T. Yavuz, and V. L. Colvin, "Synthesis of monodisperse iron oxide nanocrystals by thermal decomposition of iron carboxylate salts," *Chem Commun (Camb),* pp. 2306-7, Oct 21 2004.
[47] J. Cheon, N.-J. Kang, S.-M. Lee, J.-H. Lee, J.-H. Yoon, and S. J. Oh, "Shape evolution of single-crystalline iron oxide nanocrystals," *Journal of the American Chemical Society,* vol. 126, pp. 1950-1951, 2004.
[48] Y. Yin and A. P. Alivisatos, "Colloidal nanocrystal synthesis and the organic-inorganic interface," *Nature,* vol. 437, pp. 664-70, Sep 29 2005.
[49] U. I. Tromsdorf, N. C. Bigall, M. G. Kaul, O. T. Bruns, M. S. Nikolic, B. Mollwitz, *et al.*, "Size and surface effects on the MRI relaxivity of manganese ferrite nanoparticle contrast agents," *Nano letters,* vol. 7, pp. 2422-2427, 2007.
[50] S. Sun, H. Zeng, D. B. Robinson, S. Raoux, P. M. Rice, S. X. Wang, *et al.*, "Monodisperse MFe2O4 (M= Fe, Co, Mn) nanoparticles," *Journal of the American Chemical Society,* vol. 126, pp. 273-279, 2004.
[51] J. Xie, S. Peng, N. Brower, N. Pourmand, S. X. Wang, and S. Sun, "One-pot synthesis of monodisperse iron oxide nanoparticles for potential biomedical applications," *Pure and Applied Chemistry,* vol. 78, 2006.
[52] A. P. Khandhar, R. M. Ferguson, J. A. Simon, and K. M. Krishnan, "Tailored magnetic nanoparticles for optimizing magnetic fluid hyperthermia," *J Biomed Mater Res A,* vol. 100, pp. 728-37, Mar 2012.
[53] M. F. Kircher, U. Mahmood, R. S. King, R. Weissleder, and L. Josephson, "A multimodal nanoparticle for preoperative magnetic resonance imaging and intraoperative optical brain tumor delineation," *Cancer research,* vol. 63, pp. 8122-8125, 2003.
[54] A. Koch, F. Reynolds, M. Kircher, H. Merkle, R. Weissleder, and L. Josephson, "Uptake and metabolism of a dual fluorochrome Tat-nanoparticle in HeLa cells," *Bioconjugate chemistry,* vol. 14, pp. 1115-1121, 2003.
[55] S. J. DeNardo, G. L. DeNardo, L. A. Miers, A. Natarajan, A. R. Foreman, C. Gruettner, *et al.*, "Development of tumor targeting bioprobes ((111)In-chimeric L6 monoclonal antibody nanoparticles) for alternating magnetic field cancer therapy," *Clin Cancer Res,* vol. 11, pp. 7087s-7092s, Oct 1 2005.
[56] W. Y. William, E. Chang, C. M. Sayes, R. Drezek, and V. L. Colvin, "Aqueous dispersion of monodisperse magnetic iron oxide nanocrystals through phase transfer," *Nanotechnology,* vol. 17, p. 4483, 2006.

[57] T. Pellegrino, L. Manna, S. Kudera, T. Liedl, D. Koktysh, A. L. Rogach, *et al.*, "Hydrophobic nanocrystals coated with an amphiphilic polymer shell: a general route to water soluble nanocrystals," *Nano letters,* vol. 4, pp. 703-707, 2004.
[58] A. L. Klibanov, K. Maruyama, V. P. Torchilin, and L. Huang, "Amphipathic polyethyleneglycols effectively prolong the circulation time of liposomes," *FEBS letters,* vol. 268, pp. 235-237, 1990.
[59] Z. G. Gao, A. N. Lukyanov, A. Singhal, and V. P. Torchilin, "Diacyllipid-polymer micelles as nanocarriers for poorly soluble anticancer drugs," *Nano Letters,* vol. 2, pp. 979-982, Sep 2002.
[60] A. Gabizon and D. Papahadjopoulos, "Liposome formulations with prolonged circulation time in blood and enhanced uptake by tumors," *Proceedings of the National Academy of Sciences,* vol. 85, pp. 6949-6953, 1988.
[61] B. Dubertret, P. Skourides, D. J. Norris, V. Noireaux, A. H. Brivanlou, and A. Libchaber, "In vivo imaging of quantum dots encapsulated in phospholipid micelles," *Science,* vol. 298, pp. 1759-62, Nov 29 2002.
[62] L. E. LaConte, N. Nitin, O. Zurkiya, D. Caruntu, C. J. O'Connor, X. Hu, *et al.*, "Coating thickness of magnetic iron oxide nanoparticles affects R2 relaxivity," *J Magn Reson Imaging,* vol. 26, pp. 1634-41, Dec 2007.
[63] C. Glaus, R. Rossin, M. J. Welch, and G. Bao, "In vivo evaluation of 64Cu-labeled magnetic nanoparticles as a dual-modality PET/MR imaging agent," *Bioconjugate chemistry,* vol. 21, pp. 715-722, 2010.
[64] S. Tong, S. Hou, B. Ren, Z. Zheng, and G. Bao, "Self-assembly of phospholipid-PEG coating on nanoparticles through dual solvent exchange," *Nano Lett,* vol. 11, pp. 3720-6, Sep 14 2011.
[65] S. Tong, S. Hou, Z. Zheng, J. Zhou, and G. Bao, "Coating optimization of superparamagnetic iron oxide nanoparticles for high T2 relaxivity," *Nano Lett,* vol. 10, pp. 4607-13, Nov 10 2010.
[66] C. A. Lipinski, "Poor aqueous solubility-an industry wide problem in ADME screening," *American Pharmaceutical Review,* vol. 5, pp. 82-85, 2002.
[67] C. A. Lipinski, "Lipinski Drug-like properties and the causes of poor solubility and poor permeability," *Journal of Pharmacological and Toxicological Methods,* vol. 44, pp. 235-249, 2000.
[68] T. M. Allen and P. R. Cullis, "Drug delivery systems: entering the mainstream," *Science,* vol. 303, pp. 1818-22, Mar 19 2004.
[69] M. E. Davis, Z. G. Chen, and D. M. Shin, "Nanoparticle therapeutics: an emerging treatment modality for cancer," *Nat Rev Drug Discov,* vol. 7, pp. 771-82, Sep 2008.
[70] Y. Matsumura and H. Maeda, "A New Concept for Macromolecular Therapeutics in Cancer Chemotherapy : Mechanism of Tumoritropic Accumulation of Proteins and the Antitumor Agent Smancs A New Concept for Macromolecular Therapeutics in Cancer Chemotherapy : Mechanism of Tumoritropic Accum," *Cancer Research,* vol. 46, pp. 6387-6392, 1986.
[71] M. M. Gottesman, T. Fojo, and S. E. Bates, "Multidrug resistance in cancer: role of ATP-dependent transporters," *Nat Rev Cancer,* vol. 2, pp. 48-58, Jan 2002.

[72] F. M. Kievit, F. Y. Wang, C. Fang, H. Mok, K. Wang, J. R. Silber, *et al.*, "Doxorubicin loaded iron oxide nanoparticles overcome multidrug resistance in cancer in vitro," *J Control Release,* vol. 152, pp. 76-83, May 30 2011.
[73] A. N. Gordon, J. T. Fleagle, D. Guthrie, D. E. Parkin, M. E. Gore, and A. J. Lacave, "Recurrent epithelial ovarian carcinoma: a randomized phase III study of pegylated liposomal doxorubicin versus topotecan," *Journal of clinical oncology,* vol. 19, pp. 3312-3322, 2001.
[74] R. E. Eliaz, S. Nir, C. Marty, and F. C. Szoka, "Determination and modeling of kinetics of cancer cell killing by doxorubicin and doxorubicin encapsulated in targeted liposomes," *Cancer research,* vol. 64, pp. 711-718, 2004.
[75] M. E. O'Brien, N. Wigler, M. Inbar, R. Rosso, E. Grischke, A. Santoro, *et al.*, "Reduced cardiotoxicity and comparable efficacy in a phase III trial of pegylated liposomal doxorubicin HCl (CAELYX/Doxil) versus conventional doxorubicin for first-line treatment of metastatic breast cancer," *Ann Oncol,* vol. 15, pp. 440-9, Mar 2004.
[76] A. Gabizon, H. Shmeeda, and Y. Barenholz, "Pharmacokinetics of pegylated liposomal Doxorubicin: review of animal and human studies," *Clin Pharmacokinet,* vol. 42, pp. 419-36, 2003.
[77] A. Rahman, D. Carmichael, M. Harris, and J. K. Roh, "Comparative pharmacokinetics of free doxorubicin and doxorubicin entrapped in cardiolipin liposomes," *Cancer Res,* vol. 46, pp. 2295-9, May 1986.
[78] V. P. Torchilin, "Recent advances with liposomes as pharmaceutical carriers," *Nat Rev Drug Discov,* vol. 4, pp. 145-60, Feb 2005.
[79] F. M. Kievit, Z. R. Stephen, O. Veiseh, H. Arami, T. Wang, V. P. Lai, *et al.*, "Targeting of primary breast cancers and metastases in a transgenic mouse model using rationally designed multifunctional SPIONs," *ACS nano,* vol. 6, pp. 2591-2601, 2012.
[80] K. Kaaki, K. Herve-Aubert, M. Chiper, A. Shkilnyy, M. Souce, R. Benoit, *et al.*, "Magnetic nanocarriers of doxorubicin coated with poly(ethylene glycol) and folic acid: relation between coating structure, surface properties, colloidal stability, and cancer cell targeting," *Langmuir,* vol. 28, pp. 1496-505, Jan 17 2012.
[81] J. L. Arias, M. Ruiz, V. Gallardo, and A. V. Delgado, "Tegafur loading and release properties of magnetite/poly(alkylcyanoacrylate) (core/shell) nanoparticles," *J Control Release,* vol. 125, pp. 50-8, Jan 4 2008.
[82] C. A. Lipinski, "Drug-like properties and the causes of poor solubility and poor permeability," *Journal of pharmacological and toxicological methods,* vol. 44, pp. 235-249, 2000.
[83] T. K. Jain, M. K. Reddy, M. A. Morales, D. L. Leslie-Pelecky, and V. Labhasetwar, "Biodistribution, clearance, and biocompatibility of iron oxide magnetic nanoparticles in rats," *Molecular pharmaceutics,* vol. 5, pp. 316-327, 2008.
[84] T. K. Jain, M. A. Morales, S. K. Sahoo, D. L. Leslie-Pelecky, and V. Labhasetwar, "Iron oxide nanoparticles for sustained delivery of anticancer agents," *Molecular Pharmaceutics,* vol. 2, pp. 194-205, 2005.

[85] F. Dilnawaz, A. Singh, C. Mohanty, and S. K. Sahoo, "Dual drug loaded superparamagnetic iron oxide nanoparticles for targeted cancer therapy," *Biomaterials,* vol. 31, pp. 3694-706, May 2010.
[86] M. M. Yallapu, S. P. Foy, T. K. Jain, and V. Labhasetwar, "PEG-functionalized magnetic nanoparticles for drug delivery and magnetic resonance imaging applications," *Pharm Res,* vol. 27, pp. 2283-95, Nov 2010.
[87] T. K. Jain, S. P. Foy, B. Erokwu, S. Dimitrijevic, C. A. Flask, and V. Labhasetwar, "Magnetic resonance imaging of multifunctional pluronic stabilized iron-oxide nanoparticles in tumor-bearing mice," *Biomaterials,* vol. 30, pp. 6748-56, Dec 2009.
[88] Y. Sakaguchi, L. C. Stephens, M. Makino, T. Kaneko, F. R. Strebel, L. L. Danhauser, *et al.*, "Apoptosis in tumors and normal tissues induced by whole body hyperthermia in rats," *Cancer Res,* vol. 55, pp. 5459-64, Nov 15 1995.
[89] T. Komata, T. Kanzawa, T. Nashimoto, H. Aoki, S. Endo, M. Nameta, *et al.*, "Mild heat shock induces autophagic growth arrest, but not apoptosis in U251-MG and U87-MG human malignant glioma cells," *J Neurooncol,* vol. 68, pp. 101-11, Jun 2004.
[90] E. Vorotnikova, R. Ivkov, A. Foreman, M. Tries, and S. J. Braunhut, "The magnitude and time-dependence of the apoptotic response of normal and malignant cells subjected to ionizing radiation versus hyperthermia," *Int J Radiat Biol,* vol. 82, pp. 549-59, Aug 2006.
[91] B. V. Harmon, Y. S. Takano, C. M. Winterford, and G. C. Gobe, "The role of apoptosis in the response of cells and tumours to mild hyperthermia," *Int J Radiat Biol,* vol. 59, pp. 489-501, Feb 1991.
[92] K. S. Sellins and J. J. Cohen, "Hyperthermia induces apoptosis in thymocytes," *Radiation Research,* vol. 126, pp. 88-95, 1991.
[93] J. L. Roti Roti, H. H. Kampinga, R. S. Malyapa, W. D. Wright, R. P. vanderWaal, and M. Xu, "Nuclear matrix as a target for hyperthmic killing of cancer cells," *Cell Stress & Chaperones,* vol. 3, pp. 245-255, 1998.
[94] C. W. Song, J. G. Rhee, and S. H. Levitt, "Blood flow in normal tissues and tumors during hyperthermia," *Journal of the National Cancer Institute,* vol. 64, pp. 119-124, 1980.
[95] C. W. Song, M. S. Kang, J. G. Rhee, and S. H. Levitt, "The effect of hyperthermia on vascular function, pH, and cell survival," *Radiology,* vol. 137, pp. 795-803, 1980.
[96] C. W. Song, "Effect of local hyperthermia on blood flow and microenvironment: a review," *Cancer Research,* vol. 44, pp. 4721s-4730s, 1984.
[97] B. Hildebrandt, P. Wust, O. Ahlers, A. Dieing, G. Sreenivasa, T. Kerner, *et al.*, "The cellular and molecular basis of hyperthermia," *Critical Reviews in Oncology Hematology,* vol. 43, pp. 33-56, 2002.
[98] P. Wust, B. Hildebrandt, G. Sreenivasa, B. Rau, J. Gellermann, H. Riess, *et al.*, "Hyperthermia in combined treatment of cancer," *The Lancet Oncology,* vol. 3, pp. 487-497, 2002.
[99] P. Wust, H. Stahl, K. Dieckmann, S. Scheller, J. Loffel, H. Riess, *et al.*, "Local hyperthermia of N2/N3 cervical lymph node metastases: correlation of

technical/thermal parameters and response," *Int. J. Radiation Oncology Biol. Phys.*, vol. 34, pp. 635-646, 1996.
[100] J. M. C. Bull, "An update on the anticancer effects of a combination of chemotherapy and hyperthermia," *Cancer Research*, vol. 44, pp. 4853s-4856s, 1984.
[101] J. Marmor, F. Hilerio, and G. Hahn, "Tumor eradication and cell survival after localized hyperthermia induced by ultrasound," *Cancer Research*, vol. 39, pp. 2166-2171, 1979.
[102] H. Kawai, Y. Minamiya, M. Kitamura, I. Matsuzaki, M. Hashimoto, H. Suzuki, *et al.*, "Direct measurement of doxorubicin concentration in the intact, living single cancer cell during hyperthermia," *Cancer Cell*, vol. 79, pp. 214-219, 1997.
[103] G. Hahn, J. Braun, and I. Har-Kedar, "Thermochemotherapy: Synergism Between Hyperthermia (42-43) and Adriamycin (or Bleomycin) in Mammalian Cell Inactivation," *Proceedings of the National Academy of Sciences*, vol. 72, pp. 937-940, 1975.
[104] M. I. Shliomis, A. F. Pshenichnikov, K. I. Morozov, and I. Y. Shurubor, "Magnetic Properties of Ferrocolloids," *Journal of magnetism and magnetic materials*, vol. 85, pp. 40-46, 1990.
[105] M. Hanson, "The frequency dependence of the complex susceptibility of magnetic liquids," *Journal of magnetism and magnetic materials*, vol. 96, pp. 105-113 1991.
[106] R. E. Rosensweig, "Heating magnetic fluid with alternating magnetic field," *Journal of magnetism and magnetic materials*, vol. 252, pp. 370-374, 2002.
[107] L. Lartigue, C. Innocenti, T. Kalaivani, A. Awwad, M. Sanchez Duque Mdel, Y. Guari, *et al.*, "Water-dispersible sugar-coated iron oxide nanoparticles. An evaluation of their relaxometric and magnetic hyperthermia properties," *J Am Chem Soc*, vol. 133, pp. 10459-72, Jul 13 2011.
[108] L. C. Kennedy, L. R. Bickford, N. A. Lewinski, A. J. Coughlin, Y. Hu, E. S. Day, *et al.*, "A new era for cancer treatment: gold-nanoparticle-mediated thermal therapies," *Small*, vol. 7, pp. 169-83, Jan 17 2011.
[109] M. Domenech, I. Marrero-Berrios, M. Torres-Lugo, and C. Rinaldi, "Lysosomal membrane permeabilization by targeted magnetic nanoparticles in alternating magnetic fields," *ACS nano*, vol. 7, pp. 5091-5101, 2013.
[110] R. Gilchrist, R. Medal, W. D. Shorey, R. C. Hanselman, J. C. Parrott, and C. B. Taylor, "Selective inductive heating of lymph nodes," *Annals of surgery*, vol. 146, p. 596, 1957.
[111] M. Sato, T. Yamashita, M. Ohkura, Y. Osai, A. Sato, T. Takada, *et al.*, "N-propionyl-cysteaminylphenol-magnetite conjugate (NPrCAP/M) is a nanoparticle for the targeted growth suppression of melanoma cells," *J Invest Dermatol*, vol. 129, pp. 2233-41, Sep 2009.
[112] M. T. Basel, S. Balivada, H. Wang, T. B. Shrestha, G. M. Seo, M. Pyle, *et al.*, "Cell-delivered magnetic nanoparticles caused hyperthermia-mediated increased survival in a murine pancreatic cancer model," *Int J Nanomedicine*, vol. 7, pp. 297-306, 2012.
[113] P. Wust, U. Gneveckow, P. Wust, U. Gneveckow, M. Johannsen, D. Böhmer, *et al.*, "Magnetic nanoparticles for interstitial thermotherapy – feasibility, tolerance

and achieved temperatures," *International Journal of Hyperthermia,* vol. 22, pp. 673-685, 2006.
[114] R. A. Brooks, F. Moiny, and P. Gillis, "On T2-shortening by weakly magnetized particles: The chemical exchange model†," *Magnetic Resonance in Medicine,* vol. 45, pp. 1014-1020, 2001.
[115] R. A. Brooks, "T(2)-shortening by strongly magnetized spheres: a chemical exchange model," *Magn Reson Med,* vol. 47, pp. 388-91, Feb 2002.
[116] P. Gillis and S. H. Koenig, "Transverse relaxation of solvent protons induced by magnetized spheres: Application to ferritin, erythrocytes, and magnetite," *Magnetic Resonance in Medicine,* vol. 5, pp. 323-345, 1987.
[117] M. Lewin, N. Carlesso, C.-H. Tung, X.-W. Tang, D. Cory, D. T. Scadden, *et al.*, "Tat peptide-derivatized magnetic nanoparticles allow in vivo tracking and recovery of progenitor cells," *Nature biotechnology,* vol. 18, pp. 410-414, 2000.
[118] R. Weissleder, A. Moore, U. Mahmood, R. Bhorade, H. Benveniste, E. A. Chiocca, *et al.*, "In vivo magnetic resonance imaging of transgene expression," *Nature medicine,* vol. 6, pp. 351-354, 2000.
[119] W. S. Enochs, G. Harsh, F. Hochberg, and R. Weissleder, "Improved delineation of human brain tumors on MR images using a long-circulating, superparamagnetic iron oxide agent," *Journal of Magnetic Resonance Imaging,* vol. 9, pp. 228-232, 1999.
[120] M. E. Kooi, V. Cappendijk, K. Cleutjens, A. Kessels, P. Kitslaar, M. Borgers, *et al.*, "Accumulation of ultrasmall superparamagnetic particles of iron oxide in human atherosclerotic plaques can be detected by in vivo magnetic resonance imaging," *Circulation,* vol. 107, pp. 2453-2458, 2003.
[121] S. G. Ruehm, C. Corot, P. Vogt, S. Kolb, and J. F. Debatin, "Magnetic resonance imaging of atherosclerotic plaque with ultrasmall superparamagnetic particles of iron oxide in hyperlipidemic rabbits," *Circulation,* vol. 103, pp. 415-422, 2001.
[122] N. V. Evgenov, Z. Medarova, G. Dai, S. Bonner-Weir, and A. Moore, "In vivo imaging of islet transplantation," *Nature medicine,* vol. 12, pp. 144-148, 2006.
[123] H. Huang, Q. Xie, M. Kang, B. Zhang, H. Zhang, J. Chen, *et al.*, "Labeling transplanted mice islet with polyvinylpyrrolidone coated superparamagnetic iron oxide nanoparticles for in vivo detection by magnetic resonance imaging," *Nanotechnology,* vol. 20, p. 365101, 2009.
[124] M. N. G. Kwon, M. Yokoyama, T. Okano, Y. Sakurai, K. Kataoka, "Block copolymer micelles for drug delivery: loading and release of doxorubicin," *Journal of Controlled Release,* vol. 48, pp. 195-201, 1999.
[125] N. Tang, G. Du, N. Wang, C. Liu, H. Hang, and W. Liang, "Improving penetration in tumors with nanoassemblies of phospholipids and doxorubicin," *J Natl Cancer Inst,* vol. 99, pp. 1004-15, Jul 4 2007.
[126] V. Weissig, K. R. Whiteman, and V. P. Torchilin, "Accumulation of protein-loaded long-circulating micelles and liposomes in subcutaneous Lewis lung carcinoma in mice," *Pharmaceutical Research,* vol. 15, pp. 1552-1556, Oct 1998.
[127] C. Fang, B. Shi, Y. Y. Pei, M. H. Hong, J. Wu, and H. Z. Chen, "In vivo tumor targeting of tumor necrosis factor-α-loaded stealth nanoparticles: Effect of MePEG molecular weight and particle size," *European Journal of Pharmaceutical Sciences,* vol. 27, pp. 27-36, 2006.

[128] K. F. Chu and D. E. Dupuy, "Thermal ablation of tumours: biological mechanisms and advances in therapy," *Nat Rev Cancer,* vol. 14, pp. 199-208, Mar 2014.
[129] R. D. Issels, "Hyperthermia adds to chemotherapy," *Eur J Cancer,* vol. 44, pp. 2546-54, Nov 2008.
[130] J. Otte, "Hyperthermia in cancer therapy," *Eur J Pediatr,* vol. 147, pp. 560-9, Aug 1988.
[131] T. Sadhukha, T. S. Wiedmann, and J. Panyam, "Enhancing therapeutic efficacy through designed aggregation of nanoparticles," *Biomaterials,* vol. 35, pp. 7860-7869, 2014.
[132] K. Pala, A. Serwotka, F. Jelen, P. Jakimowicz, and J. Otlewski, "Tumor-specific hyperthermia with aptamer-tagged superparamagnetic nanoparticles," *Int J Nanomedicine,* vol. 9, pp. 67-76, 2014.
[133] M. Liong, J. Lu, M. Kovochich, T. Xia, S. G. Ruehm, A. E. Nel, *et al.*, "Multifunctional inorganic nanoparticles for imaging, targeting, and drug delivery," *ACS Nano,* vol. 2, pp. 889-96, May 2008.
[134] O. Taratula, R. K. Dani, C. Schumann, H. Xu, A. Wang, H. Song, *et al.*, "Multifunctional nanomedicine platform for concurrent delivery of chemotherapeutic drugs and mild hyperthermia to ovarian cancer cells," *Int J Pharm,* vol. 458, pp. 169-80, Dec 15 2013.
[135] C. Riccardi and I. Nicoletti, "Analysis of apoptosis by propidium iodide staining and flow cytometry," *Nature protocols,* vol. 1, pp. 1458-1461, 2006.
[136] J. Ghuman, P. A. Zunszain, I. Petitpas, A. A. Bhattacharya, M. Otagiri, and S. Curry, "Structural basis of the drug-binding specificity of human serum albumin," *J Mol Biol,* vol. 353, pp. 38-52, Oct 14 2005.
[137] J. Wang, D. Mongayt, and V. P. Torchilin, "Polymeric micelles for delivery of poorly soluble drugs: preparation and anticancer activity in vitro of paclitaxel incorporated into mixed micelles based on poly(ethylene glycol)-lipid conjugate and positively charged lipids," *J Drug Target,* vol. 13, pp. 73-80, Jan 2005.
[138] L. Mu, T. A. Elbayoumi, and V. P. Torchilin, "Mixed micelles made of poly(ethylene glycol)-phosphatidylethanolamine conjugate and d-alpha-tocopheryl polyethylene glycol 1000 succinate as pharmaceutical nanocarriers for camptothecin," *Int J Pharm,* vol. 306, pp. 142-9, Dec 8 2005.
[139] O. M. Koo, I. Rubinstein, and H. Onyuksel, "Camptothecin in sterically stabilized phospholipid micelles: a novel nanomedicine," *Nanomedicine,* vol. 1, pp. 77-84, Mar 2005.
[140] A. Krishnadas, I. Rubinstein, and H. Önyüksel, "Sterically stabilized phospholipid mixed micelles: in vitro evaluation as a novel carrier for water-insoluble drugs," *Pharmaceutical research,* vol. 20, pp. 297-302, 2003.
[141] M. P. Alvarez-Berrios, A. Castillo, J. Mendez, O. Soto, C. Rinaldi, and M. Torres-Lugo, "Hyperthermic potentiation of cisplatin by magnetic nanoparticle heaters is correlated with an increase in cell membrane fluidity," *Int J Nanomedicine,* vol. 8, pp. 1003-13, 2013.
[142] L. Tong, Y. Zhao, T. B. Huff, M. N. Hansen, A. Wei, and J. X. Cheng, "Gold Nanorods Mediate Tumor Cell Death by Compromising Membrane Integrity," *Adv Mater,* vol. 19, pp. 3136-3141, 2007.

[143] E. Amstad, J. Kohlbrecher, E. Muller, T. Schweizer, M. Textor, and E. Reimhult, "Triggered release from liposomes through magnetic actuation of iron oxide nanoparticle containing membranes," *Nano Lett,* vol. 11, pp. 1664-70, Apr 13 2011.
[144] H. Kim, D. Lee, J. Kim, T.-i. Kim, and W. J. Kim, "Photothermally triggered cytosolic drug delivery via endosome disruption using a functionalized reduced graphene oxide," *ACS nano,* vol. 7, pp. 6735-6746, 2013.
[145] E. Manders, F. Verbeek, and J. Aten, "Measurement of co-localization of objects in dual-colour confocal images," *Journal of microscopy,* vol. 169, pp. 375-382, 1993.
[146] R. J. Palzer and C. Heidelberger, "Studies on the quantitative biology of hyperthermic killing of Hela cells," *Cancer Research,* vol. 33, pp. 415-321, 1973.
[147] B. S. Packard and D. E. Wolf, "Fluorescence lifetimes of carbocyanine lipid analogs in phospholipid bilayers," *Biochemistry,* vol. 24, pp. 5176-5181, 1985.
[148] D. E. Owens, 3rd and N. A. Peppas, "Opsonization, biodistribution, and pharmacokinetics of polymeric nanoparticles," *Int J Pharm,* vol. 307, pp. 93-102, Jan 3 2006.
[149] R. Gref, M. Luck, P. Quellec, M. Marchand, E. Dellacherie, S. Harnisch, *et al.*, "'Stealth' corona-core nanoparticles surface modified by polyethylene glycol (PEG): influences of the corona (PEG chain length and surface density) and of the core composition on phagocytic uptake and plasma protein adsorption," *Colloids Surf B Biointerfaces,* vol. 18, pp. 301-313, Oct 1 2000.
[150] R. Gref, Y. Minamitake, M. T. Peracchia, V. Trubetskoy, V. Torchilin, and R. Langer, "Biodegradable long-circulating polymeric nanospheres," *Science,* vol. 263, pp. 1600-1603, 1994.
[151] Y. Wang, R. Wang, X. Lu, W. Lu, C. Zhang, and W. Liang, "Pegylated phospholipids-based self-assembly with water-soluble drugs," *Pharm Res,* vol. 27, pp. 361-70, Feb 2010.
[152] J. R. Lepock, "Cellular effects of hyperthermia: relevance to the minimum dose for thermal damage," *International Journal of Hyperthermia,* vol. 19, pp. 252-266, 2003.
[153] J. Barnes, D. Dix, B. Collins, C. Luft, and J. Allen, "Expression of inducible Hsp70 enhances the proliferation of MCF-7 breast cancer cells and protects against the cytotoxic effects of hyperthermia," *Cell stress & chaperones,* vol. 6, p. 316, 2001.
[154] T. A. Kato, A. Tsuda, M. Uesaka, A. Fujimori, T. Kamada, H. Tsujii, *et al.*, "In vitro characterization of cells derived from chordoma cell line U-CH1 following treatment with X-rays, heavy ions and chemotherapeutic drugs," *Radiat Oncol,* vol. 6, p. 116, 2011.
[155] R. D. Dabholkar, R. M. Sawant, D. A. Mongayt, P. V. Devarajan, and V. P. Torchilin, "Polyethylene glycol-phosphatidylethanolamine conjugate (PEG-PE)-based mixed micelles: some properties, loading with paclitaxel, and modulation of P-glycoprotein-mediated efflux," *Int J Pharm,* vol. 315, pp. 148-57, Jun 6 2006.
[156] M. R. Wenk, A. Fahr, R. Reszka, and J. Seelig, "Paclitaxel partitioning into lipid bilayers," *Journal of pharmaceutical sciences,* vol. 85, pp. 228-231, 1996.

[157] F. Mohamed, P. Marchettini, O. A. Stuart, M. Urano, and P. H. Sugarbaker, "Thermal enhancement of new chemotherapeutic agents at moderate hyperthermia," *Annals of surgical oncology,* vol. 10, pp. 463-468, 2003.
[158] B. Leal, M. Meltz, N. Mohan, J. Kuhn, T. Prihoda, and T. Herman, "Interaction of hyperthermia with Taxol in human MCF-7 breast adenocarcinoma cells," *International journal of hyperthermia,* vol. 15, pp. 225-236, 1999.
[159] R. Rietbroek, D. Katschinski, M. Reijers, H. Robins, A. Geerdink, K. Tutsch, *et al.*, "Lack of thermal enhancement for taxanes in vitro," *International journal of hyperthermia,* vol. 13, pp. 525-533, 1997.
[160] T. Kondo, K. Ueda, and E. Kano, "Combined effects of hyperthermia and CPT-11 on DNA strand breaks in mouse mammary carcinoma FM3A cells," *Anticancer research,* vol. 15, pp. 83-86, 1994.
[161] C. Ng, A. Bussey, and G. Raaphorst, "Sequence of treatment is important in the modification of camptothecin induced cell killing by hyperthermia," *International Journal of Hyperthermia,* vol. 12, pp. 663-678, 1996.
[162] W. Lu, G. Zhang, R. Zhang, L. G. Flores, Q. Huang, J. G. Gelovani, *et al.*, "Tumor site–specific silencing of NF-κB p65 by targeted hollow gold nanosphere–mediated photothermal transfection," *Cancer research,* vol. 70, pp. 3177-3188, 2010.
[163] H. S. Choi, W. Liu, P. Misra, E. Tanaka, J. P. Zimmer, B. I. Ipe, *et al.*, "Renal clearance of quantum dots," *Nature biotechnology,* vol. 25, pp. 1165-1170, 2007.
[164] G. Kong, R. D. Braun, and M. W. Dewhirst, "Hyperthermia enables tumor-specific nanoparticle delivery: effect of particle size," *Cancer Res,* vol. 60, pp. 4440-5, Aug 15 2000.
[165] B. Chertok, B. A. Moffat, A. E. David, F. Yu, C. Bergemann, B. D. Ross, *et al.*, "Iron oxide nanoparticles as a drug delivery vehicle for MRI monitored magnetic targeting of brain tumors," *Biomaterials,* vol. 29, pp. 487-96, Feb 2008.
[166] C. Bremer, C.-H. Tung, and R. Weissleder, "In vivo molecular target assessment of matrix metalloproteinase inhibition," *Nature medicine,* vol. 7, pp. 743-748, 2001.
[167] K. Cheng, S. Peng, C. Xu, and S. Sun, "Porous hollow Fe3O4 nanoparticles for targeted delivery and controlled release of cisplatin," *Journal of the American Chemical Society,* vol. 131, pp. 10637-10644, 2009.
[168] P. Mohan and N. Rapoport, "Doxorubicin as a molecular nanotheranostic agent: effect of doxorubicin encapsulation in micelles or nanoemulsions on the ultrasound-mediated intracellular delivery and nuclear trafficking," *Molecular pharmaceutics,* vol. 7, pp. 1959-1973, 2010.
[169] W. Li, X. Cai, C. Kim, G. Sun, Y. Zhang, R. Deng, *et al.*, "Gold nanocages covered with thermally-responsive polymers for controlled release by high-intensity focused ultrasound," *Nanoscale,* vol. 3, pp. 1724-30, Apr 2011.
[170] Y. Ma, X. Liang, S. Tong, G. Bao, Q. Ren, and Z. Dai, "Gold Nanoshell Nanomicelles for Potential Magnetic Resonance Imaging, Light-Triggered Drug Release, and Photothermal Therapy," *Advanced Functional Materials,* vol. 23, pp. 815-822, 2013.

[171] M. L. Hauck, S. M. LaRue, W. P. Petros, J. M. Poulson, D. Yu, I. Spasojevic, *et al.*, "Phase I trial of doxorubicin-containing low temperature sensitive liposomes in spontaneous canine tumors," *Clin Cancer Res,* vol. 12, pp. 4004-10, Jul 1 2006.
[172] J. K. Mills and D. Needham, "Lysolipid incorporation in dipalmitoylphosphatidylcholine bilayer membranes enhances the ion permeability and drug release rates at the membrane phase transition," *Biochim Biophys Acta,* vol. 1716, pp. 77-96, Oct 15 2005.
[173] P. S. Yarmolenko, Y. Zhao, C. Landon, I. Spasojevic, F. Yuan, D. Needham, *et al.*, "Comparative effects of thermosensitive doxorubicin-containing liposomes and hyperthermia in human and murine tumours," *Int J Hyperthermia,* vol. 26, pp. 485-98, 2010.
[174] G. R. Anyarambhatla and D. Needham, "Enhancement of the phase transition permeability of DPPC liposomes by incorporation of MPPC: a new temperature-sensitive liposome for use with mild hyperthermia," *Journal of Liposome Research,* vol. 9, pp. 491-506, 1999.
[175] M. S. Yavuz, Y. Cheng, J. Chen, C. M. Cobley, Q. Zhang, M. Rycenga, *et al.*, "Gold nanocages covered by smart polymers for controlled release with near-infrared light," *Nat Mater,* vol. 8, pp. 935-9, Dec 2009.
[176] J. You, R. Zhang, G. Zhang, M. Zhong, Y. Liu, C. S. Van Pelt, *et al.*, "Photothermal-chemotherapy with doxorubicin-loaded hollow gold nanospheres: A platform for near-infrared light-trigged drug release," *J Control Release,* vol. 158, pp. 319-28, Mar 10 2012.
[177] J. H. Park, G. von Maltzahn, L. L. Ong, A. Centrone, T. A. Hatton, E. Ruoslahti, *et al.*, "Cooperative nanoparticles for tumor detection and photothermally triggered drug delivery," *Adv Mater,* vol. 22, pp. 880-5, Feb 23 2010.
[178] R. A. Frimpong and J. Z. Hilt, "Poly(n-isopropylacrylamide)-based hydrogel coatings on magnetite nanoparticles via atom transfer radical polymerization," *Nanotechnology,* vol. 19, p. 175101, Apr 30 2008.
[179] S. R. Deka, A. Quarta, R. Di Corato, A. Riedinger, R. Cingolani, and T. Pellegrino, "Magnetic nanobeads decorated by thermo-responsive PNIPAM shell as medical platforms for the efficient delivery of doxorubicin to tumour cells," *Nanoscale,* vol. 3, pp. 619-29, Feb 2011.
[180] S. Purushotham, P. E. Chang, H. Rumpel, I. H. Kee, R. T. Ng, P. K. Chow, *et al.*, "Thermoresponsive core-shell magnetic nanoparticles for combined modalities of cancer therapy," *Nanotechnology,* vol. 20, p. 305101, Jul 29 2009.
[181] A. Aqil, S. Vasseur, E. Duguet, C. Passirani, J. P. Benoît, R. Jérôme, *et al.*, "Magnetic nanoparticles coated by temperature responsive copolymers for hyperthermia," *Journal of Materials Chemistry,* vol. 18, p. 3352, 2008.
[182] M. Pernia Leal, A. Torti, A. Riedinger, R. La Fleur, D. Petti, R. Cingolani, *et al.*, "Controlled release of doxorubicin loaded within magnetic thermo-responsive nanocarriers under magnetic and thermal actuation in a microfluidic channel," *ACS Nano,* vol. 6, pp. 10535-45, Dec 21 2012.
[183] S. Balasubramaniam, N. Pothayee, Y. Lin, M. House, R. C. Woodward, T. G. St. Pierre, *et al.*, "Poly(N-isopropylacrylamide)-Coated Superparamagnetic Iron Oxide Nanoparticles: Relaxometric and Fluorescence Behavior Correlate to

Temperature-Dependent Aggregation," *Chemistry of Materials,* vol. 23, pp. 3348-3356, 2011.
[184] H. Vihola, A. Laukkanen, L. Valtola, H. Tenhu, and J. Hirvonen, "Cytotoxicity of thermosensitive polymers poly (N-isopropylacrylamide), poly (N-vinylcaprolactam) and amphiphilically modified poly (N-vinylcaprolactam)," *Biomaterials,* vol. 26, pp. 3055-3064, 2005.
[185] S. Purushotham and R. V. Ramanujan, "Thermoresponsive magnetic composite nanomaterials for multimodal cancer therapy," *Acta Biomater,* vol. 6, pp. 502-10, Feb 2010.
[186] B. Ashok, L. Arleth, R. P. Hjelm, I. Rubinstein, and H. Onyuksel, "In vitro characterization of PEGylated phospholipid micelles for improved drug solubilization: effects of PEG chain length and PC incorporation," *J Pharm Sci,* vol. 93, pp. 2476-87, Oct 2004.
[187] O. Mouritsen, K. Jorgensen, and T. Honger, "Permeability of lipid bilayers near the phase transition," *Permeability and stability of lipid bilayers,* pp. 137-160, 1995.
[188] A. K. Kenworthy, S. A. Simon, and T. J. McIntosh, "Structure and phase behavior of lipid suspensions containing phospholipids with covalently attached poly (ethylene glycol)," *Biophysical journal,* vol. 68, p. 1903, 1995.
[189] H. Heerklotz, "The microcalorimetry of lipid membranes," *Journal of Physics: Condensed Matter,* vol. 16, pp. R441-R467, 2004.
[190] D. Needham, G. Anyarambhatla, G. Kong, and M. W. Dewhirst, "A new temperature-sensitive liposome for use with mild hyperthermia: characterization and testing in a human tumor xenograft model," *Cancer research,* vol. 60, pp. 1197-1201, 2000.
[191] G. Kong, G. Anyarambhatla, W. P. Petros, R. D. Braun, O. M. Colvin, D. Needham, *et al.*, "Efficacy of liposomes and hyperthermia in a human tumor xenograft model: importance of triggered drug release," *Cancer Research,* vol. 60, pp. 6950-6957, 2000.
[192] L. Arleth, B. Ashok, H. Onyuksel, P. Thiyagarajan, J. Jacob, and R. P. Hjelm, "Detailed structure of hairy mixed micelles formed by phosphatidylcholine and PEGylated phospholipids in aqueous media," *Langmuir,* vol. 21, pp. 3279-3290, 2005.
[193] L. n. Lartigue, P. Hugounenq, D. Alloyeau, S. P. Clarke, M. Lévy, J.-C. Bacri, *et al.*, "Cooperative organization in iron oxide multi-core nanoparticles potentiates their efficiency as heating mediators and MRI contrast agents," *ACS nano,* vol. 6, pp. 10935-10949, 2012.
[194] R. Di Corato, A. Espinosa, L. Lartigue, M. Tharaud, S. Chat, T. Pellegrino, *et al.*, "Magnetic hyperthermia efficiency in the cellular environment for different nanoparticle designs," *Biomaterials,* vol. 35, pp. 6400-11, Aug 2014.
[195] M. Pappalardo, D. Milardi, D. Grasso, and C. La Rosa, "Phase behaviour of polymer-grafted DPPC membranes for drug delivery systems design," *Journal of thermal analysis and calorimetry,* vol. 80, pp. 413-418, 2005.
[196] Z. Xu, C. Shen, Y. Hou, H. Gao, and S. Sun, "Oleylamine as both reducing agent and stabilizer in a facile synthesis of magnetite nanoparticles," *Chemistry of Materials,* vol. 21, pp. 1778-1780, 2009.

[197] M. E. Materia, P. Guardia, A. Sathya, M. Pernia Leal, R. Marotta, R. Di Corato, *et al.*, "Mesoscale Assemblies of Iron Oxide Nanocubes as Heat Mediators and Image Contrast Agents," *Langmuir,* vol. 31, pp. 808-816, 2015.
[198] I. Andreu, E. Natividad, L. Solozábal, and O. Roubeau, "Nano-objects for Addressing the Control of Nanoparticle Arrangement and Performance in Magnetic Hyperthermia," *ACS nano,* vol. 9, pp. 1408-1419, 2015.
[199] R. Chen, M. G. Christiansen, and P. Anikeeva, "Maximizing hysteretic losses in magnetic ferrite nanoparticles via model-driven synthesis and materials optimization," *ACS nano,* vol. 7, pp. 8990-9000, 2013.
[200] R. Hergt, S. Dutz, and M. Röder, "Effects of size distribution on hysteresis losses of magnetic nanoparticles for hyperthermia," *Journal of Physics: Condensed Matter,* vol. 20, p. 385214, 2008.
[201] J. P. Fortin, C. Wilhelm, J. Servais, C. Menager, J. C. Bacri, and F. Gazeau, "Size-sorted anionic iron oxide nanomagnets as colloidal mediators for magnetic hyperthermia," *J Am Chem Soc,* vol. 129, pp. 2628-35, Mar 7 2007.
[202] M. Gonzales-Weimuller, M. Zeisberger, and K. M. Krishnan, "Size-dependant heating rates of iron oxide nanoparticles for magnetic fluid hyperthermia," *Journal of Magnetism and Magnetic Materials,* vol. 321, pp. 1947-1950, 2009.
[203] M. Levy, A. Quarta, A. Espinosa, A. Figuerola, C. Wilhelm, M. García-Hernández, *et al.*, "Correlating magneto-structural properties to hyperthermia performance of highly monodisperse iron oxide nanoparticles prepared by a seeded-growth route," *Chemistry of Materials,* vol. 23, pp. 4170-4180, 2011.
[204] P. Guardia, R. Di Corato, L. Lartigue, C. Wilhelm, A. Espinosa, M. Garcia-Hernandez, *et al.*, "Water-soluble iron oxide nanocubes with high values of specific absorption rate for cancer cell hyperthermia treatment," *ACS Nano,* vol. 6, pp. 3080-91, Apr 24 2012.
[205] D. A. Yablonskiy and E. M. Haacke, "Theory of NMR signal behavior in magnetically inhomogeneous tissues: the static dephasing regime," *Magnetic Resonance in Medicine,* vol. 32, pp. 749-763, 1994.
[206] N. Lee, Y. Choi, Y. Lee, M. Park, W. K. Moon, S. H. Choi, *et al.*, "Water-dispersible ferrimagnetic iron oxide nanocubes with extremely high r(2) relaxivity for highly sensitive in vivo MRI of tumors," *Nano Lett,* vol. 12, pp. 3127-31, Jun 13 2012.
[207] H. Duan, M. Kuang, X. Wang, Y. A. Wang, H. Mao, and S. Nie, "Reexamining the effects of particle size and surface chemistry on the magnetic properties of iron oxide nanocrystals: new insights into spin disorder and proton relaxivity," *The Journal of Physical Chemistry C,* vol. 112, pp. 8127-8131, 2008.
[208] Y.-w. Jun, Y.-M. Huh, J.-s. Choi, J.-H. Lee, H.-T. Song, S. Kim, *et al.*, "Nanoscale size effect of magnetic nanocrystals and their utilization for cancer diagnosis via magnetic resonance imaging," *Journal of the American Chemical Society,* vol. 127, pp. 5732-5733, 2005.
[209] K. M. Krishnan, A. B. Pakhomov, Y. Bao, P. Blomqvist, Y. Chun, M. Gonzales, *et al.*, "Nanomagnetism and spin electronics: materials, microstructure and novel properties," *Journal of materials science,* vol. 41, pp. 793-815, 2006.

[210] S. Purushotham and R. V. Ramanujan, "Modeling the performance of magnetic nanoparticles in multimodal cancer therapy," *Journal of Applied Physics,* vol. 107, p. 114701, 2010.
[211] D. Jiles and D. Atherton, "Theory of ferromagnetic hysteresis," *Journal of magnetism and magnetic materials,* vol. 61, pp. 48-60, 1986.
[212] S.-h. Noh, W. Na, J.-t. Jang, J.-H. Lee, E. J. Lee, S. H. Moon, *et al.*, "Nanoscale magnetism control via surface and exchange anisotropy for optimized ferrimagnetic hysteresis," *Nano letters,* vol. 12, pp. 3716-3721, 2012.
[213] C. Martinez-Boubeta, K. Simeonidis, A. Makridis, M. Angelakeris, O. Iglesias, P. Guardia, *et al.*, "Learning from nature to improve the heat generation of iron-oxide nanoparticles for magnetic hyperthermia applications," *Scientific reports,* vol. 3, 2013.
[214] S. Laurent, D. Forge, M. Port, A. Roch, C. Robic, L. Vander Elst, *et al.*, "Magnetic iron oxide nanoparticles: synthesis, stabilization, vectorization, physicochemical characterizations, and biological applications," *Chemical reviews,* vol. 108, pp. 2064-2110, 2008.
[215] C. Bean and J. Livingston, "Superparamagnetism," *Journal of Applied Physics,* vol. 30, pp. S120-S129, 1959.
[216] T. Neuberger, B. Schöpf, H. Hofmann, M. Hofmann, and B. Von Rechenberg, "Superparamagnetic nanoparticles for biomedical applications: possibilities and limitations of a new drug delivery system," *Journal of Magnetism and Magnetic Materials,* vol. 293, pp. 483-496, 2005.
[217] A. Figuerola, R. Di Corato, L. Manna, and T. Pellegrino, "From iron oxide nanoparticles towards advanced iron-based inorganic materials designed for biomedical applications," *Pharmacological Research,* vol. 62, pp. 126-143, 2010.
[218] N. Lee and T. Hyeon, "Designed synthesis of uniformly sized iron oxide nanoparticles for efficient magnetic resonance imaging contrast agents," *Chemical Society Reviews,* vol. 41, pp. 2575-2589, 2012.
[219] X. Batlle and A. Labarta, "Finite-size effects in fine particles: magnetic and transport properties," *Journal of Physics D: Applied Physics,* vol. 35, p. R15, 2002.
[220] T. Shendruk, R. Desautels, B. Southern, and J. Van Lierop, "The effect of surface spin disorder on the magnetism of γ-Fe2O3 nanoparticle dispersions," *Nanotechnology,* vol. 18, p. 455704, 2007.
[221] T. Kim and M. Shima, "Reduced magnetization in magnetic oxide nanoparticles," *Journal of applied physics,* vol. 101, p. 09M516, 2007.
[222] K. J. Klabunde and R. M. Richards, *Nanoscale materials in chemistry*: John Wiley & Sons, 2009.
[223] R. O'Handley, "Modern Magnetic Materials: Principles and Applications O'HANDLEY Robert C," ed: Librairie Lavoisier, 2000.
[224] M. Ma, Y. Wu, J. Zhou, Y. Sun, Y. Zhang, and N. Gu, "Size dependence of specific power absorption of Fe 3 O 4 particles in AC magnetic field," *Journal of Magnetism and Magnetic Materials,* vol. 268, pp. 33-39, 2004.
[225] P. Guardia, A. Riedinger, S. Nitti, G. Pugliese, S. Marras, A. Genovese, *et al.*, "One pot synthesis of monodisperse water soluble iron oxide nanocrystals with

high values of the specific absorption rate," *Journal of Materials Chemistry B,* vol. 2, pp. 4426-4434, 2014.
[226] R. Hergt, R. Hiergeist, M. Zeisberger, D. Schüler, U. Heyen, I. Hilger, *et al.*, "Magnetic properties of bacterial magnetosomes as potential diagnostic and therapeutic tools," *Journal of Magnetism and Magnetic Materials,* vol. 293, pp. 80-86, 2005.
[227] A. C. Silva, T. R. Oliveira, J. B. Mamani, S. Malheiros, L. Malavolta, L. F. Pavon, *et al.*, "Application of hyperthermia induced by superparamagnetic iron oxide nanoparticles in glioma treatment," *Int J Nanomedicine,* vol. 6, pp. 591-603, 2011.
[228] C. L. Dennis, A. J. Jackson, J. A. Borchers, P. J. Hoopes, R. Strawbridge, A. R. Foreman, *et al.*, "Nearly complete regression of tumors via collective behavior of magnetic nanoparticles in hyperthermia," *Nanotechnology,* vol. 20, p. 395103, Sep 30 2009.
[229] S. Balivada, R. S. Rachakatla, H. Wang, T. N. Samarakoon, R. K. Dani, M. Pyle, *et al.*, "A/C magnetic hyperthermia of melanoma mediated by iron(0)/iron oxide core/shell magnetic nanoparticles: a mouse study," *BMC Cancer,* vol. 10, p. 119, 2010.
[230] W. Tilly, P. Wust, B. Rau, C. Harder, J. Gellermann, P. Schlag, *et al.*, "Temperature data and specific absorption rates in pelvic tumours: predictive factors and correlations," *International journal of hyperthermia,* vol. 17, pp. 172-188, 2001.
[231] A. Granov, O. Muratov, and V. Frolov, "Problems in the local hyperthermia of inductively heated embolized tissues," *Theoretical Foundations of Chemical Engineering,* vol. 36, pp. 63-66, 2002.
[232] I. A. Brezovich, "Low frequency hyperthermia: capacitive and ferromagnetic thermoseed methods," *Medical physics monograph,* vol. 16, pp. 82-111, 1988.
[233] W. J. Atkinson, I. A. Brezovich, and D. P. Chakraborty, "Usable frequencies in hyperthermia with thermal seeds," *Biomedical Engineering, IEEE Transactions on,* pp. 70-75, 1984.
[234] P. Hoopes, R. Strawbridge, U. Gibson, Q. Zeng, Z. Pierce, M. Savellano, *et al.*, "Intratumoral iron oxide nanoparticle hyperthermia and radiation cancer treatment," in *Biomedical Optics (BiOS) 2007,* 2007, pp. 64400K-64400K-10.
[235] Q. Zhao, L. Wang, R. Cheng, L. Mao, R. D. Arnold, E. W. Howerth, *et al.*, "Magnetic nanoparticle-based hyperthermia for head & neck cancer in mouse models," *Theranostics,* vol. 2, pp. 113-21, 2012.
[236] A. Ito, K. Tanaka, H. Honda, S. Abe, H. Yamaguchi, and T. Kobayashi, "Complete regression of mouse mammary carcinoma with a size greater than 15 mm by frequent repeated hyperthermia using magnetite nanoparticles," *Journal of bioscience and bioengineering,* vol. 96, pp. 364-369, 2003.
[237] J. Braun and G. M. Hahn, "Enhanced cell killing by bleomycin and 43 hyperthermia and the inhibition of recovery from potentially lethal damage," *Cancer research,* vol. 35, pp. 2921-2927, 1975.
[238] K. E. Wallner and G. C. Li, "Effect of drug exposure duration and sequencing on hyperthermic potentiation of mitomycin-C and cisplatin," *Cancer research,* vol. 47, pp. 493-495, 1987.

[239] R. U. Jänicke, M. L. Sprengart, M. R. Wati, and A. G. Porter, "Caspase-3 is required for DNA fragmentation and morphological changes associated with apoptosis," *Journal of Biological Chemistry,* vol. 273, pp. 9357-9360, 1998.
[240] A. G. Porter and R. U. Jänicke, "Emerging roles of caspase-3 in apoptosis," *Cell death and differentiation,* vol. 6, pp. 99-104, 1999.
[241] S.-W. Yu, H. Wang, M. F. Poitras, C. Coombs, W. J. Bowers, H. J. Federoff, *et al.*, "Mediation of poly (ADP-ribose) polymerase-1-dependent cell death by apoptosis-inducing factor," *Science,* vol. 297, pp. 259-263, 2002.
[242] S. J. Hong, T. M. Dawson, and V. L. Dawson, "Nuclear and mitochondrial conversations in cell death: PARP-1 and AIF signaling," *Trends in pharmacological sciences,* vol. 25, pp. 259-264, 2004.
[243] J. Yang, X. Liu, K. Bhalla, C. N. Kim, A. M. Ibrado, J. Cai, *et al.*, "Prevention of apoptosis by Bcl-2: release of cytochrome c from mitochondria blocked," *Science,* vol. 275, pp. 1129-1132, 1997.
[244] R. M. Kluck, E. Bossy-Wetzel, D. R. Green, and D. D. Newmeyer, "The release of cytochrome c from mitochondria: a primary site for Bcl-2 regulation of apoptosis," *Science,* vol. 275, pp. 1132-1136, 1997.
[245] L. H. Boise, M. González-García, C. E. Postema, L. Ding, T. Lindsten, L. A. Turka, *et al.*, "bcl-x, a bcl-2-related gene that functions as a dominant regulator of apoptotic cell death," *cell,* vol. 74, pp. 597-608, 1993.
[246] H. M. Beere and D. R. Green, "Stress management–heat shock protein-70 and the regulation of apoptosis," *Trends in cell biology,* vol. 11, pp. 6-10, 2001.
[247] A. S. Sreedhar and P. Csermely, "Heat shock proteins in the regulation of apoptosis: new strategies in tumor therapy: a comprehensive review," *Pharmacol Ther,* vol. 101, pp. 227-57, Mar 2004.
[248] A. Ito, H. Saito, K. Mitobe, Y. Minamiya, N. Takahashi, K. Maruyama, *et al.*, "Inhibition of heat shock protein 90 sensitizes melanoma cells to thermosensitive ferromagnetic particle-mediated hyperthermia with low Curie temperature," *Cancer science,* vol. 100, pp. 558-564, 2009.
[249] R. Kappiyoor, M. Liangruksa, R. Ganguly, and I. K. Puri, "The effects of magnetic nanoparticle properties on magnetic fluid hyperthermia," *Journal of Applied Physics,* vol. 108, p. 094702, 2010.
[250] M. Salloum, R. Ma, and L. Zhu, "Enhancement in treatment planning for magnetic nanoparticle hyperthermia: optimization of the heat absorption pattern," *International Journal of Hyperthermia,* vol. 25, pp. 309-321, 2009.
[251] C. He, Y. Hu, L. Yin, C. Tang, and C. Yin, "Effects of particle size and surface charge on cellular uptake and biodistribution of polymeric nanoparticles," *Biomaterials,* vol. 31, pp. 3657-3666, 2010.
[252] M. Levy, N. Luciani, D. Alloyeau, D. Elgrabli, V. Deveaux, C. Pechoux, *et al.*, "Long term in vivo biotransformation of iron oxide nanoparticles," *Biomaterials,* vol. 32, pp. 3988-3999, 2011.
[253] Z. Cheng, A. Al Zaki, J. Z. Hui, V. R. Muzykantov, and A. Tsourkas, "Multifunctional nanoparticles: cost versus benefit of adding targeting and imaging capabilities," *Science,* vol. 338, pp. 903-10, Nov 16 2012.
[254] E. Ruoslahti, S. N. Bhatia, and M. J. Sailor, "Targeting of drugs and nanoparticles to tumors," *The Journal of cell biology,* vol. 188, pp. 759-768, 2010.

[255] P. C. Brooks, A. M. Montgomery, M. Rosenfeld, R. A. Reisfeld, T. Hu, G. Klier, *et al.*, "Integrin α v β 3 antagonists promote tumor regression by inducing apoptosis of angiogenic blood vessels," *Cell*, vol. 79, pp. 1157-1164, 1994.
[256] A. Erdreich-Epstein, H. Shimada, S. Groshen, M. Liu, L. S. Metelitsa, K. S. Kim, *et al.*, "Integrins αvβ3 and αvβ5 are expressed by endothelium of high-risk neuroblastoma and their inhibition is associated with increased endogenous ceramide," *Cancer research*, vol. 60, pp. 712-721, 2000.
[257] J. S. Desgrosellier and D. A. Cheresh, "Integrins in cancer: biological implications and therapeutic opportunities," *Nature Reviews Cancer*, vol. 10, pp. 9-22, 2010.
[258] A. J. Primeau, A. Rendon, D. Hedley, L. Lilge, and I. F. Tannock, "The distribution of the anticancer drug Doxorubicin in relation to blood vessels in solid tumors," *Clinical Cancer Research*, vol. 11, pp. 8782-8788, 2005.
[259] A. I. Minchinton and I. F. Tannock, "Drug penetration in solid tumours," *Nature Reviews Cancer*, vol. 6, pp. 583-592, 2006.
[260] K. N. Sugahara, T. Teesalu, P. P. Karmali, V. R. Kotamraju, L. Agemy, O. M. Girard, *et al.*, "Tissue-penetrating delivery of compounds and nanoparticles into tumors," *Cancer cell*, vol. 16, pp. 510-520, 2009.
[261] T. Teesalu, K. N. Sugahara, V. R. Kotamraju, and E. Ruoslahti, "C-end rule peptides mediate neuropilin-1-dependent cell, vascular, and tissue penetration," *Proceedings of the National Academy of Sciences*, vol. 106, pp. 16157-16162, 2009.
[262] T. Teesalu, K. N. Sugahara, and E. Ruoslahti, "Tumor-penetrating peptides," *Frontiers in oncology*, vol. 3, 2013.
[263] Q. A. Pankhurst, J. Connolly, S. Jones, and J. Dobson, "Applications of magnetic nanoparticles in biomedicine," *Journal of physics D: Applied physics*, vol. 36, p. R167, 2003.
[264] C. Alexiou, W. Arnold, R. J. Klein, F. G. Parak, P. Hulin, C. Bergemann, *et al.*, "Locoregional cancer treatment with magnetic drug targeting," *Cancer research*, vol. 60, pp. 6641-6648, 2000.
[265] N. Schleich, C. Po, D. Jacobs, B. Ucakar, B. Gallez, F. Danhier, *et al.*, "Comparison of active, passive and magnetic targeting to tumors of multifunctional paclitaxel/SPIO-loaded nanoparticles for tumor imaging and therapy," *Journal of Controlled Release*, vol. 194, pp. 82-91, 2014.
[266] B. Gleich, N. Hellwig, H. Bridell, R. Jurgons, C. Seliger, C. Alexiou, *et al.*, "Design and evaluation of magnetic fields for nanoparticle drug targeting in cancer," *Nanotechnology, IEEE Transactions on*, vol. 6, pp. 164-170, 2007.
[267] B. Shapiro, "Towards dynamic control of magnetic fields to focus magnetic carriers to targets deep inside the body," *J Magn Magn Mater*, vol. 321, p. 1594, May 1 2009.
[268] G. Kong, R. D. Braun, and M. W. Dewhirst, "Characterization of the effect of hyperthermia on nanoparticle extravasation from tumor vasculature," *Cancer Research*, vol. 61, pp. 3027-3032, 2001.

VITA

Christopher A. Quinto

Christopher was born in Queens, New York. He attended public schools in the Herricks School District in Long Island, New York, received a B.S. in Biomedical Engineering and Mechanical Engineering from Rensselaer Polytechnic Institute, Troy, New York in 2010 before coming to Georgia Tech to pursue a doctorate in Biomedical Engineering. When he is not working on his research, Christopher enjoys cooking, listening to live music, and spending time with his dog, Lana, and two cats, Martin and Roxanne.